PHOTOPHYSICAL STUDIES OF ELECTRONIC STRUCTURE AND EXCITED-

STATE DYNAMICS OF DNA-TEMPLATED CYANINE DYE AGGREGATES

by

Jonathan Samuel Huff

A dissertation

submitted in partial fulfillment

of the requirements for the degree of

Doctor of Philosophy in Materials Science and Engineering

Boise State University

August 2023

BOISE STATE UNIVERSITY GRADUATE COLLEGE

DEFENSE COMMITTEE AND FINAL READING APPROVALS

of the dissertation submitted by

Jonathan Samuel Huff

Dissertation Title: Photophysical Studies of Electronic Structure and Excited-State Dynamics of DNA-Templated Cyanine Dye Aggregates

Date of Final Oral Examination: 22 May 2023

The following individuals read and discussed the dissertation submitted by student Jonathan Samuel Huff, and they evaluated the student's presentation and response to questions during the final oral examination. They found that the student passed the final oral examination.

William B. Knowlton, Ph.D.	Chair, Supervisory Committee
Bernard Yurke, Ph.D.	Co-Chair, Supervisory Committee
Ryan D. Pensack, Ph.D.	Co-Chair, Supervisory Committee
Joseph Melinger, Ph.D.	Member, Supervisory Committee
Daniel B. Turner, Ph.D.	Member, Supervisory Committee

The final reading approval of the dissertation was granted by William B. Knowlton, Ph.D., Co-Chair of the Supervisory Committee. The dissertation was approved by the Graduate College.

DEDICATION

To my wife, Angela

ACKNOWLEDGMENTS

I would like to thank former students Donald Kellis, Chris Green, Allison Christy, and Drew Lysne for all the stimulating and entertaining conversations over the years. I would also like to acknowledge the support and encouragement I have received from the entire Nanoscale Materials and Device Group. I would also like to thank Jessica Economy and all of the past and present MSE front office staff for making me feel welcome.

I have had the pleasure of working directly with some very intelligent, talented, and helpful people while at Boise State. I would like to thank Dr. Paul Davis, and Dr. Nirmala Kandadai for teaching me about lasers, Donald Kellis training me in the labs, Lance Patten, Simon Roy, Austin Biaggne, and German Barcenas for providing their insights and expertise on structural modelling, and Dr. Matthew Barclay, Dr. Katie Duncan, and Dr. Azhad Chowdhury for their collaboration, instruction, and companionship in the ultrafast labs.

Finally, I would like to express my appreciation for my graduate committee. Thanks to Dr. Bill Knowlton for all of the encouragement and for always advocating on my behalf, Dr. Bernard Yurke for always having time to entertain questions and having great explanations, Dr. Daniel Turner for informative and entertaining discussions, and Dr. Joseph Melinger his support and collaboration. Finally, I would like to give a special thanks to my main supervisor and committee co-chair, Dr. Ryan Pensack. Dr. Pensack has invested tremendous effort into my development as a professional scientist and spectroscopist.

ABSTRACT

The invention and widespread adoption of the digital computer in the last century has led to an era of rapid technological advancement that has continued to the present day. This advancement has been sustained to a large degree by continued miniaturization of the electronic components in microprocessors, which results in increased computing power and energy efficiency. In recent years, this strategy has produced diminishing returns because the cost for each incremental size reduction increases as engineers approach the fundamental scaling limits of silicon-based semiconductor devices. Meanwhile, breakthroughs in DNA nanotechnology hold great promise for a new generation of self-assembled nanodevices with applications in nanoscale computing and quantum computing.

DNA nanotechnology has emerged as a means to realize directed self-assembly of arbitrary nanostructures that can be functionalized with nanoparticles or dyes to create nanophotonic devices. Of particular interest for computing applications are DNA-templated nanophotonic devices in which dye molecules are assembled into designated spatial configurations in order to control the evolution of optically generated excited states. These excited states, known as molecular excitons, arise from electronic interactions between dyes and are sensitive to the proximity and orientation of dyes relative to one another. To date, a number of DNA-templated excitonic devices such as optical switches, sensors, and energy relays have been demonstrated.

The function of the above devices may be enhanced by using DNA to assemble closely-spaced assemblies of dyes, known as dye aggregates, that experience close-range coherent interactions that can drastically alter their properties with respect to the isolated dye. For example, coherent interactions can result in spectral shifts in absorption and

fluorescence, modulation of absorption and fluorescence intensity, and facilitate lossless energy transfer. These properties are extremely sensitive to the mutual orientation and separation of the constituent dyes, and the structure-property relationships of DNA templated dye aggregates are an active area of research.

Here, we present three photophysical studies of cyanine dye aggregates assembled on DNA. In the first study, we use DNA to assemble heteroaggregate tetramers of the cyanine dyes Cy5 and Cy5.5. We observe that changing the ratio of Cy5 to Cy5.5 within the heteroaggregates produces incremental shifts in their optical absorption frequencies that are reminiscent of alloying. In the second study, the excited-state relaxation kinetics of a DNA templated Cy5 dimer and tetramer are compared to those of the monomer. A combination of steady-state and time-dependent absorption spectroscopies indicate that the relaxation kinetics of the aggregates are dominated by a rapid nonradiative relaxation pathway that is introduced upon aggregation. In the third study, a larger set of DNA-templated Cy5 aggregates are studied, including three dimers, a trimer, and a tetramer. We find that nonradiative quenching persists across these structures. We additionally model the aggregate spectra based on their steady-state absorption and circular dichroism spectra to infer a possible relationship between the relaxation kinetics and structural parameters such as intermolecular separation and the number of dyes comprising the aggregate.

TABLE OF CONTENTS

LIST OF TABLES

xi

LIST OF ABBREVIATIONS AND SYMBOLS

σ	Absorption Peak Width
Φ_{EET}	End-to-End Quantum Efficiency
CD	Circular Dichroism
cm^{-1}	Wave Number Unit
D	Debye Unit
DNA	Deoxyribonucleic Acid
E	Transition Energy
EET	Electronic Energy Transfer
ESA	Excited-State Absorption
FRET	Förster Resonance Energy Transfer
fs	Femtosecond
GTA	Global Target Analysis
GSB	Ground-State Bleach
IRF	Instrument Response Function
J	Excitonic Hopping Parameter
KRM	Kühn-Renger-May
$M^{-1}\ cm^{-1}$	Molecular Extinction Unit
meV	Milli-electron Volt
nm	Nanometer
ns	Nanosecond

PAGE	Polyacrylamide Gel Electrophoresis
ps	Picosecond
SAS	Species Associated Spectrum
SE	Stimulated Emission
TA	Transient Absorption
TAS	Transient Absorption Spectroscopy
TCSPC	Time-Correlated Single Photon Counting
TDM	Transition Dipole Moment

CHAPTER ONE: INTRODUCTION

Over half a million years ago, our ancestors created the very first examples of nanotechnology. Early humans used stones to manually chip away flakes from pieces of obsidian and fashioned them into incredibly-sharp blades with edges as fine as three nanometers.[1] Nanomaterials, which are materials with properties arising from their structure on the nanometer scale, have made other isolated appearances in history such as Damascus steel blades with incredible strength,[1] and Roman dichroic glass that appears red or green depending on lighting.[2] However, it was not until the late twentieth century that we possessed the tools and theoretical framework necessary to contemplate engineering at the nanometer scale.

In modern times, nanotechnology is of interest in nearly every industry, from medicine to electronics. The study of the relationships between the structure, properties, performance, and processing of materials with features that range from 1-100 nm is known as nanoscience, and the application of this research to realize nanostructured functional materials and devices is known as nanotechnology. Nanomaterials have become the focus of much research because, at this scale, effects from both quantum confinement and secondary intermolecular forces can be present. The complex interplay between fundamental and secondary physical interactions at the nanoscale gives rise to interesting properties at larger-length scales. These emergent properties are of great technological importance and have become increasingly important within materials science and engineering.

Integrated circuit (IC) technology is the greatest success of nanotechnology by virtually every measure, and is among the greatest technological successes in history. ICs are miniature electric circuits that form the basis of all digital electronics, including devices that incorporate computers such as laptops, phones, and smart appliances. These devices are made by patterning nanoscale features through selective deposition or removal of material from semiconductor substrates such as silicon. The steady advancement of digital electronics over the last several decades has been driven, to a large extent, by breakthroughs in nanotechnology that have enabled continued miniaturization of ICs. Miniaturization has increased the density of elements on a chip, increasing their performance and enabling new applications with a predictable regularity that has allowed hardware and software developers to target their applications to hardware that did not yet exist, but would at a known point in the future. This is the crux of Moore's law,[3] which has had a profound impact on the global economy.

Despite decades of success, there are mounting challenges facing the semiconductor industry that demand new approaches. With each incremental reduction in IC feature size, the associated engineering and tooling have become costlier. Within the next decade, it is expected that fundamental physical limitations will prevent further reduction in the size of IC elements.[4] Additionally, while integrated circuits have become more energy-efficient from miniaturization, the expansion of embedded computers into all aspects of life has more than offset gains in efficiency, and the condition has been set for the electrical demand for computing to outstrip global electrical capacity later this century if current trends hold.[4,5] Therefore, it is necessary to research new materials systems and

device physics in order to fully realize the long-term benefits of further mutual integration of artificial intelligence, sensing, and networking.

An alternative to the current approach to fabricating ICs, which is largely top-down and thus requires expensive and energy-intensive tooling, is to pursue so-called "bottom-up" molecular self-assembly techniques. Bottom-up self-assembly more resembles the processes by which living things grow and reproduce, with structures assembling from molecular subunits via intermolecular forces into forms dictated by thermodynamics. Bottom-up self-assembly has the attractive feature of not necessarily requiring expensive tooling or extreme processing conditions to realize functional nanoscale materials. Among molecular self-assembly techniques under development, DNA nanotechnology has emerged in recent years as the leading approach to realizing arbitrarily-shaped nanoscale structures with feature sizes as small as the 2.4 nm width of the DNA double helix.[6-10] The ability of DNA to assemble into arbitrary shapes derives from the high specificity of interactions that can be realized through base-pairing. Dozens of DNA sequences can exist in a solution with very little interaction if their respective sequences are judiciously chosen. Conversely, with the proper choice of base sequence, DNA oligonucleotides can assemble into branched junctions with domains that are complementary to multiple other oligonucleotides.[11,12] These addressable branch points thereby enable self-assembly into arbitrary three-dimensional structures.

Importantly, DNA is also amenable to a variety of chemical modifications, including fluorescent dye molecules. Dye molecules absorb visible light and convert the energy to electronic excited states, thus confining the energy of a photon to a few nm^3. Dyes in close proximity (i.e., a few nm) can transfer excitations between them through

resonant Coulombic interactions. These delocalized excited states are known as molecular excitons. By using DNA as a molecular scaffold, dye molecules can be assembled into molecular excitonic devices that operate well below the diffraction limit of light. For example, recent work demonstrated DNA-templated all-optical excitonic switches that could out-perform CMOS field effect transistors in key performance metrics such as device volume, switching rate, and switching energy.[13] Theoretical work also suggests that dye-based excitonic logic gates could be used for signal processing or computation.[14,15] Additionally, DNA-templated dye networks have been contemplated as sources of true random numbers with a controllable distribution for application in the emerging field of stochastic computing.[16]

The performance of devices for the above applications could be substantially enhanced if dye aggregates, which are closely packed supramolecular assemblies of dye molecules, can be incorporated into their design. This is because dye aggregates exhibit optical properties that can vary drastically from the isolated dye.[17] For example, dye aggregates often exhibit shifts and narrowing of their absorption and emission spectra as well as enhanced or suppressed emission strength.[18-21] Furthermore, excitons in dye aggregates can exhibit the emergent property of coherent delocalization, meaning they spread out in a wave-like manor across multiple dyes. Coherent exciton delocalization in dye aggregates, is of interest for increasing excitonic energy transfer efficiency as well as quantum information applications.[22-24] The optical properties and extent of coherent exciton delocalization in dye aggregates are highly sensitive to structural parameters such as the mutual orientation of dyes, intermolecular separation, and number of dyes comprising the aggregate.[21,25] Thus, there is increasing interest in leveraging molecular

scaffolds such as DNA to direct the assembly of dye aggregates into designated structures to access properties not observed in the isolated dye.

While many examples of dye aggregates assembled on DNA have been demonstrated,[26-33] methodologies for controlling their structure and resulting properties are still developing. At the current stage of development, it is critical to understand how the optical properties and excited-state dynamics of DNA-templated dye aggregates are related to parameters that can be controlled, and thus engineered. Additionally, understanding the relationship between dye aggregate structural parameters and their excited state dynamics is critical because these affect the energy transfer and fluorescence emission characteristics. This dissertation focuses on these two areas of research, and the following chapters contribute new insight to outstanding questions or problems in the field of DNA-templated dye aggregates.

One desired feature of dye aggregates is the ability to control their electronic transition energies to suit a specific application. For example, dye aggregates with different transition energies could be used to differentiate the inputs of an excitonic logic gate, allowing for the presence or absence of certain wavelengths to control the input state of the logic gate. A similar strategy could be to read out the output state of an excitonic logic gate via fluorescence from dye aggregates at specific wavelengths. Strategies to engineer the electronic structures of dye aggregates often involve controlling how the dyes are positioned and oriented in space relative to one another, i.e., packed. Historically, changes in aggregate packing have been achieved by adding chemical substituents to monomeric dyes and/or altering the solvent conditions in order to alter the packing geometry to favor structures such as nanofibers,[34-36] and nanotubes.[37,38] Using DNA to assemble dye

aggregates results in several additional strategies for affecting their electronic structures. For example, the intermolecular spacing can be coarsely controlled by varying the number of bases between dyes,[39,40] with a maximum resolution of the 0.34 nm base-spacing occasionally observed.[41] Altering the nucleotide sequence in the immediate vicinity of the dyes has also been observed to alter the electronic structure of aggregates.[42] More recently, researchers have explored the hypothesis that inducing strain in the DNA template can alter the electronic structure of dimers by pushing the dyes together or pulling them apart.[43]

The above strategies focus on altering dye packing within dye aggregates to affect the electronic structure; however, another strategy for controlling electronic structure of aggregates is to leverage the specificity of dye placement afforded by DNA templating to assemble aggregates of chemically-distinct dyes. These aggregates are known as heteroaggregates, whereas aggregates composed of chemically identical dyes are known as homoaggregates. Foundational work on DNA-templated heteroaggregates shows that the optical absorption spectra of heteroaggregates are intermediate between the corresponding two homoaggregates, and that the theory used to describe the optical spectra of homoaggregates generally applies to heteroaggregates.[27,44,45] However, the extent of tunability has not been explored, as only heteroaggregates with a 1:1 compositional ratio have been examined. Even less is known about how heteroaggregation affects nonradiative relaxation processes that are often enhanced in aggregates compared to monomeric dyes. **Chapter 2** details a study in which we explore these gaps in understanding. Specifically, we utilize four-armed DNA Holliday junctions to construct strongly-coupled heterotetramers of the dyes Cy5 and Cy5.5. We measure the absorption and fluorescence emission spectra of every tetramer permutation of Cy5 and Cy5.5. Additionally, we

measure the excited-state relaxation dynamics of a subset of these structures using spectrally-resolved transient absorption spectroscopy.

In addition to electronic structure, the excited-state dynamics of DNA-templated aggregates are of critical importance to their application in nanotechnology. Properties such as fluorescence quantum yield and energy transfer rates and efficiencies are largely determined by the kinetic competition between radiative and nonradiative decay processes of a dye or aggregate.[46] In the simplest case in which decay occurs directly to the ground state and secondary excited populations are not generated, a population of excited dye molecules or aggregates will relax to the ground state according to first-order kinetics. The rate constant associated with the first-order kinetics is the sum of the radiative and nonradiative relaxation rates. For dyes and aggregates, it is possible to estimate the radiative relaxation rate by integrating the portion of the absorption spectrum expressed in units of molar extinction that corresponds to the lowest-energy electronic transition.[47] The nonradiative decay rate, however, is difficult to estimate because it is itself the sum of all of the active nonradiative decay pathways, and thus can vary greatly from the influence of the local environment. Since it is possible for both the radiative and nonradiative decay rates of an aggregate to differ from the monomeric dye, interpreting the as-measured excited-state lifetime is challenging. In **Chapter 3**, we use a combination of steady-state and time-resolved spectroscopic techniques to determine the radiative and nonradiative decay rates of a DNA-templated Cy5 monomer as well as place bounded estimates of these quantities for a dimer and tetramer. In **Chapter 4**, we measured the excited-state lifetimes of a larger set of DNA-templated Cy5 aggregates and analyze them in combination with

structural modeling in order to relate the observed lifetimes to aggregate structural parameters.

Another underexplored challenge in DNA-templated dye aggregates is detecting the presence of undesired subpopulations, i.e., heterogeneity. The use of a large (relative to a dye molecule) DNA template and tethering linker chemistry complicates the local solution environment experienced by dyes compared to the environment experienced by dyes that spontaneously associate in solution. This more complicated local environment may lead to multiple discrete meta-stable dye packing configurations with distinct optical spectra and relaxation dynamics. Identifying the presence of these solutions is critical to properly interpreting experimental spectra. In **Chapters 2**, **3**, and **4**, we make several observations that indicate the presence of monomer and aggregate subpopulations in DNA-templated cyanine-aggregate solutions. In **Chapter 4**, we propose two mechanisms related to dynamic processes in the DNA Holliday junction templates to account for monomer and aggregate subpopulations observed in our solutions. Finally, in **Chapter 5**, the results of chapters 2, 3, and 4 are summarized, and several possible directions for future studies are proposed.

REFERENCES

(1) Eglash, R. "Nanotechnology and Traditional Knowledge Systems In Donnie Maclurcan and Natalia Radywyl (Ed) Nanotechnology and Global Sustainability, CRC Press 2011 Nanotechnology and Traditional Knowledge Systems. In *Nanotechnology and Global Sustainability*; Maclurcan, D., Radywyl, N., Eds.; CRC Press, 2012; pp 45–68. https://doi.org/https://doi.org/10.1201/9781315217260.

(2) Barber, D. J. An Investigation of the Origin of the Colour of the Lycurgus Cup by Analytical Transmission Electron Microscopy. *Archaeometry* **1990**, *1*, 33–45.

(3) Moore, G. E. Cramming More Components onto Integrated Circuits. *Electronics* **1965**, *38* (8), 114.

(4) INTERNATIONAL ROADMAP FOR DEVICES AND SYSTEMS EXECUTIVE SUMMARY. *IEEE* **2022**.

(5) Rebooting the IT Revolution: A Call to Action. *Semicond. Ind. Assoc.* **2015**.

(6) Rothemund, P. W. K. Folding DNA to Create Nanoscale Shapes and Patterns. *Nature* **2006**, *440* (7082), 297–302. https://doi.org/10.1038/nature04586.

(7) Wei, B.; Dai, M.; Yin, P. Complex Shapes Self-Assembled from Single-Stranded DNA Tiles. *Nature* **2012**, *485*, 623–627. https://doi.org/10.1038/nature11075.

(8) Ke, Y.; Ong, L. L.; Shih, W. M.; Yin, P. Three-Dimensional Structures Self-Assembled from DNA Bricks. *Science (80-.).* **2012**, *338*, 1177–1184.

(9) Cademartiri, L.; Bishop, K. J. M. Programmable Self-Assembly. *Nat. Mater.* **2015**, *14*. https://doi.org/10.1038/nmat4184.

(10) Seeman, N. C. *Structural DNA Nanotechnology*; Cambridge University Press: Cambridge, **2016**.

(11) Seeman, N. C.; Kallenbach, N. R. Design of Immobile Nucleic Acid Junctions. *Biophys. J.* **1983**, *44* (2), 201–209. https://doi.org/10.1016/S0006-3495(83)84292-1.

(12) Seeman, N. C. DNA in a Material World. **2003**, *421* (January), 1122–1126.

(13) Kellis, D. L.; Sarter, C.; Cannon, B. L.; Davis, P. H.; Graugnard, E.; Lee, J.; Pensack, R. D.; Kolmar, T.; Jäschke, A.; Yurke, B.; et al. An All-Optical Excitonic Switch Operated in the Liquid and Solid Phases. *ACS Nano* **2019**, *13* (3), 2986–2994. https://doi.org/10.1021/acsnano.8b07504.

(14) Boulais, E.; Sawaya, N. P. D.; Veneziano, R.; Andreoni, A.; Banal, J. L.; Kondo, T.; Mandal, S.; Lin, S.; Schlau-Cohen, G. S.; Woodbury, N. W.; et al. Programmed Coherent Coupling in a Synthetic DNA-Based Excitonic Circuit. *Nat. Mater.* **2018**, *17* (2), 159–166. https://doi.org/10.1038/NMAT5033.

(15) Sawaya, N. P. D.; Rappoport, D.; Tabor, D. P.; Aspuru-Guzik, A. Excitonics: A Set of Gates for Molecular Exciton Processing and Signaling. *ACS Nano* **2018**, *12* (7), 6410–6420. https://doi.org/10.1021/acsnano.8b00584.

(16) Wang, S.; Lebeck, A. R.; Dwyer, C. L. Nanoscale Resonance Energy Transfer-Based Devices for Probabilistic Computing. *IEEE Micro* **2015**, *35* (5), 72–84.

(17) Würthner, F.; Kaiser, T. E.; Saha-Möller, C. R. J-Aggregates: From Serendipitous Discovery to Supramolecular Engineering of Functional Dye Materials. *Angew. Chemie - Int. Ed.* **2011**, *50* (15), 3376–3410. https://doi.org/10.1002/anie.201002307.

(18) Jelley, E. E. Spectral Absorption and Fluorescence of Dyes in the Molecular State. *Nature* **1936**, *138* (3502), 1009–1010.

(19) Jelley, E. E. Molecular, Nematic and Crystal States of I: I-Diethyl--Cyanine Chloride. *Nature* **1937**, *139* (3519), 631–631.

(20) Scheibe, G. Über Die Veränderlichkeit Der Absorptionsspektren in Lösungen Und Die Nebenvalenzen Als Ihre Ursache. *Angew. Chemie* **1937**, *50* (11), 212–219.

(21) Kasha, M.; Rawls, H. R.; Ashraf El-Bayoumi, M. The Exciton Model in Molecular Spectroscopy. *Pure Appl. Chem.* **1965**, *11* (3–4), 371–392.

(22) Yurke, B.; Elliott, R.; Sup, A. Implementation of a Frenkel Exciton-Based Controlled Phase Shifter. *Phys. Rev. A* **2023**, *107* (1). https://doi.org/10.1103/PhysRevA.107.012603.

(23) Yonetani, Y. Exciton Quantum Dynamics in the Molecular Logic Gates for Quantum Computing. *Chem. Phys.* **2023**, *570*, 111860. https://doi.org/10.1016/j.chemphys.2023.111860.

(24) Wittmann, B.; Wenzel, F. A.; Wiesneth, S.; Haedler, A. T.; Drechsler, M.; Kreger, K.; Köhler, J.; Meijer, E. W.; Schmidt, H. W.; Hildner, R. Enhancing Long-Range Energy Transport in Supramolecular Architectures by Tailoring Coherence Properties. *J. Am. Chem. Soc.* **2020**, *142* (18), 8323–8330. https://doi.org/10.1021/jacs.0c01392.

(25) Ahn, T. S.; Müller, A. M.; Al-Kaysi, R. O.; Spano, F. C.; Norton, J. E.; Beljonne, D.; Bŕdas, J. L.; Bardeen, C. J. Experimental and Theoretical Study of Temperature Dependent Exciton Delocalization and Relaxation in Anthracene Thin Films. *J. Chem. Phys.* **2008**, *128* (5), 1–11. https://doi.org/10.1063/1.2822310.

(26) Wang, M.; Silva, G. L.; Armitage, B. A. DNA-Templated Formation of a Helical Cyanine Dye J-Aggregate. *J. Am. Chem. Soc.* **2000**, *122*, 9977–9986.

(27) Asanuma, H.; Murayama, K.; Kamiya, Y.; Kashida, H. The DNA Duplex as an Aqueous One-Dimensional Soft Crystal Scaffold for Photochemistry. *Bull. Chem. Soc. Jpn.* **2018**, *91* (12), 1739–1748. https://doi.org/10.1246/bcsj.20180278.

(28) Markova, L. I.; Malinovskii, V. L.; Patsenker, L. D.; Häner, R. J- vs. H-Type Assembly: Pentamethine Cyanine (Cy5) as a near-IR Chiroptical Reporter. *Chem. Commun.* **2013**, *49* (46), 5298–5300. https://doi.org/10.1039/c3cc42103a.

(29) Cannon, B. L.; Patten, L. K.; Kellis, D. L.; Davis, P. H.; Lee, J.; Graugnard, E.; Yurke, B.; Knowlton, W. B. Large Davydov Splitting and Strong Fluorescence Suppression: An Investigation of Exciton Delocalization in DNA-Templated Holliday Junction Dye Aggregates. *J. Phys. Chem. A* **2018**, *122* (8), 2086–2095. https://doi.org/10.1021/acs.jpca.7b12668.

(30) Cunningham, P. D.; Kim, Y. C.; Díaz, S. A.; Buckhout-White, S.; Mathur, D.; Medintz, I. L.; Melinger, J. S. Optical Properties of Vibronically Coupled Cy3 Dimers on DNA Scaffolds. *J. Phys. Chem. B* **2018**, *122* (19), 5020–5029.

(31) Barclay, M. S.; Wilson, C. K.; Roy, S. K.; Mass, O. A.; Obukhova, O. M.; Svoiakov, R. P.; Tatarets, A. L.; Chowdhury, A. U.; Huff, J. S.; Turner, D. B.; et al. Oblique Packing and Tunable Excitonic Coupling in DNA-Templated Squaraine Rotaxane Dimer Aggregates. *ChemPhotoChem* **2022**, No. e202200039. https://doi.org/10.1002/cptc.202200039.

(32) Mass, O. A.; Wilson, C. K.; Roy, S. K.; Barclay, M. S.; Patten, L. K.;

Terpetschnig, E. A.; Lee, J.; Pensack, R. D.; Yurke, B.; Knowlton, W. B. Exciton Delocalization in Indolenine Squaraine Aggregates Templated by DNA Holliday Junction Scaffolds. *J. Phys. Chem. B* **2020**, *124*, 9636–9647.

(33) Banal, J. L.; Kondo, T.; Veneziano, R.; Bathe, M.; Schlau-Cohen, G. S. Photophysics of J-Aggregate-Mediated Energy Transfer on DNA. *J. Phys. Chem. Lett.* **2017**, *8* (23), 5827–5833.

(34) Wittmann, B.; Wenzel, F. A.; Wiesneth, S.; Haedler, A. T.; Drechsler, M.; Kreger, K.; Köhler, J.; Meijer, E. W.; Schmidt, H. W.; Hildner, R. Enhancing Long-Range Energy Transport in Supramolecular Architectures by Tailoring Coherence Properties. *J. Am. Chem. Soc.* **2020**, *142* (18), 8323–8330. https://doi.org/10.1021/jacs.0c01392.

(35) Haedler, A. T.; Kreger, K.; Issac, A.; Wittmann, B.; Kivala, M.; Hammer, N.; Köhler, J.; Schmidt, H. W.; Hildner, R. Long-Range Energy Transport in Single Supramolecular Nanofibres at Room Temperature. *Nature* **2015**, *523* (7559), 196–199. https://doi.org/10.1038/nature14570.

(36) Bricker, W. P.; Banal, J. L.; Stone, M. B.; Bathe, M. Molecular Model of J-Aggregated Pseudoisocyanine Fibers. *J. Chem. Phys.* **2018**, *149*, 024905. https://doi.org/10.1063/1.5036656.

(37) Kirstein, S.; Daehne, S. J-Aggregates of Amphiphilic Cyanine Dyes: Self-Organization of Artificial Light Harvesting Complexes. *Int. J. Photoenergy* **2006**, *2006*, 1–21. https://doi.org/10.1155/IJP/2006/20363.

(38) Wan, Y.; Stradomska, A.; Knoester, J.; Huang, L. Direct Imaging of Exciton Transport in Tubular Porphyrin Aggregates by Ultrafast Microscopy. *J. Am. Chem. Soc.* **2017**, *139*, 7287–7293. https://doi.org/10.1021/jacs.7b01550.

(39) Nicoli, F.; Roos, M. K.; Hemmig, E. A.; Di Antonio, M.; De Vivie-Riedle, R.; Liedl, T. Proximity-Induced H-Aggregation of Cyanine Dyes on DNA-Duplexes. *J. Phys. Chem. A* **2016**, *120* (50), 9941–9947. https://doi.org/10.1021/acs.jpca.6b10939.

(40) Cannon, B. L.; Kellis, D. L.; Patten, L. K.; Davis, P. H.; Lee, J.; Graugnard, E.; Yurke, B.; Knowlton, W. B. Coherent Exciton Delocalization in a Two-State DNA-Templated Dye Aggregate System. *J. Phys. Chem. A* **2017**, *121* (37), acs.jpca.7b04344. https://doi.org/10.1021/acs.jpca.7b04344.

(41) Kato, T.; Kashida, H.; Kashida, H.; Yada, H.; Okamoto, H.; Hiroyuki, A. Development of a Robust Model System of FRET using Base Surrogates Tethering Fluorophores for Strict Control of their Position and Orientation within DNA Duplex. *J. Am. Chem. Soc.* **2013**, 135(2), 741-750.

(42) Cunningham, P. D.; Kim, Y. C.; Díaz, S. A.; Buckhout-White, S.; Mathur, D.; Medintz, I. L.; Melinger, J. S. Optical Properties of Vibronically Coupled Cy3 Dimers on DNA Scaffolds. *J. Phys. Chem. B* **2018**, *122* (19), 5020–5029. https://doi.org/10.1021/acs.jpcb.8b02134.

(43) Hart, S. M.; Wang, X.; Guo, J.; Bathe, M.; Schlau-Cohen, G. S. Tuning Optical Absorption and Emission Using Strongly Coupled Dimers in Programmable DNA Scaffolds. *J. Phys. Chem. Lett.* **2022**, *13*, 1863–1871. https://doi.org/10.1021/acs.jpclett.1c03848.

(44) Kashida, H.; Asanuma, H.; Komiyama, M. Alternating Hetero H Aggregation of Different Dyes by Interstrand Stacking from Two DNA– Dye Conjugates**.

12

Angew. Chem. **2004**, *43*, 6522–6525. https://doi.org/10.1002/anie.200460870.

(45)   Fujii, T.; Kashida, H.; Asanuma, H. Analysis of Coherent Heteroclustering of Different Dyes by Use of Threoninol Nucleotides for Comparison with the Molecular Exciton Theory. *Chem. - A Eur. J.* **2009**, *15*, 10092–10102. https://doi.org/10.1002/chem.200900962.

(46)   Clegg, R. M. Fluorescence Resonance Energy Transfer and Nucleic Acids. *Methods Enzymol.* **1992**, *211*, 353–388.

(47)   Strickler, S. J.; Berg, R. A. Relationship between Absorption Intensity and Fluorescence Lifetime of Molecules. *J. Chem. Phys.* **1962**, *37* (4), 814–822

CHAPTER TWO: TUNABLE ELECTRONIC STRUCTURE VIA DNA-TEMPLATED

HETEROAGGREGATES OF TWO DISTINCT CYANINE DYES

This chapter is published by the American Chemical Society in *Journal of Physical*

Chemistry C and should be referenced appropriately

Reference:

Huff, J. S.; Díaz, S. A.; Barclay, M. S.; Chowdhury, A. U.; Chiriboga, M.; Ellis, G. A.; Mathur, D.; Patten, L. K.; Roy, S. K.; Sup, A.; Biaggne, A.; Rolczynski, B. S.; Cunningham, P. D.; Li, L.; Lee, J.; Davis, P. H.; Yurke, B.; Knowlton, W. B.; Medintz, I.; Turner, D. B.; Melinger, J. S.; Pensack, R. D., Tunable Electronic Structure via DNA-Templated Heteroaggregates of Two Distinct Cyanine Dyes, *Journal of Physical Chemistry C* **2022**, 126 (40), 17164-17175.

*This chapter includes modifications from the originally published version.

2.1 Abstract:

Molecular excitons are useful for applications in light harvesting, organic optoelectronics, and nanoscale computing. Electronic energy transfer (EET) is a process central to the function of devices based on molecular excitons. Achieving EET with a high quantum efficiency is a common obstacle to excitonic devices, often owing to the lack of donor and acceptor molecules that exhibit favorable spectral overlap. EET quantum efficiencies may be substantially improved through the use of heteroaggregates—aggregates of chemically distinct dyes—rather than individual dyes as energy relay units. However, controlling the assembly of heteroaggregates remains a significant challenge. Here, we use DNA Holliday junctions to assemble homo- and hetero-tetramer aggregates of the prototypical cyanine dyes Cy5 and Cy5.5. In addition to permitting control over the number of dyes within an aggregate, DNA-templated assembly confers control over aggregate composition, i.e., the ratio of constituent Cy5 and Cy5.5 dyes. By varying the ratio of Cy5 and Cy5.5, we show that the most intense absorption feature of the resulting tetramer can be shifted in energy over a range of almost 200 meV (1,600 cm^{-1}). All tetramers pack in the form of H-aggregates and exhibit quenched emission and drastically reduced excited-state lifetimes compared to the monomeric dyes. We apply a purely electronic exciton theory model to describe the observed progression of the absorption spectra. This model agrees with both the measured data and a more-sophisticated vibronic model of the absorption and circular dichroism spectra, indicating that Cy5 and Cy5.5 heteroaggregates are largely described by molecular exciton theory. Finally, we extend the purely electronic exciton model to describe an idealized J-aggregate based on Förster

resonance energy transfer (FRET) and discuss the potential advantages of such a device over traditional FRET relays.

2.2 Introduction

Molecular excitons are essential to applications in light harvesting,[1,2] organic optoelectronics,[3] and nanoscale computing.[4–10] In light harvesting and organic optoelectronics, for example, solar photons are converted into molecular excitons that undergo several energy transfer steps from the site of initial photoexcitation to the reaction center or charge-transfer interface where they are converted into reaction products or photocurrent. In nanoscale computing, molecular excitons carry information and propagate between optical inputs, active elements (such as logic gates), and optical outputs via energy transfer. Each of these applications requires an overall high efficiency, and therefore each step needs to be as efficient as possible. Thus, strategies to increase the efficiency of energy-transfer steps are desirable to improve overall performance.

There are several parameters that determine the efficiency of electronic energy transfer (EET) of molecular excitons, which leads to a number of approaches to improve EET efficiency. At the most general level, the efficiency of EET depends on kinetic competition between the rate of EET and rate of excited-state decay. Therefore, the EET efficiency can be improved by increasing the rate of EET or by decreasing the rate of excited-state decay. The rate of EET is the rate at which an exciton on a donor incoherently hops to a nearby, unexcited acceptor. The rate of EET, which, in certain limits, is described by Förster resonance energy transfer (FRET),[11–15] depends on the coupling strength between the donor and acceptor along with the overlap between the donor emission and the acceptor absorption spectra.[13,16,17] Thus, the rate of EET can be increased by increasing the coupling strength between the donor and acceptor. However, this approach has practical limits as FRET is only applicable in the limit of weak coupling. Another way in which the

rate of EET can be increased is by improving the spectral overlap of the donor and acceptor. For example, dyes can be chemically modified to alter their electronic structure for improved spectral overlap. Chemically modifying dye structure, however, can be challenging in the case where several successive steps are necessary to achieve long-range spatial separation of the electronic excitation energy. An alternative approach is to use molecular dye aggregates as the building blocks for long-range and spatially-directed energy transfer. The transition energies of dye aggregates can be tuned and they can exhibit more intense absorption and emission, both of which are desirable for improving spectral overlap.[18,19] Examples of rapid long-range and spatially-directed energy transfer facilitated by aggregates can be found in nature in the photosynthetic light harvesting complexes of certain extremophile bacteria.[20]

One way to tune electronic structure is by assembling aggregates of one type of dye and modifying their packing. Dye packing determines the orientation of the constituent dye transition dipole moments (TDMs), which in turn governs the aggregate's transition energies and absorption and emission intensity.[21–24] For example, when TDMs orient in an end-to-end configuration, the resulting J-aggregate energy levels split and absorption intensity is redistributed to the lower energy transition, leading to redshifted absorption features relative to the monomer (**Figure 2.1A**). Similarly, when TDMs orient face-to-face in a H-aggregate configuration, the absorption intensity is redistributed to the higher energy transition, resulting in blueshifted absorption features.

18
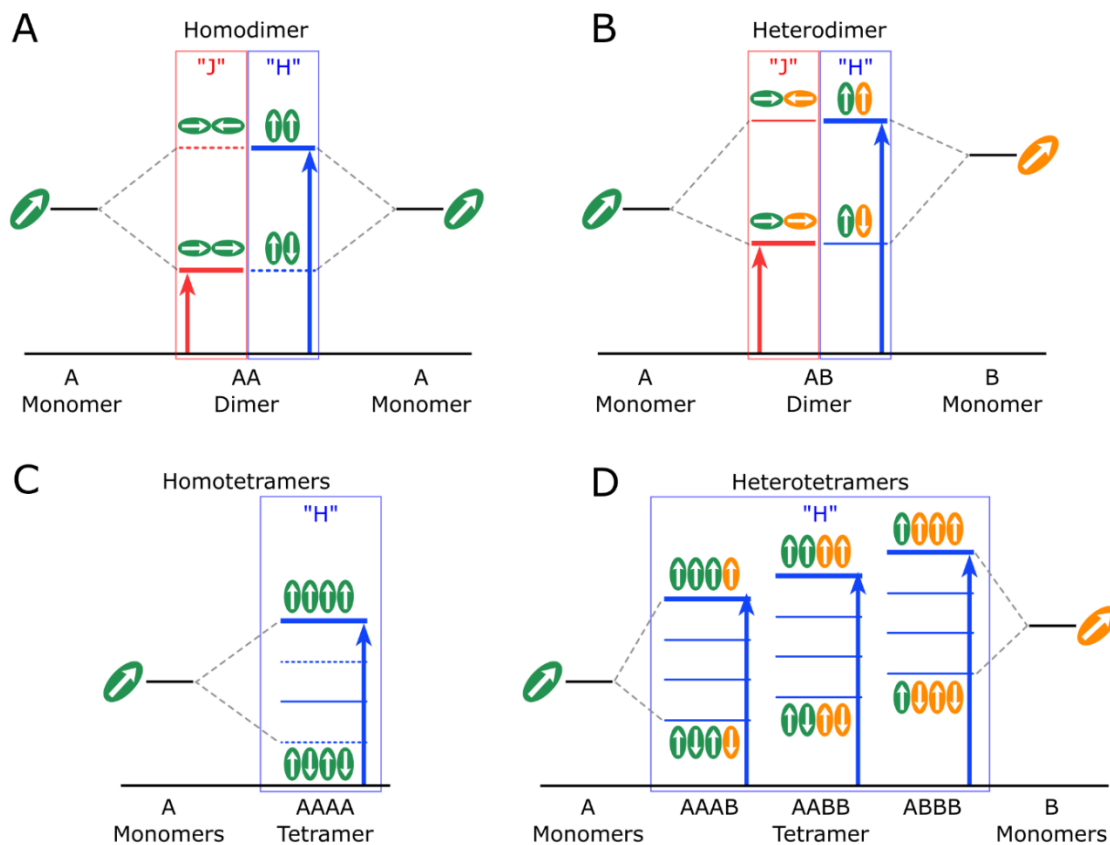
Figure 2.1. Energy-level diagrams depicting monomer electronic states and associated dimer and tetramer aggregate excitonic states. **(A)** Energy-level diagram for an ideal molecular dimer composed of two identical monomers, i.e., a homodimer, packing in the form of J- and H- aggregates. As a result of excitonic coupling between the two monomers, two new excitonic states are formed with energies and transition dipole moment (TDM) amplitudes dependent on the geometric arrangement of the monomers. The monomers comprising the dimer are represented as green ovals and include TDM vectors as white arrows along the molecular long axis (i.e., assuming a rod-like shape for the molecule). There are two distinct packing arrangements for J- and H-aggregates, resulting in four total distinct packing arrangements. A cartoon schematic for each of these packing arrangements, i.e., the geometric arrangement of the monomers, is shown next to the corresponding excitonic state. Excitonic states able and unable to optically couple to the ground state are depicted as thick solid lines and thin dashed lines, respectively. The higher- and lower-energy excitonic transitions are forbidden for J- and H-aggregates, respectively. Optically-allowed transitions are shown as red and blue arrows, respectively. **(B)** Energy level diagram for an ideal molecular dimer composed of two different monomers, i.e., a heterodimer, packing in the form of J- and H-aggregates. The TDMs of monomers A and B are represented as white vectors enclosed in green and orange ovals, respectively. As in the homodimer, excitonic coupling between the two monomers produces two new excitonic states, but, due to the nature of heteroaggregate coupling, the transitions to the optically forbidden states become weakly allowed in

heteroaggregates and are shown as thin solid lines. Because there is only one composition for the heterodimer, i.e., AB, there is no ability to further tune the energies of these states. (C) Energy level diagram for an ideal molecular tetramer composed of four identical monomers, i.e., a homotetramer, packing in the form of an H-aggregate. As a result of excitonic coupling between the four monomers, four new excitonic states result. For ease of viewing, the geometric arrangement of the monomers is only shown for the highest- and lowest-energy states. (D) Energy level diagram for an ideal molecular tetramer composed of two different monomers, i.e., a heterotetramer, packing in the form of an H-aggregate. Excitonic coupling between the four monomers produces four new excitonic states; as in the case of the heterodimer, the optical transitions that are forbidden in the homotetramer (i.e., the three lower energy states) are weakly allowed. Because there are three different compositions for the heterotetramer, i.e., AAAB, AABB, and ABBB, the energies of the heterotetramer excitonic states can be tuned. Specifically, by adjusting the ratio of the two monomers comprising the heterotetramer, the excitonically-split states can be tuned to higher or lower energies.

An alternative, albeit less explored, way of tuning electronic structure is by assembling aggregates of two chemically distinct dyes. It is instructive to first consider the case where we have two homoaggregate dimers corresponding to two chemically distinct dyes, which, for simplicity, we assume to have identical TDMs and exhibit the same packing arrangement. In the case of J-aggregate homodimers of dyes A and B, the lowest-energy optical transition of the two homodimers, AA and BB, are lower in energy compared with the transition energy of the corresponding monomer and the dimers exhibit enhanced radiative decay rates. Thus, while there is some enhancement in radiative decay rate, there is no gain in number of distinct transition energies (i.e., two distinct monomer transition energies compared with two distinct homodimer transition energies). Now let us consider a third possibility—the heterodimer, AB (**Figure 2.1B**). The heterodimer will have new electronic states intermediate in energy between those of the two homodimers and, in the case of J-aggregation, maintain enhanced radiative decay rates and increased absorption intensity. In the case of the heterodimer, we now have additional electronic

structure tunability without the need for a third chemically distinct dye. This concept can be extended further to higher-order aggregates, such as tetramers. As in the homodimer, the homotetramer (**Figure 2.1C**) offers no gain in the number of distinct transition energies. That is, four distinct monomer transition energies correspond to four distinct homotetramer transition energies, one of which is shown in **Figure 2.1C**. In contrast, for a set of heterotetramers consisting of different combinations of two chemically distinct dyes, five distinct transition energies are possible. Specifically, the three distinct transition energies that correspond to the heterotetramers (i.e., AAAB, AABB, and ABBB) are shown in **Figure 2.1D**, and there are two additional distinct transition energies corresponding to the two homotetramers (i.e., AAAA and BBBB). We now have added tunability—the energy difference between the distinct transition energies is smaller—meaning that we can tune electronic structure on a finer scale. It is important to mention that the possibility of assembling high-order aggregates, such as heterotetramers, is not unrealistic, as studies on methyl red aggregates,[25] merocyanine aggregates,[26] and crystalline polyacenes[27] have indicated that the spatial extent of exciton delocalization in aggregates of these dyes can encompass as many as six, eight, and ten dyes, respectively. The challenge in implementing high-order heteroaggregates thus far has not been spatial extent of exciton delocalization— rather, it has been in controlling their assembly.

A promising way of assembling heteroaggregates involves harnessing the programmability and bottom-up self-assembly of DNA. Using DNA nanotechnology, oligonucleotides with specific sequences can be designed to self-assemble into a variety of low-dimensional structures such as multi-armed junctions,[28] dendrimers,[29] hairpins,[30] and loops.[31] Much larger DNA structures with sizes on the order of hundreds of nanometers

have also been realized through DNA origami,[32] and similarly large vesicles, ribbons, and star-shaped structures have been self-assembled using chemically modified, amphiphilic duplex DNA where the ends are hydrophobic and the interior is hydrophilic.[33,34] In addition to having enormous structural diversity, DNA is amenable to a vast number of chemical modifications including dye labelling. By chemically attaching dyes to the DNA backbone, it is possible to bring dyes into close proximity at subnanometer separations. Through DNA templating, the aggregate size and composition can also be controlled, which are distinct advantages over solution-based assembly of aggregates. To date, DNA has been used to systematically examine the structure and dynamics of a number of strongly-coupled homoaggregates,[35–44] with cyanines representing an exceptional class of dyes facilitating the assembly and characterization of excitonically-coupled dye aggregates.[35,36,42,45–47] Despite the relative ease with which DNA can be used to assemble heteroaggregates, only a very small subset of studies on DNA templated dye aggregates have included heteroaggregates.[46,48–50] Further, these studies largely focused on the steady-state optical properties and electronic structure of the DNA-templated heteroaggregates, without details of the excited-state dynamics.

In this work, we show how to systematically tune electronic structure in a series of DNA-templated tetramer aggregates by varying the aggregate composition. We use Cy5 and Cy5.5, two chemically distinct and prototypical dyes used in excitonics and imaging, and assemble the dyes into a series of homo- and hetero-tetramer aggregates (**Scheme 2.1**). We chose these specific dyes for their compatibility, which arises from their similar chemical structures, large transition dipole moment amplitudes,[51] overall similar optical spectra (in spectral range and shape),[43] and their facile incorporation into DNA

oligonucleotides.[52] We find using steady-state absorption and circular dichroism (CD) spectroscopy that all of the tetramers exhibit strong excitonic interactions and that the constituent dyes pack in the form of H-aggregates. Remarkably, as the composition of the tetramer is varied, i.e., by increasing the Cy5.5 content, we observe a progressive shift of the primary absorption band to longer wavelengths over an energy span of ~200 meV (~1,600 cm^{-1}). We find via steady-state fluorescence measurements that all of the tetramers exhibit quenched fluorescence. This result, combined with a more than tenfold reduction in excited state lifetimes of the tetramers compared to the monomers as measured via transient absorption, indicates that the tetramers exhibit enhanced nonradiative decay relative to the monomers. We use a purely electronic model based on molecular exciton theory to explain the progression of the most-intense and highest-energy absorption band of each homo- and hetero-tetramer aggregate. In parallel, we simulate the steady-state absorption and CD spectra via an approach based on the Kühn-Renger-May (KRM) theory, which includes one vibronic mode and produces a packing configuration and excitonic interaction strengths similar to the purely electronic model. We conclude by applying the model to an idealized energy-transfer relay based on a series of J-aggregate homo- and hetero-tetramers, which can transfer electronic excitation energy over a large spatial distance (16 nm) with high quantum efficiency (99.9%).
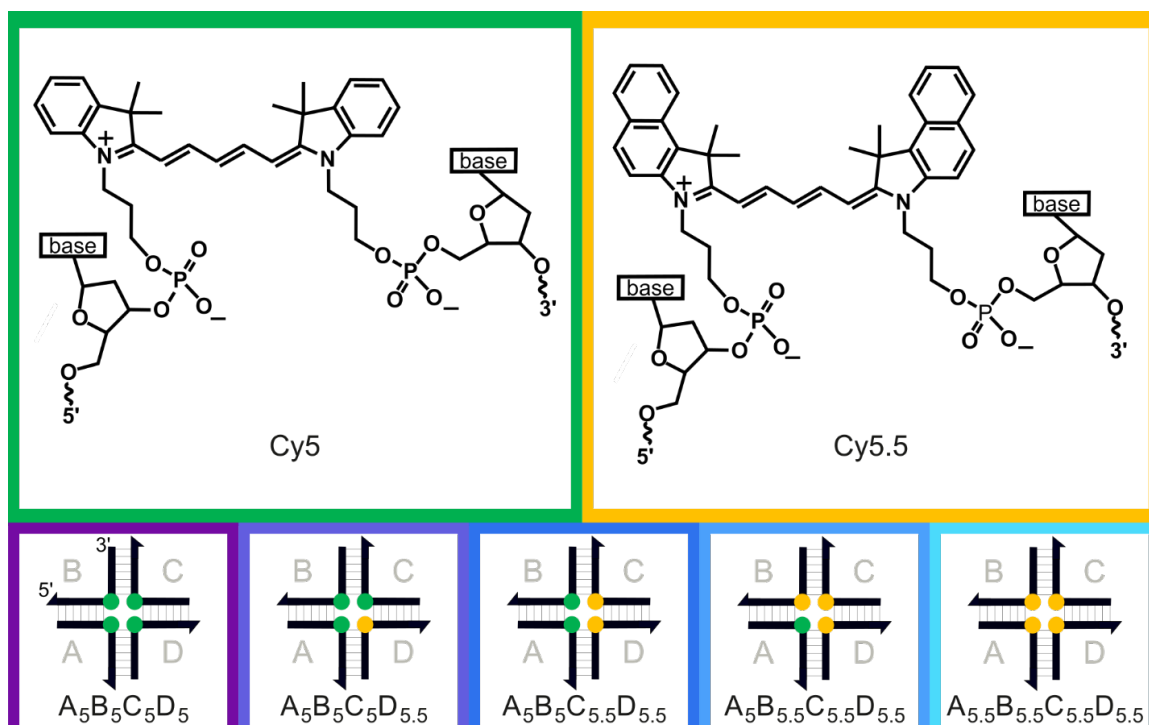
Scheme 2.1. **Chemical structures of dual-phosphoramidite functionalized Cy5 and Cy5.5 (top) and schematic illustrations of Cy5 and Cy5.5 homo- and hetero-tetramer aggregates templated using DNA Holliday junctions (bottom). Cy5 and Cy5.5 are represented as green and yellow circles, respectively. The DNA-dye constructs are composed of four dye-labeled oligonucleotide sequences, with the oligonucleotide sequences shown as black lines with the half-arrowhead pointed towards the 5' part of the sequence and with the full sequence provided in Section 2.6.1. Grey lines between oligonucleotides represent hydrogen bonding between complementary nucleobases. The DNA-dye construct configurations include two homotetramers (i.e., $A_5B_5C_5D_5$ and $A_{5.5}B_{5.5}C_{5.5}D_{5.5}$) and three heterotetramers ($A_5B_5C_5D_{5.5}$, $A_5B_5C_{5.5}D_{5.5}$, $A_5B_{5.5}C_{5.5}D_{5.5}$), which are a subset of the sixteen total possible tetramer configurations.**

2.3 Results and Discussion

Electronic structure characterization via steady-state absorption and circular dichroism.

We first used steady-state absorption spectroscopy to characterize the electronic structure of Cy5 and Cy5.5 monomers attached to DNA Holliday junctions. **Section S1** includes details of the oligonucleotide labeling and assembly of the DNA Holliday junctions. Absorption spectra are shown in **Figure 2.2A**. The monomer spectra resemble

one another and are characterized by a prominent lowest-energy absorption band, with less intense vibronic shoulders at shorter wavelengths. The absorption maximum, which we assign to the 0-0 absorption band, and is located at ca. 653 and 695 nm for Cy5 and Cy5.5, respectively. The presence of the additional aryl groups on Cy5.5 extends the size of the conjugated network compared to Cy5 and results in the overall redshifted absorption spectrum. For both dyes, the next-most intense (i.e., 0-1) absorption band is shifted in energy by ~1,100 cm^{-1} (~140 meV), indicating that the electronic transition is coupled to a symmetric CC stretching mode.[53,54] The 0-1 absorption band is more intense for the Cy5.5 monomer, indicating that the displacement between the ground- and lowest-energy excited electronic potential energy surfaces (i.e., S_0 and S_1) is greater for Cy5.5 than Cy5. An important precursor for excitonic interactions (and delocalization) is the transition dipole moment (TDM) amplitude.[22] In order to gain insight into the magnitude of the TDM of the monomers, we measured their extinction spectra. The extinction spectra are useful in this regard because the peak extinction coefficient is generally proportional to the TDM amplitude.[24] The results indicate that Cy5 and Cy5.5 have peak extinction coefficients of ~239,000 and ~230,000 M^{-1} cm^{-1}, respectively, with these values representing the average of the peak extinction coefficient of the monomers attached to each of the four strands of the Holliday junction (**Section S2**). Such large peak extinction coefficients (and similar absorption profiles) are consistent with the large calculated TDM amplitudes of Cy5 and Cy5.5 of ~15-16 D.[51,55,56] Taken together, the results suggest that Cy5 and Cy5.5 are capable of strong excitonic interactions when brought into close proximity (i.e., sub-nm intermolecular separation).
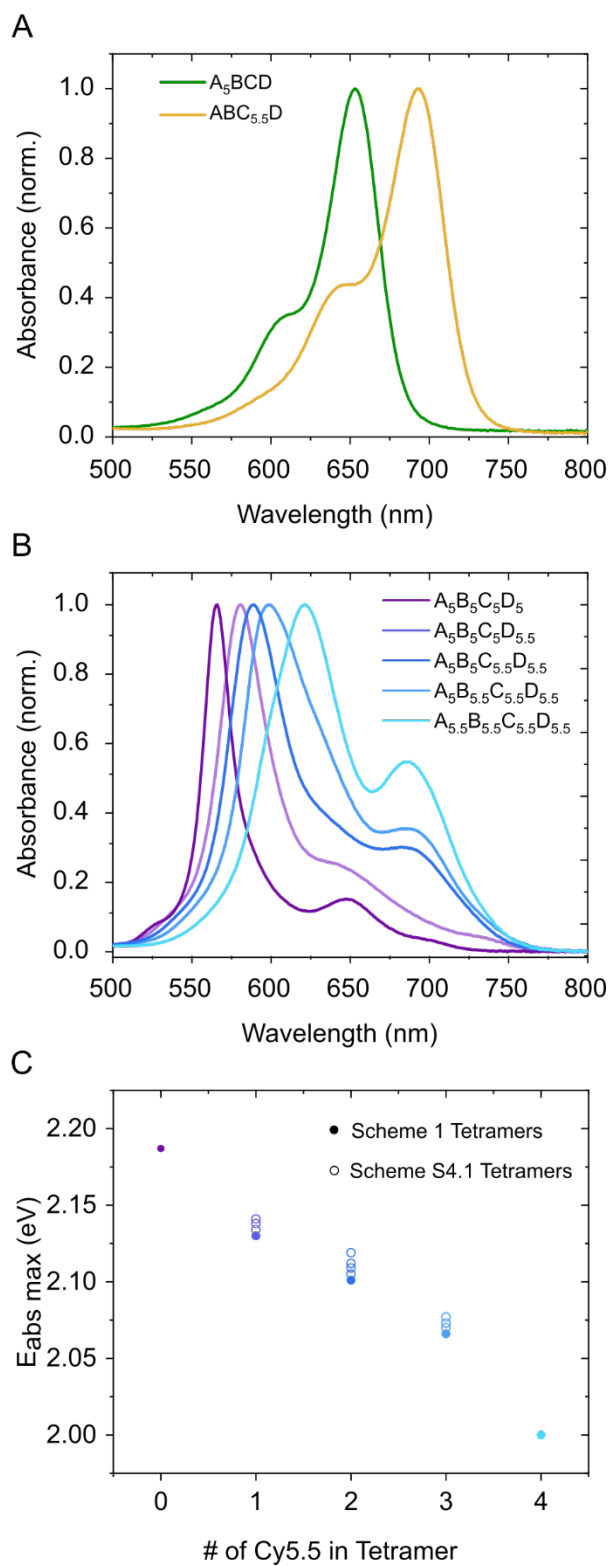
Figure 2.2. **Steady-state absorption spectra of the DNA-templated monomer and heterotetramer structures shown in Scheme 2.1. (A) Steady-state absorption spectra**

of representative Cy5 and Cy5.5 monomers. The absorption spectra of all monomer configurations are plotted in Section 2.6.2. (B) Steady-state absorption spectra of the Cy5-Cy5.5 homo- and hetero-tetramers. (C) The energy of the peak of the most intense absorption band appearing in the spectra of the homo- and hetero-tetramers displayed as a function of Cy5.5 content. Closed circles correspond to the most intense absorption band of the five homo- and hetero-tetramer configurations shown in Scheme 2.1 (and plotted in panel B), while open circles correspond to the remaining eleven heterotetramer configurations shown in Section S5.

Figure 2.2B displays the steady-state absorption spectra of five different homo- and hetero-tetramer aggregates of Cy5 and Cy5.5. In the case of the Cy5 and Cy5.5 homotetramers, we observe that their absorption spectra are drastically different than those of the Cy5 and Cy5.5 monomers. Specifically, in both cases we observe: (i) an intense primary absorption band blueshifted relative to the monomers, which is indicative of strong excitonic interactions between dyes, and (ii) an overall blueshift of the absorption profile, which indicates the dyes are packing in a primarily face-to-face, or H-aggregate, arrangement. Additionally, we find that the most intense absorption band of the Cy5.5 homotetramer is considerably broader than the corresponding absorption band of the Cy5 homotetramer. We also measured the circular dichroism (CD) spectra of the Cy5 and Cy5.5 homotetramers, which provide additional evidence for strong excitonic interactions between dyes (**Section S3**). Specifically, the monomer CD spectra are featureless in the visible range, while the tetramer CD spectra exhibit intense positive and negative peaks in the same spectral region. The position of the CD features in the Cy5 homotetramer at ~569 and 701 nm are consistent with a prior report;[57] the CD features in the Cy5.5 homotetramer are consistent with the interpretation of strong excitonic interactions between dyes and indicate that the additional steric bulk via the introduction of the phenyl rings does not compromise these strong excitonic interactions.

Motivated by the evidence of strong excitonic interactions in the homotetramers, we proceeded to assemble and characterize a series of Cy5 and Cy5.5 heterotetramer aggregates (**Figure 2.2B**). In the series, we successively substitute Cy5.5 dyes with Cy5 dyes to result in the following heterotetramers: $A_5B_5C_5D_{5.5}$, $A_5B_5C_{5.5}D_{5.5}$, and $A_5B_{5.5}C_{5.5}D_{5.5}$. Remarkably, just as we saw for the homotetramers, we also observe drastic spectral changes for these heterotetramers, which indicates that the chemically distinct Cy5 and Cy5.5 dyes are capable of strong excitonic interactions (**Section S4**). Specifically, all heterotetramers exhibit an intense primary absorption that is blueshifted relative to both the Cy5 and Cy5.5 monomer absorption maxima, indicating a common H-aggregate packing arrangement (and further indicating that added steric bulk with successive Cy5.5 substitution does not disrupt this common packing arrangement). Additionally, we find that the absorption maxima and widths of the heterotetramers are intermediate between those of the two homotetramers with increasing Cy5.5 substitutions. Specifically, the most-intense transition energy (E) and its associated width (σ) exhibits a gradual progression from high to low energy and narrow to broad width in the order $E_{Cy5(3)Cy5.5(1)} > E_{Cy5(2)Cy5.5(2)} > E_{Cy5(1)Cy5.5(3)}$ and $\sigma_{Cy5(3)Cy5.5(1)} < \sigma_{Cy5(2)Cy5.5(2)} < \sigma_{Cy5(1)Cy5.5(3)}$, respectively.

To investigate the generality of this effect, we characterized all possible heterotetramer configurations. In total, fourteen heterotetramer configurations are possible, with three representative mono-, di-, and tri-Cy5.5 substituted configurations shown in **Scheme 2.1**. **Section S5** displays schematics of the remaining eleven heterotetramer configurations, along with the absorption spectra for all fourteen heterotetramers (including those plotted in **Figure 2.2**). In all cases, i.e., mono-, di-, and tri-Cy5.5 substitution, the absorption spectra of the corresponding heterotetramers are similar. The

major differences include: (i) a slight energy shift of the most intense absorption band (as is evident by comparing the solid and open circles displayed in **Figure 2.2C**), and (ii) changes in absorption intensity in the vicinity of where the Cy5 and Cy5.5 monomers absorb. The former observation, combined with the observation that the dyes pack in a similar H-aggregate configuration in all cases, suggests that, while the DNA brings the dyes close, the dye packing is driven largely by self-association of the dyes, i.e., strong inter-dye interactions. We attribute the slight energy shift of the absorption maxima either to subtle differences in packing, which impacts excitonic interaction strength, or to differences in the solvent environment, i.e., solvatochromism. The second observation, i.e., that the absorption intensity changes in the vicinity of where the Cy5 and Cy5.5 monomers absorb, is consistent with past observations of a small subpopulation of 'optical' monomers in these materials,[58,59] which we attribute to either DNA 'breathing'[60] or different packing in different DNA conformers.[39,59]

Excited-state electronic structure and dynamics.

We next proceeded to characterize the structure and dynamics of the lowest-energy excited state of the homo- and hetero-tetramer aggregates via steady-state fluorescence spectroscopy. Much like the Cy5 homotetramer solution where extensive quenching compared to the monomer has been observed,[45,57–59] all tetramer solutions exhibit highly quenched fluorescence emission (**Section S6**). Such strongly quenched fluorescence emission is consistent with enhanced nonradiative decay in all of the tetramer structures. Interestingly, the fluorescence emission spectra of the heterotetramer solutions exhibit prominent emission bands peaking in the vicinity of the most intense features in the Cy5 and Cy5.5 monomer emission spectra. Furthermore, the heterotetramer solution emission

spectra strongly resemble a combination of the Cy5 and Cy5.5 monomer emission spectra. As such, we assign the majority of emission coming from the heterotetramer solutions as arising from a small subpopulation of 'optical' monomers, which was confirmed by performing fluorescence excitation spectroscopy measurements (**Section S7**). Previous work suggested that the Cy5 homotetramer solution exhibited an exceptionally weak emission band in the vicinity of ~800 nm.[58] In order to determine whether the heterotetramers are emissive and, if so, the approximate spectral range of emission, we collected fluorescence emission spectra over a range of excitation wavelengths to generate fluorescence emission-excitation surface plots. These measurements indicate that the homo- and hetero-tetramer structures do indeed emit, albeit weakly, in the range of ~750 to 850 nm (**Section S7**).

To gain insight into the mechanism of the enhanced nonradiative decay, we additionally performed femtosecond transient absorption (TA) spectroscopy measurements, which are capable of probing both "bright" and "dark" excited states. In the measurements, a pump pulse excites the sample and a time-delayed probe pulse measures the electronic structure of the electronically excited population. As such, different decay pathways such as direct return to the ground state, conversion to triplet excitations, or conversion to charge carriers can be evaluated. **Figure 2.3A** displays the normalized TA spectra for the homo- and hetero-tetramer aggregate solutions excited near their respective maxima and at a time delay of 3 ps. Each spectrum exhibits an intense negative-going peak corresponding to the ground-state bleach (GSB) of the most intense absorption band. The GSB exhibit the same redshifted progression with increased Cy5.5 content observed in the steady-state absorption spectra (**Figure 2.2B**). Much weaker GSB bands are also visible at

longer wavelengths for each of the solutions, which we attribute to the weak absorption evident in the steady-state absorption. Additionally, we observe positive-going excited-state absorption (ESA) bands on both sides of the primary GSB for all of the tetramers. The ESA to the red of the primary GSB is most apparent as a positive peak at ca. 615 nm in the Cy5 homotetramer TA spectrum. With successive Cy5.5 substitution, this ESA decreases in intensity, possibly as a result of the overlapping primary GSB band, such that tracking its peak position is not possible. On the blue side of the primary GSB, the ESA bands do not follow a smooth progression. Interestingly, the peak position of the ESA band of the $A_5C_5B_5D_{5.5}$ and $A_5B_5C_{5.5}D_{5.5}$ heterotetramers at ~460 nm largely matches that of the Cy5 homotetramer, while the peak position of the ESA band of the $A_5B_{5.5}C_{5.5}D_{5.5}$ heterotetramer at ~500 nm largely matches that of the Cy5.5 homotetramer.
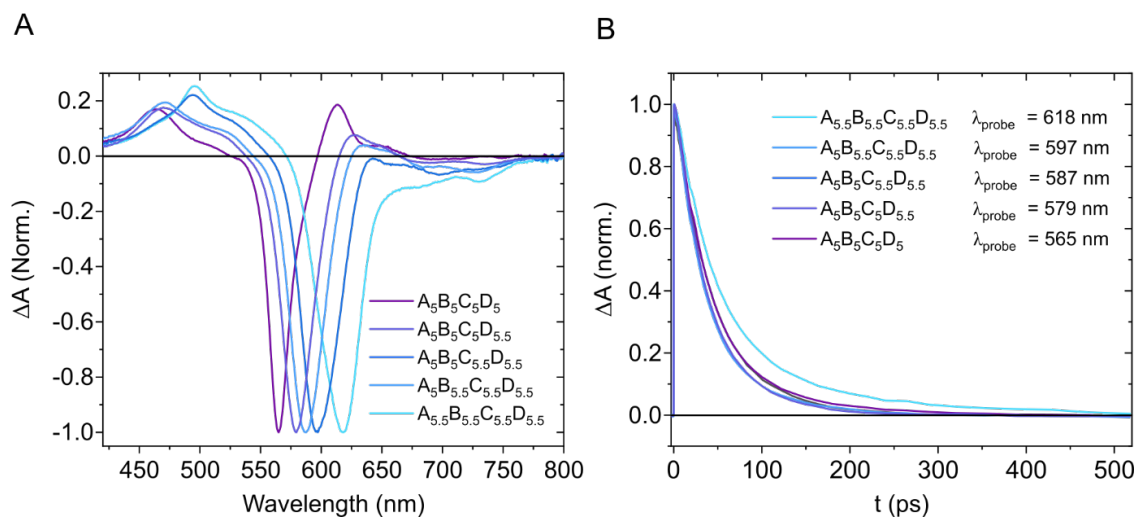
Figure 2.3. **Transient absorption spectra (A) and kinetics traces (B) for a series of tetramers. The TA spectra correspond to a pump-probe delay of 3 ps. The main bleach features reflect the progression of the main absorption steady-state absorption features. For samples $A_5B_5C_{5.5}D_5$, $A_5B_5C_5D_{5.5}$, $A_5B_5C_{5.5}D_{5.5}$, $A_5B_{5.5}C_{5.5}D_{5.5}$, $A_{5.5}B_{5.5}C_{5.5}D_{5.5}$, the excitation wavelengths were centered at ~565, 579, 587, 597, and 618 nm, respectively.**

We next consider the excited-state dynamics of the tetramers. **Figure 2.3B** displays normalized kinetics traces of the decay of the primary GSB feature for each tetramer in the series. The kinetics traces all decay at a similar rate and recover to baseline within 500 ps, with no apparent relationship between the Cy5.5 content of the tetramers and the relaxation rate. The complete recovery of the GSB indicates that the entire excited-state population has returned to the ground state, suggesting that the solutions contain no long-lived "dark" populations. In order to determine the excited-state lifetimes of the tetramer solutions, we performed global target analysis (GTA) on the TA datasets (**Section S8**). GTA can be used to isolate individual spectra and decay kinetics when overlapping signals from multiple populations are embedded in a TA dataset. GTA proceeds according to a kinetic model that states the number of populations and their relationship to one another in terms of the decay pathway (i.e., parallel and sequential). For all homo- and hetero-tetramer TA datasets, we applied a two-component kinetic model that we previously used to model the TA of Cy5 homotetramers.[59] The two-component model includes: (i) an initial component that we assign to a rapid structural relaxation process, as is evident in changes in the excited-state absorption bands, and (ii) a second component that we assign to relaxation to the ground state, based on the decay of all transient spectral features including the GSB bands. The extracted lifetimes, which correspond to the second component, are listed in **Table 2.1**. Perhaps surprisingly, we observe very little variation in the excited-state lifetimes of the series, which range from ~40-60 ps. The lifetimes of the tetramer solutions are more than an order of magnitude shorter than the monomer solutions, indicating that the excited-state quenching previously observed in homotetramers also occurs in heterotetramers.[58,59] This result, combined with the dramatically reduced fluorescence intensity of the tetramers

compared to the monomers, further corroborates that the quenched fluorescence of the tetramer solutions results from rapid nonradiative decay to the ground state. We assign the nonradiative decay to a nonadiabatic transition from the lowest-energy excited state (S_1S_0) to the ground state (S_0S_0), and note that such quenching has been observed in a number of additional strongly-coupled dye aggregate systems.[58]

Table 2.1.   Excited-State Lifetimes of Cy5 and Cy5.5 Monomer and Tetramer Solutions

Sample	τ (ps)
A_5BCD	1870 $\pm$ 20.0
$ABC_{5.5}D$	920 $\pm$ 10.0
$A_5B_5C_5D_5$	44.2 $\pm$ 0.6
$A_5B_5C_5D_{5.5}$	38.3 $\pm$ 0.5
$A_5B_5C_{5.5}D_{5.5}$	38.7 $\pm$ 0.5
$A_5B_{5.5}C_{5.5}D_{5.5}$	45.5 $\pm$ 0.9
$A_{5.5}B_{5.5}C_{5.5}D_{5.5}$	58.6 $\pm$ 0.5

<u>Purely electronic exciton theory model of electronic structure</u>

The similarities in appearance between the tetramer absorption spectra (**Figure 2.2B**)—which is mirrored in the TA spectra (**Figure 2.3A**) as well as the regular progression both sets of spectra display with increasing Cy5.5 content—suggest that the dyes in each tetramer are packing similarly and experiencing similar excitonic interactions. To better understand the observed progression of the absorption spectra, we use a model based on Kasha's molecular exciton theory to predict the progression.[21–23] We made several assumptions to create a model Hamiltonian. We first assumed that the dyes were located at the four corners of a square with their TDMs aligned parallel to one another and normal to the plane of the square, which prior studies have indicated is approximately representative.[45] We additionally assumed that excitonic interactions between pairs of dyes, described quantitatively by the excitonic hopping parameter, J_{mn}, is independent of

dye type. We were motivated to make this assumption as the excitonic interactions between pairs of dyes is mediated by their TDM, which seemed reasonable given that the TDMs of Cy5 and Cy5.5 are similar.[51,55,56] Finally, we assumed that excitonic interactions between dyes were mediated purely by electronic coupling; that is, vibronic coupling was neglected. The assumption here is reasonable given the considerable amplitude of the dye TDMs, which is associated with a fully allowed electronic transition. These assumptions yield a diagonally symmetric 4 × 4 Hamiltonian matrix. In the Hamiltonian, we assume a single value for the excitonic hopping parameter associated with nearest neighbor dyes, which we label J_N. Likewise, we assume a single value for the excitonic hopping parameter associated with next-nearest neighbor dyes interacting across the diagonal, which we label J_{NN}, and further assume that $J_{NN} = 2^{-3/2} \times J_N$ due to the R^3 dependence of J_{mn} on dye separation. The relationship between J_N and J_{NN} is represented graphically in **Figure 2.4A**. Assuming periodic boundary conditions, the Hamiltonian for such a tetramer is given by:

$$\hat{H} = \sum_{j=0}^{3} \varepsilon_i \, |i\rangle\langle i| + \sum_{j=i\pm1}^{3} J_N \, |j\rangle\langle i| + \sum_{j=i\pm2}^{3} 2^{-3/2} J_N \, |j\rangle\langle i| \qquad \textbf{Eq. 2.1}$$

where ε_i is the transition energy for dye i, which is 1.90 and 1.78 eV for Cy5 and Cy5.5, respectively (see e.g. **Figure 2.2A**).

A

B
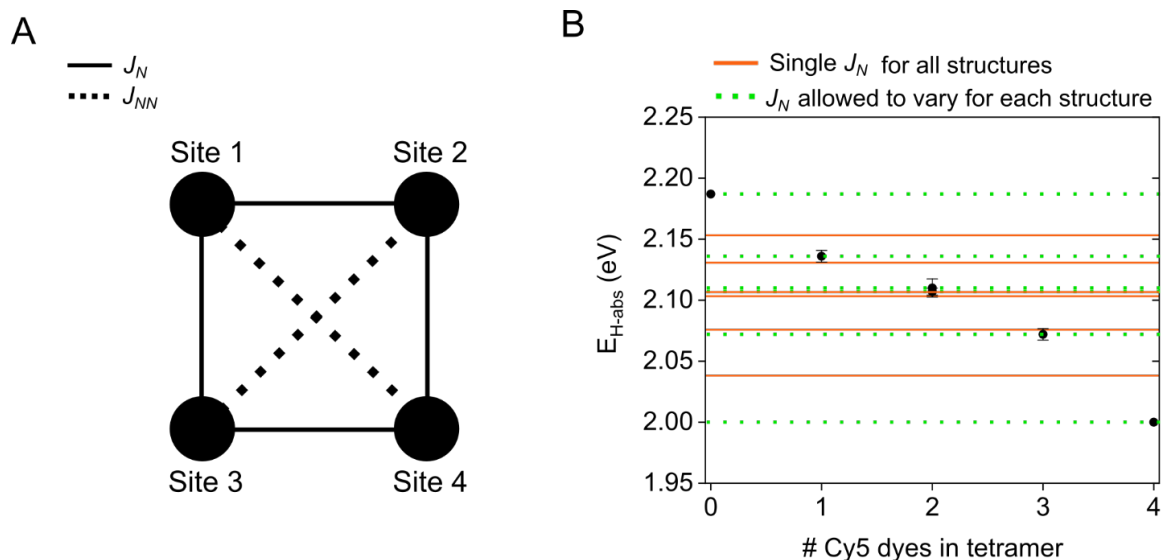
Figure 2.4. **(A) Schematic illustration of the dye configuration used in the Hamiltonian. Black dots represent the TDM centers (pointing into and out of the plane of the page). Lines represent the excitonic hopping parameter between pairs of dyes. (B) Energies of the blue shifted absorption maxima of the DNA Holliday junction-templated tetramer solutions as a function Cy5.5 content (circles), and corresponding best fits of the highest energy eigenvalue (horizontal lines) calculated from exciton theory using a single value for the exciton hopping parameter, J_N, as the only fitting parameter (orange lines), and allowing J_N to vary for each structure (green dotted lines). The error bars represent the variance of the absorption maxima for tetramers of a given composition. Two circles and fit lines are plotted for the tetramers composed of two Cy5 and two Cy5.5 molecules because of the two distinct symmetries associated with placing the like dyes at adjacent corners or across the diagonal of a square. The full set of calculated energy eigenvalues for the global and individual fits are listed in Section S10.**

We proceeded to examine whether the purely electronic model could explain the progression of the transition energies associated with the most intense absorption of the tetramers, shown as black circles in **Figure 2.4B**. We first fit the data globally using a least-squares approach, varying only the excitonic hopping parameter to calculate the energy eigenvalues of the tetramer electronic transitions. We initially assumed no next-nearest neighbor coupling (i.e., $J_{NN} = 0$). We found that the best fit is achieved for a J_N value of 129 meV, which produces an average error of 0.7% between the measured transition

energies and fitted energy eigenvalues. We then performed the global fit assuming next-nearest neighbor coupling is present (i.e., $J_{NN} = 2^{-3/2} \times J_N$). Since the nearest-neighbor and next-nearest neighbor couplings are related by a coefficient, the global fit still uses a single fitting parameter. The best global fit was produced for a J_N value of 108 meV, which produced the equivalent average error as when assuming $J_{NN} = 0$ (**Figure 2.4B**, orange). The global fit shown in **Figure 2.4B** agrees particularly well with the measured highest-energy electronic transitions for the heterotetramers, but under- and over-estimates the transition energies of the Cy5 and Cy5.5 homotetramers, respectively.

We then proceeded to fit the highest-energy transitions for each tetramer type individually. This fit is shown in dotted green in **Figure 2.4B**. While there are no errors associated with these fits, it is useful to compare the calculated J_N and J_{NN} values, which are shown in **Table 2.2**. According to this model, the coupling between adjacent dyes exhibits a maximum value of 123 meV for the Cy5 homotetramer, decreases to a value of ~110 meV for the heterotetramers and is independent of composition, and further decreases to a value of 92 meV for the Cy5.5 homotetramer. A possible explanation for this trend may be due to the extra bulkiness (i.e., aryl groups) associated with Cy5.5 in the heterotetramers and Cy5.5 homotetramer preventing the dyes from packing as close. The ability of this model to fit the highest-energy transitions for all tetramers with a single fitting parameter suggests that the assumptions of the model are physically reasonable. For example, the good match of the exciton theory model with the data suggests that excitonic interactions between dyes are largely mediated by electronic rather than vibronic coupling.

Table 2.2.   Exciton Hopping Parameters that Produced the Best Fit of the Highest Energy Transition Energies of the Homo- and Hetero-Tetramers via the Purely Electronic Exciton Theory Model.

Construct	J_N (meV)	J_{NN} (meV)
$A_5B_5C_5D_5$	123	43
$A_5B_5C_5D_{5.5}$	111	39
$A_5B_5C_{5.5}D_{5.5}$	110	39
$A_5B_{5.5}C_5D_{5.5}$	110	39
$A_5B_{5.5}C_{5.5}D_{5.5}$	105	37
$A_{5.5}B_{5.5}C_{5.5}D_{5.5}$	92	33

To gain additional insight into the results of the purely electronic exciton theory model, we simulated the optical properties of the tetramers using a deeper level of theory. Specifically, we simulated the steady-state absorption and CD spectra via a model based on KRM theory.[61] In the KRM modeling approach, the best fit to the steady-state absorption and CD spectra is found by simulating a range of dye orientations within the aggregate.[45,57] The KRM modeling approach calculates J_{mn} between every pair of dyes within the aggregate, models the TDMs as extended dipoles, and incorporates vibronic coupling to a single mode, making a comparison of the results of the KRM modeling an excellent test of the validity of the assumptions inherent to the exciton theory model. In the KRM modeling approach employed here, the centers of the extended dipoles were constrained to a square configuration, while the zenith and azimuthal angles were allowed to vary. The procedure was iterated to determine the optimal dye separation (i.e., the edge length of the square configuration). **Section S11** overlays the steady-state absorption and CD spectra of the Cy5 and Cy5.5 homotetramers with fits from the KRM modeling. **Table 2.3** displays the associated J_N and J_{NN} values.

Table 2.3   Excitonic Hopping Parameters of the Homotetramers Derived from KRM Modeling

Construct	J_N (meV)	J_{NN} (meV)
$A_5B_5C_5D_5$	106	69
$A_{5.5}B_{5.5}C_{5.5}D_{5.5}$	70	20

We then compared the results of the KRM modeling to those of the purely electronic exciton model. For the Cy5 homotetramer, we find that the J_N values in **Table 2.2** (purely electronic model) are consistent with the corresponding values in **Table 2.3** (KRM modeling approach), indicating good agreement between the two approaches. Interestingly, the J_N value derived via the purely electronic model is slightly larger (~16%) than the value derived via the KRM modeling approach, while J_{NN} is appreciably smaller (~38%). We explain the discrepancy in J_{NN} values by considering that the excitonic coupling experienced between the extended dipoles used in KRM exhibits more gradual drop off at close range compared to the purely electronic model, which treats the TDMs as point dipoles. For the Cy5.5 homotetramer, J_N and J_{NN} values derived for the purely electronic model are ~31 and ~65% larger than the values derived by the KRM model, respectively.

Next, we compared the dye packing configurations of the two models. While the symmetry of the Hamiltonian matrix used in the purely electronic model implies the dyes are oriented perfectly parallel, the results of the KRM modelling indicate that the TDM vectors deviate somewhat from this ideal configuration. This deviation captures the circular dichroism exhibited by the tetramers. For the Cy5 homotetramer, this deviation is relatively small, and the average deviation from parallel for each pair of dyes is ~17 degrees (**Section S11**). For the Cy5.5 homotetramer, however, the TDM vectors deviated more appreciably, with an average deviation from parallel of ~51 degrees. The greater deviation from parallel

calculated for the Cy5.5 homotetramer is consistent with its more complicated and intense CD response compared to the Cy5 homotetramer, which may also account for the greater deviation from the J_{NN} predicted by the purely electronic model. Based on the agreement between the results of the KRM and the purely electronic models, we conclude that the dyes in the homotetramers pack approximately in the configuration of a square and that the assumptions inherent to the purely electronic model are sufficiently valid to enable basic predictions of the electronic structure of the Cy5 and Cy5.5 homo- and hetero-tetramers (for additional details and discussion, see e.g. **Section S12**).

Idealized J-aggregate FRET relay.

Our finding that the electronic structure of Cy5 and Cy5.5 homo- and hetero-aggregate tetramers can be tuned by changing the aggregate composition, and that the resulting spectral variations are well described by a purely electronic exciton theory model, has interesting implications, particularly when extended to J-aggregates. The properties of J-aggregates, specifically their intense and narrow absorption bands and increased radiative rates relative to monomers,[18,19,62] are of interest for applications that involve EET. If the cyanine dyes Cy5 and Cy5.5 could be assembled in the form of J-aggregates of varying composition, the resultant material could potentially find application in organic optoelectronics, light harvesting, and nanoscale computing, as discussed in the Introduction.

To illustrate the potential impact of our results on EET, we next discuss how a FRET relay comprised of tunable J-aggregate heterotetramers might function. This idealized energy relay (**Figure 2.5A**) begins with a Cy5.5 monomer, includes three bridging Cy5 and Cy5.5 homo- and hetero-tetramers, and ends with a Cy5-Cy5.5

heterotetramer. Using the purely electronic exciton theory model as it would apply to the J-aggregate geometry, we calculated the transition energies using the Hamiltonian:

$$\hat{H} = \sum_{n=0}^{3} \varepsilon_n \, |n\rangle\langle n| + \sum_{n=m\pm1}^{3} J_N \, |n\rangle\langle m| \qquad \textbf{Eq. 2.2}$$

where we assumed a J_n value of 120 meV because it is comparable to the values derived for the H-aggregate homo- and hetero-tetramers. The calculated transition energies, in this case corresponding to the fully-allowed lowest-energy electronic transition, are shown above the corresponding J-aggregate homo- and hetero-tetramers in **Figure 2.5**. The tetramers are organized to spatially direct the EET; that is, EET proceeds downhill in energy from left-to-right in the diagram. To estimate the rates and efficiencies of EET in the FRET relay, we next simulated the optical spectra of the J-aggregate homo- and hetero-tetramers in order to extract the radiative rates of each tetramer and the absorption and emission spectral overlap integrals, which determine the EET rates.[17] Implicit in the calculated radiative rates is the assumption that the TDMs associated with each dye in the tetramer interact cooperatively, i.e., the tetramers exhibit superradiance,[62,63] which is a potential advantage of using J-aggregates for EET. Additionally, the tunability of heteroaggregates can potentially be used to optimize spectral overlap integrals. For specified end-to-end EET quantum efficiencies, Φ_{EET}, we calculated EET rates and maximum separations for the different donor-acceptor pairs (**Section S13**).
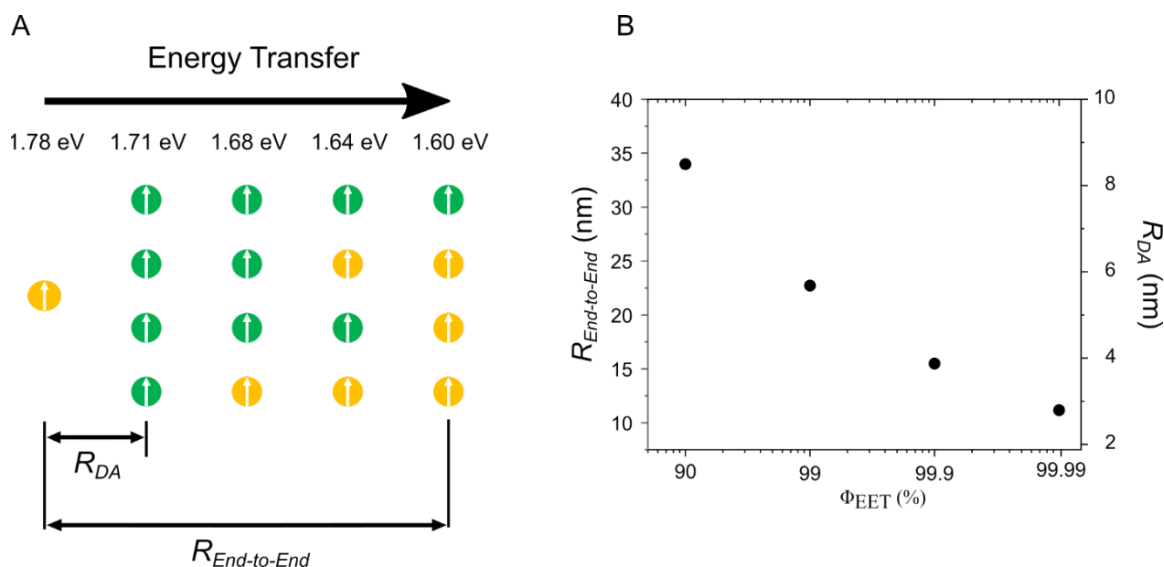
Figure 2.5. **(A) Schematic diagram of the idealized J-aggregate FRET relay. Cy5 and Cy5.5 dyes are shown in green and yellow, respectively. The relay begins with Cy5.5 monomer, includes three intermediate homo- and hetero-tetramer J-aggregates, and ends with a hetero-tetramer J-aggregate. The energy value for Cy5.5 corresponds to 1.78 eV; shown above each homo- and hetero-tetramer is the calculated energy corresponding to the lowest energy electronic transition. Transition dipole moments of the constituent dyes are indicated by white arrows. Double headed arrows labeled R_{DA} and $R_{End-to-End}$ indicate donor-acceptor and end-to-end distances, respectively. (B) Calculated R_{DA} and $R_{End-to-End}$ as a function of electronic energy transfer quantum efficiency (i.e., Φ_{EET}).**

Figure 2.5B shows the relationship between the calculated maximum end-to-end distances and quantum efficiencies for the FRET relay. The results of these calculations have relevance to a number of applications based on EET. For example, the overall device efficiency of organic solar cells is often limited by the exciton diffusion length (typically ~10 nm), which is generally an order of magnitude smaller than the absorption length (i.e., ~100 nm).[64–66] Long-range spatially directed energy transfer up to 34 nm with an efficiency of 90% may benefit organic solar cells by facilitating spatially directed EET toward an electron donor:acceptor interface.[67] **Figure 2.5B** shows that a larger efficiency of 99% is achieved for a smaller distance of ~23 nm, which may benefit light harvesting systems

where it has been suggested that large spatial separation of antenna complexes and reaction centers (i.e., greater than 10 nm) may prevent excitation quenching via chemical oxidation.[68] Even higher EET quantum efficiencies are possible for smaller end-to-end distances (although we acknowledge that deviations from the point-dipole approximation in this regime may cause quantitative disagreement[13,14,69]—see e.g. **Section S14**). Higher EET efficiencies may benefit applications in nanoscale computing,[4] which are envisioned to include optical inputs, active elements, and optical outputs where EET mediates the transfer of excitons. For example, 99.9 and 99.99% quantum efficiencies, which result in end-to-end distances >10 nm, correspond to error rates of 1 in 1,000 and 1 in 10,000, respectively, where the exciton does not transfer to the end of the relay. Such error rates are clearly within the 1% error permitted by computational error correction procedures.[70–73] The potential impact of such an idealized FRET relay on the applications highlighted above sheds promising light on the future utility of tunable heteroaggregates.

2.4 Conclusion

In conclusion, we showed that the electronic structure of tetramer aggregates of two chemically distinct cyanine dyes is progressively tunable by modifying the aggregate composition. Specifically, we used DNA Holliday junctions to template homo- and hetero-tetramer aggregates of Cy5 and Cy5.5. The optical properties, including absorption and CD, exhibit a progressive trend with respect to Cy5.5 content; the overall blueshift of the absorption spectra was consistent with similar H-aggregate packing across the series. The aggregates in this form exhibited quenched fluorescence emission and short excited-state lifetimes. We applied an exciton theory model to describe the progression of the electronic structure, which had a number of assumptions including purely electronic interactions. The

agreement between the experimental results, the purely electronic exciton theory model, and more advanced modeling based on KRM theory validated these assumptions. We proceeded to use the purely electronic exciton theory model to estimate end-to-end distances and overall EET quantum efficiencies for an idealized J-aggregated-based homo- and hetero-tetramer relay. If such FRET relays can be realized, they would have profound implications in a diverse range of fields including light harvesting, organic optoelectronics, and nanoscale computing.

2.5 Acknowledgments

2.6 References

(1) Mirkovic, T.; Ostroumov, E. E.; Anna, J. M.; Grondelle, R. Van; Scholes, G. D. Light Absorption and Energy Transfer in the Antenna Complexes of Photosynthetic Organisms. *Chem. Rev.* **2017**, *117* (2), 249–293. https://doi.org/10.1021/acs.chemrev.6b00002.

(2) Brixner, T.; Hildner, R.; Köhler, J.; Lambert, C.; Würthner, F. Exciton Transport in Molecular Aggregates – From Natural Antennas to Synthetic Chromophore Systems. *Adv. Energy Mater.* **2017**, *7* (16), 1–33. https://doi.org/10.1002/aenm.201700236.

(3) Ostroverkhova, O. Organic Optoelectronic Materials: Mechanisms and Applications. *Chem. Rev.* **2016**, *116* (22), 13279–13412. https://doi.org/10.1021/acs.chemrev.6b00127.

(4) Yurke, B.; Kuang, W. Passive Linear Nanoscale Optical and Molecular Electronics Device Synthesis from Nanoparticles. *Phys. Rev. A* **2010**, *81* (3), 033814-1–9. https://doi.org/10.1103/PhysRevA.81.033814.

(5) Graugnard, E.; Kellis, D. L.; Bui, H.; Barnes, S.; Kuang, W.; Lee, J.; Hughes, W. L.; Knowlton, W. B.; Yurke, B. DNA-Controlled Excitonic Switches. *Nano Lett.* **2012**, *12* (4), 2117–2122. https://doi.org/10.1021/nl3004336.

(6) Laboda, C.; Duschl, H.; Dwyer, C. L. DNA-Enabled Integrated Molecular Systems for Computation and Sensing. *Acc. Chem. Res.* **2014**, *47* (6), 1816–1824. https://doi.org/10.1021/ar500054u.

(7) Cannon, B. L.; Kellis, D. L.; Davis, P. H.; Lee, J.; Kuang, W.; Hughes, W. L.; Graugnard, E.; Yurke, B.; Knowlton, W. B. Excitonic AND Logic Gates on DNA Brick Nanobreadboards. *ACS Photonics* **2015**, *2* (3), 398–404. https://doi.org/10.1021/ph500444d.

(8) Sawaya, N. P. D.; Rappoport, D.; Tabor, D. P.; Aspuru-Guzik, A. Excitonics: A Set of Gates for Molecular Exciton Processing and Signaling. *ACS Nano* **2018**, *12* (7), 6410–6420. https://doi.org/10.1021/acsnano.8b00584.

(9) Kellis, D. L.; Sarter, C.; Cannon, B. L.; Davis, P. H.; Graugnard, E.; Lee, J.; Pensack, R. D.; Kolmar, T.; Jäschke, A.; Yurke, B.; et al. An All-Optical Excitonic Switch Operated in the Liquid and Solid Phases. *ACS Nano* **2019**, *13* (3), 2986–2994. https://doi.org/10.1021/acsnano.8b07504.

(10) Castellanos, M. A.; Dodin, A.; Willard, A. P. On the Design of Molecular Excitonic Circuits for Quantum Computing: The Universal Quantum Gates. *Phys. Chem. Chem. Phys.* **2020**, *22* (5), 3048–3057. https://doi.org/10.1039/c9cp05625d.

(11) Förster, T. Energiewanderung Und Fluoreszenz. *Naturwissenschaften* **1946**, *33*, 166–175.

(12) Förster, T. Energy Migration and Fluorescence. *J. Biomed. Opt.* **2012**, *17* (1), 011002. https://doi.org/10.1117/1.jbo.17.1.011002.

(13) Muñoz-Losa, A.; Curutchet, C.; Krueger, B. P.; Hartsell, L. R.; Mennucci, B. Fretting about FRET : Failure of the Ideal Dipole Approximation. *Biophys. J.* **2009**, *96* (12), 4779–4788. https://doi.org/10.1016/j.bpj.2009.03.052.

(14) Scholes, G. D. Designing Light-Harvesting Antenna Systems Based on Superradiant Molecular Aggregates. *Chem. Phys.* **2002**, *275* (1–3), 373–386. https://doi.org/10.1016/S0301-0104(01)00533-X.

(15) Petkov, B. K.; Gellen, T. A.; Farfan, C. A.; Carbery, W. P.; Hetzler, B. E.; Trauner, D.; Li, X.; Glover, W. J.; Ulness, D. J.; Turner, D. B. Two-Dimensional Electronic Spectroscopy Reveals the Spectral Dynamics of Förster Resonance Energy Transfer. *Chem* **2019**, *5*, 2111–2125. https://doi.org/10.1016/j.chempr.2019.05.005.

(16) Scholes, G. D. Long-Range Resonance Energy Transfer in Molecular Systems. *Annu. Rev. Phys. Chem.* **2003**, *54* (18), 57–87. https://doi.org/10.1146/annurev.physchem.54.011002.103746.

(17) Clegg, R. M. Fluorescence Resonance Energy Transfer and Nucleic Acids. *Methods Enzymol.* **1992**, *211*, 353–388.

(18) Würthner, F.; Kaiser, T. E.; Saha-Möller, C. R. J-Aggregates: From Serendipitous Discovery to Supramolecular Engineering of Functional Dye Materials. *Angew. Chemie - Int. Ed.* **2011**, *50* (15), 3376–3410. https://doi.org/10.1002/anie.201002307.

(19) Julia.L. Bricks, Yuri.L. Slominskii, Ihor.D. Panas, A. P. D. Fluorescent J-Aggregates of Cyanine Dyes: Basic Research and Applications Review. *Methods Appl. Fluoresc.* **2018**, *6*. https://doi/https://doi.org/10.1088/1478-3975/aa9768.

(20) Mirkovic, T.; Ostroumov, E. E.; Anna, J. M.; Grondelle, R. Van; Govindjee; Scholes, G. D. Light Absorption and Energy Transfer in the Antenna Complexes of Photosynthetic Organisms. *Chem. Rev.* **2017**, *117* (2), 249–293. https://doi.org/10.1021/acs.chemrev.6b00002.

(21) Kasha, M. Energy Transfer Mechanisms and the Molecular Exciton Model for Molecular Aggregates. *Radiat. Res.* **1963**, *20* (1), 55–70.

(22) Kasha, M.; Rawls, H. R.; Ashraf El-Bayoumi, M. The Exciton Model in Molecular Spectroscopy. *Pure Appl. Chem.* **1965**, *11* (3–4), 371–392. https://doi.org/10.1351/pac196511030371.

(23) Mcrae, E. G.; Kasha, M. Enhancement of Phosphorescence Ability upon Aggregation of Dye Molecules. *J. Chem. Phys.* **1958**, *28* (721). https://doi.org/10.1063/1.1744225.

(24) Turro, N. J.; Scaiano, J. C.; Ramamurthy, V. *Modern Molecular Photochemistry of Organic Molecules*; University Science Books: Sausalito, Calif, 2010. https://doi.org/10.1111/j.1751-1097.2012.01178.x.

(25) Kashida, H.; Asanuma, H. Threoninol as a Scaffold of Dyes (Threoninol-Nucleotide) and Their Stable Interstrand Clustering in Duplexes †. *Org. Biomol. Chem* **2008**, *6*, 2892–2899. https://doi.org/10.1039/b806406g.

(26) Kirchner, E.; Bialas, D.; Fennel, F. Defined Merocyanine Dye Stacks from a Dimer up to an Octamer by Spacer-Encoded Self-Assembly Approach. *J. Am. Chem. Soc.* **2019**, *141*, 7248–7438. https://doi.org/10.1021/jacs.9b01835.

(27) Ahn, T. S.; Müller, A. M.; Al-Kaysi, R. O.; Spano, F. C.; Norton, J. E.; Beljonne, D.; Bŕdas, J. L.; Bardeen, C. J. Experimental and Theoretical Study of Temperature Dependent Exciton Delocalization and Relaxation in Anthracene Thin Films. *J. Chem. Phys.* **2008**, *128* (5), 1–11. https://doi.org/10.1063/1.2822310.

(28) Seeman, N. C.; Kallenbach, N. R. Design of Immobile Nucleic Acid Junctions. *Biophys. J.* **1983**, *44* (2), 201–209. https://doi.org/10.1016/S0006-3495(83)84292-1.

(29) Brown, C. W.; Buckhout-White, S.; Sebastián, S.; Díaz, A.; Melinger, J. S.; Ancona, M. G.; Goldman, E. R.; Medintz, I. L. Evaluating Dye-Labeled DNA Dendrimers for Potential Applications in Molecular Biosensing. *ACS Sensors* **2017**, *2*, 401–410. https://doi.org/10.1021/acssensors.6b00778.

(30) Olshansky, J. H.; Zhang, J.; Krzyaniak, M. D.; Lorenzo, E. R.; Wasielewski, M. R. Selectively Addressable Photogenerated Spin Qubit Pairs in DNA Hairpins. *J. Am. Chem. Soc.* **2020**, *142* (7), 3346–3350. https://doi.org/10.1021/jacs.9b13398.

(31) Depew, D. E.; Wang, J. C. Conformational Fluctuations of DNA Helix. *Proc. Natl. Acad. Sci. U. S. A.* **1975**, *72* (11), 4275–4279.

(32) Rothemund, P. W. K. Folding DNA to Create Nanoscale Shapes and Patterns. *Nature* **2006**, *440* (7082), 297–302. https://doi.org/10.1038/nature04586.

(33) Bösch, C. D.; Jevric, J.; Bürki, N.; Probst, M.; Langenegger, S. M.; Häner, R. Supramolecular Assembly of DNA-Phenanthrene Conjugates into Vesicles with Light-Harvesting Properties. *Bioconjug. Chem.* **2018**, *29* (5), 1505–1509. https://doi.org/10.1021/acs.bioconjchem.8b00263.

(34) Rothenbühler, S.; Iacovache, I.; Langenegger, S. M.; Zuber, B.; Häner, R. Complex DNA Architectonics - Self-Assembly of Amphiphilic Oligonucleotides into Ribbons, Vesicles, and Asterosomes. *Bioconjug. Chem.* **2022**. https://doi.org/10.1021/acs.bioconjchem.2c00077.

(35) Nicoli, F.; Roos, M. K.; Hemmig, E. A.; Di Antonio, M.; De Vivie-Riedle, R.; Liedl, T. Proximity-Induced H-Aggregation of Cyanine Dyes on DNA-Duplexes. *J. Phys. Chem. A* **2016**, *120* (50), 9941–9947. https://doi.org/10.1021/acs.jpca.6b10939.

(36) Cunningham, P. D.; Kim, Y. C.; Díaz, S. A.; Buckhout-White, S.; Mathur, D.; Medintz, I. L.; Melinger, J. S. Optical Properties of Vibronically Coupled Cy3 Dimers on DNA Scaffolds. *J. Phys. Chem. B* **2018**, *122* (19), 5020–5029. https://doi.org/10.1021/acs.jpcb.8b02134.

(37) Heussman, D.; Kittell, J.; Kringle, L.; Tamimi, A.; von Hippel, P. H.; Marcus, A. H. Measuring Local Conformations and Conformational Disorder of (Cy3)2 Dimer Labeled DNA Fork Junctions Using Absorbance, Circular Dichroism and Two-Dimensional Fluorescence Spectroscopy. *Faraday Discuss.* **2019**, No. DOI: 10.1039/C8FD00245B. https://doi.org/10.1039/C8FD00245B.

(38) Cunningham, P. D.; Díaz, S. A.; Yurke, B.; Medintz, I. L.; Melinger, J. S. Delocalized Two-Exciton States in DNA Scaffolded Cyanine Dimers. *J. Phys. Chem. B* **2020**, *124* (37), 8042–8049. https://doi.org/10.1021/acs.jpcb.0c06732.

(39) Mass, O. A.; Wilson, C. K.; Roy, S. K.; Barclay, M. S.; Patten, L. K.; Terpetschnig, E. A.; Lee, J.; Pensack, R. D.; Yurke, B.; Knowlton, W. B. Exciton Delocalization in Indolenine Squaraine Aggregates Templated by DNA Holliday Junction Scaffolds. *J. Phys. Chem. B* **2020**, *124* (43), 9636–9647. https://doi.org/10.1021/acs.jpcb.0c06480.

(40) Hart, S. M.; Chen, W. J.; Banal, J. L.; Bricker, W. P.; Dodin, A.; Markova, L.; Vyborna, Y.; Willard, A. P.; Häner, R.; Bathe, M.; et al. Engineering Couplings for Exciton Transport Using Synthetic DNA Scaffolds. *Chem* **2021**, *7*, 752–773. https://doi.org/10.1016/j.chempr.2020.12.020.

(41) Mass, O. A.; Wilson, C. K.; Barcenas, G.; Terpetschnig, E. A.; Obukhova, O. M.; Kolosova, O. S.; Tatarets, A. L.; Li, L.; Yurke, B.; Knowlton, W. B.; et al.

Influence of Hydrophobicity on Excitonic Coupling in DNA-Templated Indolenine Squaraine Dye Aggregates. *J. Phys. Chem. C* **2022**, *126* (7), 3475–3488. https://doi.org/10.1021/acs.jpcc.1c08981.

(42) Hart, S. M.; Wang, X.; Guo, J.; Bathe, M.; Schlau-cohen, G. S. Tuning Optical Absorption and Emission Using Strongly Coupled Dimers in Programmable DNA Scaffolds. *J. Phys. Chem. Lett.* **2022**, *13*, 1863–1871. https://doi.org/10.1021/acs.jpclett.1c03848.

(43) Chowdhury, A. U.; Díaz, S. A.; Huff, J. S.; Barclay, M. S.; Chiriboga, M.; Ellis, G. A.; Mathur, D.; Patten, L. K.; Sup, A.; Hallstrom, N.; et al. Tuning between Quenching and Energy Transfer in DNA-Templated Heterodimer Aggregates. *J. Phys. Chem. Lett.* **2022**, *13*, 2782–2791. https://doi.org/10.1021/acs.jpclett.2c00017.

(44) Barclay, M. S.; Wilson, C. K.; Roy, S. K.; Mass, O. A.; Obukhova, O. M.; Svoiakov, R. P.; Tatarets, A. L.; Chowdhury, A. U.; Huff, J. S.; Turner, D. B.; et al. Oblique Packing and Tunable Excitonic Coupling in DNA-Templated Squaraine Rotaxane Dimer Aggregates. *ChemPhotoChem* **2022**, No. e202200039. https://doi.org/10.1002/cptc.202200039.

(45) Cannon, B. L.; Kellis, D. L.; Patten, L. K.; Davis, P. H.; Lee, J.; Graugnard, E.; Yurke, B.; Knowlton, W. B. Coherent Exciton Delocalization in a Two-State DNA-Templated Dye Aggregate System. *J. Phys. Chem. A* **2017**, *121* (37), 6905–6916. https://doi.org/10.1021/acs.jpca.7b04344.

(46) Markova, L. I.; Malinovskii, V. L.; Patsenker, L. D.; Häner, R. J- vs. H-Type Assembly: Pentamethine Cyanine (Cy5) as a near-IR Chiroptical Reporter. *Chem. Commun.* **2013**, *49* (46), 5298–5300. https://doi.org/10.1039/c3cc42103a.

(47) Heussman, D.; Kittell, J.; Von Hippel, P. H.; Marcus, A. H. Temperature-Dependent Local Conformations and Conformational Distributions of Cyanine Dimer Labeled Single-Stranded-Double-Stranded DNA Junctions by 2D Fluorescence Spectroscopy. *J. Chem. Phys.* **2022**, *156* (045101). https://doi.org/10.1063/5.0076261.

(48) Fujii, T.; Kashida, H.; Asanuma, H. Analysis of Coherent Heteroclustering of Different Dyes by Use of Threoninol Nucleotides for Comparison with the Molecular Exciton Theory. *Chem. - A Eur. J.* **2009**, *15*, 10092–10102. https://doi.org/10.1002/chem.200900962.

(49) Asanuma, H.; Fujii, T.; Kato, T.; Kashida, H. Coherent Interactions of Dyes Assembled on DNA. *J. Photochem. Photobiol. C Photochem. Rev.* **2012**, *13* (2), 124–135. https://doi.org/10.1016/j.jphotochemrev.2012.04.002.

(50) Asanuma, H.; Murayama, K.; Kamiya, Y.; Kashida, H. The DNA Duplex as an Aqueous One-Dimensional Soft Crystal Scaffold for Photochemistry. *Bull. Chem. Soc. Jpn.* **2018**, *91* (12), 1739–1748. https://doi.org/10.1246/bcsj.20180278.

(51) Biaggne, A.; Spear, L.; Ketteridge, M.; Kim, Y. C.; Melinger, J. S.; Knowlton, W. B.; Yurke, B.; Li, L. Data-Driven and Multiscale Modeling of DNA-Templated Dye Aggregates. *Molecules* **2022**, *27*, 3456.

(52) Meares, A.; Susumu, K.; Mathur, D.; Lee, S. H.; Mass, O. A.; Lee, J.; Pensack, R. D.; Yurke, B.; Knowlton, W. B.; Melinger, J. S.; et al. Synthesis of Substituted Cy5 Phosphoramidite Derivatives and Their Incorporation into Oligonucleotides Using Automated DNA Synthesis. *ACS Omega* **2022**, *7* (13), 11002–11016.

https://doi.org/10.1021/acsomega.1c06921.

(53) Mustroph, H.; Reiner, K.; Mistol, J.; Ernst, S.; Keil, D.; Hennig, L. Relationship between the Molecular Structure of Cyanine Dyes and the Vibrational Fine Structure of Their Electronic Absorption Spectra. *ChemPhysChem* **2009**, *10* (5), 835–840. https://doi.org/10.1002/cphc.200800755.

(54) Bishop, M. M.; Roscioli, J. D.; Ghosh, S.; Mueller, J. J.; Shepherd, N. C.; Beck, W. F. Vibrationally Coherent Preparation of the Transition State for Photoisomerization of the Cyanine Dye Cy5 in Water. *J. Phys. Chem. B* **2015**, *119* (23), 6905–6915. https://doi.org/10.1021/acs.jpcb.5b02391.

(55) Dominik Spiegel, J.; Fulle, S.; Kleinschmidt, M.; Gohlke, H.; Marian, C. M. Failure of the IDA in FRET Systems at Close Inter-Dye Distances Is Moderated by Frequent Low K2 Values. *J. Phys. Chem. B* **2016**, *120* (34), 8845–8862. https://doi.org/10.1021/acs.jpcb.6b05754.

(56) Biaggne, A.; Knowlton, W. B.; Yurke, B.; Lee, J.; Li, L. Substituent Effects on the Solubility and Electronic Properties of the Cyanine Dye Cy5: Density Functional and Time-Dependent Density Functional Theory Calculations. *Molecules* **2021**, *26* (3). https://doi.org/10.3390/molecules26030524.

(57) Cannon, B. L.; Patten, L. K.; Kellis, D. L.; Davis, P. H.; Lee, J.; Graugnard, E.; Yurke, B.; Knowlton, W. B. Large Davydov Splitting and Strong Fluorescence Suppression: An Investigation of Exciton Delocalization in DNA-Templated Holliday Junction Dye Aggregates. *J. Phys. Chem. A* **2018**, *122* (8), 2086–2095. https://doi.org/10.1021/acs.jpca.7b12668.

(58) Huff, J. S.; Davis, P. H.; Christy, A.; Kellis, D. L.; Kandadai, N.; Toa, Z. S. D.; Scholes, G. D.; Yurke, B.; Knowlton, W. B.; Pensack, R. D. DNA-Templated Aggregates of Strongly Coupled Cyanine Dyes: Nonradiative Decay Governs Exciton Lifetimes. *J. Phys. Chem. Lett.* **2019**, *10* (10), 2386–2392. https://doi.org/10.1021/acs.jpclett.9b00404.

(59) Huff, J. S.; Turner, D. B.; Mass, O. A.; Patten, L. K.; Wilson, C. K.; Roy, S. K.; Barclay, M. S.; Yurke, B.; Knowlton, W. B.; Davis, P. H.; et al. Excited-State Lifetimes of DNA-Templated Cyanine Dimer, Trimer, and Tetramer Aggregates: The Role of Exciton Delocalization, Dye Separation, and DNA Heterogeneity. *J. Phys. Chem. B* **2021**, *125* (36), 10240–10259. https://doi.org/10.1021/acs.jpcb.1c04517.

(60) Von Hippel, P. H.; Johnson, N. P.; Marcus, A. H. Fifty Years of DNA "Breathing": Reflections on Old and New Approaches. *Biopolymers* **2013**, *99* (12), 923–954. https://doi.org/10.1002/bip.22347.

(61) Kühn, O.; Renger, T.; May, V. Theory of Exciton-Vibrational Dynamics in Molecular Dimers. *Chem. Phys.* **1996**, *204* (1), 99–114. https://doi.org/10.1016/0301-0104(95)00448-3.

(62) Spano, F. C.; Kuklinski, J. R.; Mukamel, S. Cooperative Radiative Dynamics in Molecular Aggregates. *J. Chem. Phys.* **1991**, *94* (11), 7534–7544. https://doi.org/10.1063/1.2822310.

(63) Dicke, R. H. Coherence in Spontaneous Radiation Process. *Phys. Rev.* **1954**, *93* (1), 99–110. https://doi.org/10.1038/nphoton.2015.54.

(64) Bredas, J. L. Molecular Understanding of Organic Solar Cells: The Challenges. *Acc. Chem. Res.* **2009**, *42* (11), 1691–1699. https://doi.org/10.1063/1.4794709.

(65)   Clarke, T. M.; Durrant, J. R. Charge Photogeneration in Organic Solar Cells. *Chem. Rev.* **2010**, *110* (11), 6736–6767. https://doi.org/10.1021/cr900271s.

(66)   Ostroverkhova, O. Organic Optoelectronic Materials: Mechanisms and Applications. *Chem. Rev.* **2016**, *116* (22), 13279–13412.

(67)   Scully, S. R.; Armstrong, P. B.; Edder, C.; Fréchet, J. M. J.; McGehee, M. D. Long-Range Resonant Energy Transfer for Enhanced Exciton Harvesting for Organic Solar Cells. *Adv. Mater.* **2007**, *19* (19), 2961–2966. https://doi.org/10.1002/adma.200700917.

(68)   Sundström, V.; Pullerits, T.; Van Grondelle, R. Photosynthetic Light-Harvesting: Reconciling Dynamics and Structure of Purple Bacterial LH2 Reveals Function of Photosynthetic Unit. *J. Phys. Chem. B* **1999**, *103* (13), 2327–2346. https://doi.org/10.1021/jp983722+.

(69)   Scholes, G. D.; Mirkovic, T.; Turner, D. B.; Fassioli, F.; Buchleitner, A. Solar Light Harvesting by Energy Transfer: From Ecology to Coherence. *Energy Environ. Sci.* **2012**, *5* (11), 9374–9393. https://doi.org/10.1039/c2ee23013e.

(70)   Fowler, A. G.; Whiteside, A. C.; Hollenberg, L. C. L. Towards Practical Classical Processing for the Surface Code. *Phys. Rev. Lett.* **2012**, *108*, 180501. https://doi.org/10.1103/PhysRevLett.108.180501.

(71)   Fowler, A. G.; Mariantoni, M.; Martinis, J. M.; Cleland, A. N. Surface Codes: Towards Practical Large-Scale Quantum Computation. *Phys. Rev. A - At. Mol. Opt. Phys.* **2012**, *86* (3). https://doi.org/10.1103/PhysRevA.86.032324.

(72)   Wang, D. S.; Fowler, A. G.; Hollenberg, L. C. L. Surface Code Quantum Computing with Error Rates over 1%. *Phys. Rev. A - At. Mol. Opt. Phys.* **2011**, *83*, 020302. https://doi.org/10.1103/PhysRevA.83.020302.

(73)   Stephens, A. M. Fault-Tolerant Thresholds for Quantum Error Correction with the Surface Code. *Phys. Rev. A - At. Mol. Opt. Phys.* **2014**, *89* (2), 1–9. https://doi.org/10.1103/PhysRevA.89.022321.

CHAPTER THREE: DNA-TEMPLATED AGGREGATES OF STRONGLY COUPLED

CYANINE DYES: NONRADIATIVE DECAY GOVERNS EXCITON LIFETIMES

This chapter is published by the American Chemical Society in *The Journal of Physical Chemistry Letters* and should be referenced appropriately

Reference:

Huff, J. S.; Davis, P. H.; Christy, A.; Kellis, D. L.; Kandadai, N.; Toa, Z. S. D.; Scholes, G. D.; Yurke, B.; Knowlton, W. B.; Pensack, R. D. DNA-Templated Aggregates of Strongly Coupled Cyanine Dyes: Nonradiative Decay Governs Exciton Lifetimes. *J. Phys. Chem. Lett.* **2019**, *10*, 2386–2392,

*This chapter includes modifications from the originally published version.

3.1 Abstract

Molecular excitons are used in a variety of applications including light harvesting, optoelectronics, and nanoscale computing. Controlled aggregation via covalent attachment of dyes to DNA templates is a promising aggregate assembly technique that enables the design of extended dye networks. However, there are few studies of exciton dynamics in DNA-templated dye aggregates. We report time-resolved excited-state dynamics measurements of two cyanine-based dye aggregates, a J-like dimer and an H-like tetramer, formed through DNA-templating of covalently attached dyes. Time-resolved fluorescence and transient absorption indicate that nonradiative decay, in the form of internal conversion, dominates the aggregate ground state recovery dynamics, with singlet exciton lifetimes on the order of tens of picoseconds for the aggregates versus nanoseconds for the monomer. These results highlight the importance of circumventing nonradiative decay pathways in the future design of DNA-templated dye aggregates.

3.2 Introduction

Excitons in molecular (dye) aggregates have sparked intense interest due to their potential applications in light harvesting (including natural,[1] artificial,[2,3] and biomimetic[4–6]), organic optoelectronics,[2,3] and more recently nanoscale computing.[7–11] Dye aggregation was first discovered in the 1930's when Jelley and Scheibe observed significant shifts in absorption spectra of concentrated cyanine dye solutions.[12–14] Since their discovery, considerable effort has been invested in developing an improved understanding of the structure of dye aggregates and nature of the attendant spectral shifts. Importantly, when interchromophore separations are similar to or less than the length of individual chromophores, where the term chromophore is defined as the light-absorbing portion of

the dye molecule, electronic interactions result in splitting of the excited state energy levels and coherent delocalization of excitons. The magnitude of the energy level splitting (known as the Davydov splitting)[15] is highly sensitive to the interchromophore separation, while the relative orientation of the chromophore transition dipoles determines the selection rules for optical excitation of the molecular aggregates.

Figure 3.1 presents a summary schematic energy level diagram illustrating the excited state band splitting and selection rules for the simplest type of dye aggregates — dimers.[16,17] When chromophores are arranged such that their transition dipole moments align parallel to each other in an end to end fashion, the resulting chromophore assembly will display Jelley-aggregate (J-aggregate) behavior, with optical transitions allowed only to and from the lower energy excited state. Conversely, when the transition dipoles are instead stacked side-by-side in a parallel fashion, H-aggregate behavior is observed and optical transitions are only allowed to the higher energy excited state. For oblique configurations, wherein the transition dipole moments are not perfectly parallel, transitions to both excited state energy levels are allowed. From **Figure 3.1**, it is obvious that tuning the optical properties of aggregates requires fine spatial control over the dyes. Nature provides an example of such fine control in photosynthetic light harvesting complexes, which have evolved to maximize energy transfer efficiency.[18] While natural light harvesting systems use protein scaffolds to control intermolecular spacing and orientation, understanding protein folding and engineering artificial protein nanostructures is still in a nascent stage,[19–24] and hence rational design of artificial protein superstructures that incorporate and precisely template dyes is exceptionally difficult.
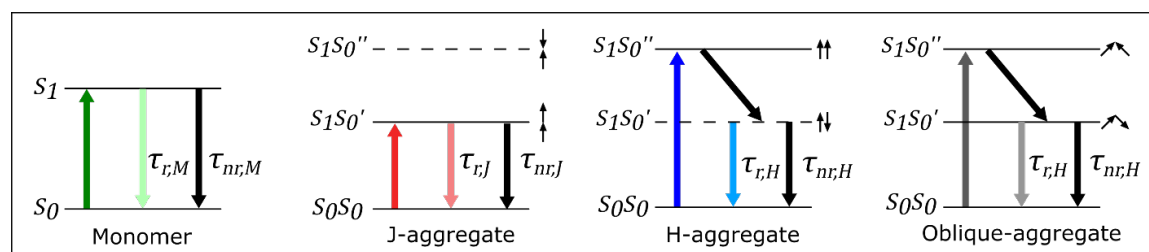
Figure 3.1. Schematic energy level diagrams of a dye monomer (far left), J-dimer (middle left), H-dimer (middle right), and oblique dimer (far right). A schematic representation of relative transition dipole moment orientations for each aggregate is shown to the right of each excitonic excited state. Solid horizontal lines indicate excitonic states that can couple optically to the ground state whereas dashed horizontal lines indicate excitonic states that cannot couple optically to the ground state. Optical transitions are shown as colored arrows for the monomer (green), J-aggregate (red), H-aggregate (blue), and oblique aggregate (gray). Optical (radiative) absorption is represented by dark colors, and optical (radiative) emission is represented by corresponding light colors. Nonradiative transitions are represented by black arrows.

Using structurally less complex DNA oligonucleotides to assemble dye molecules has proven a more tractable approach to controlling aggregation.[4,6,25–29] The relatively simple rules of Watson-Crick base pairing enable the rational design of arbitrarily shaped DNA structures. This facile design process, combined with the wide range of commercially available dyes and attendant labelling techniques for DNA, point toward the exciting prospect of using DNA to pattern coherently delocalized excitons. In particular, covalent attachment of dyes to the DNA backbone allows a high degree of spatial precision with regard to interchromophore spacing. Furthermore, the electronic coupling strength of DNA-templated dyes can be readily modulated by controlling the base pair (bp) separation.[4,6,25,28] A number of reports have demonstrated weak electronic coupling in the Förster regime achieved by spacing out dyes over large bp separations.[4,7–10,30–33] On the other hand, strong electronic coupling resulting in exciton delocalization (as evidenced by extensive spectral shifts and other optical phenomena), has only been reported in cases

where dyes are positioned directly adjacent to one another on the same strand, or opposite each other on a DNA duplex and separated by no more than a single bp.[4,6,25,28,29,34–36]

Studies of the dynamics of molecular excitons in DNA-templated dye aggregates, which are critical to their application in excitonic devices, are unfortunately scarce. In particular, the excited-state lifetime, which can change upon aggregation, is a parameter of crucial importance. Long exciton lifetimes enhance exciton transmission distance and enable more complex structures. Conversely, short lifetimes may limit the use of excitons for optoelectronic and nanoscale computing applications, highlighting the need to optimize lifetimes. While existing time-resolved studies of strongly-coupled DNA-templated dye aggregates report reduced exciton lifetimes relative to the respective monomers,[6,37,38] the mechanisms suggested for the reduced exciton lifetimes differ. One recent work suggests that aggregation enhances photoisomerization in covalently templated Cy3 dimers, thereby increasing the nonradiative decay rate and reducing the excited-state lifetime.[6] In contrast, recent work with DNA-intercalated pseudoisocyanine J-aggregates has suggested that the observed accelerated exciton dynamics result from superradiant emission enhancement.[37,38] However, it is unclear whether both processes are active in these systems, and if so, to what degree.

In this letter, we report the excited-state relaxation dynamics of two DNA-templated Cy5 dye systems that exhibit spectral signatures characteristic of strong excitonic coupling. Two representative systems were selected for this study, with one system exhibiting primarily J-aggregate behavior (i.e., J-*like* behavior) and the other primarily H-aggregate behavior (i.e., H-*like* behavior). Initial measurements utilizing steady-state spectroscopic techniques resulted in two key observations. First, a

subpopulation of highly fluorescent monomers remains in solution despite purification of the as-formed constructs. This subpopulation of monomers is accounted for in all subsequent measurements. Second, solutions of both J-like and H-like aggregate systems exhibit low fluorescence quantum yields relative to the monomer, suggesting enhanced nonradiative pathways. Subsequently, time-resolved fluorescence (TRF) and transient absorption spectroscopy (TAS) measurements are presented showing that exciton lifetimes for both the H-like and J-like aggregates are nearly two orders of magnitude shorter than that of the monomer. A quantitative analysis of the exciton lifetimes and fluorescence quantum yields indicates that nonradiative decay, in contrast to superradiance, governs exciton lifetimes in both these aggregate systems.

3.3 Results and Discussion

Following the work of Cannon *et al.* (ref. 25), two DNA-templated Cy5 aggregate constructs were selected for this work: (i) a hybridized DNA duplex bearing a pair of Cy5 dyes located directly across from each other on opposing strands (i.e., 0 bp separation) that form a strongly-coupled J-like dimer (**Figure 3.2**, middle), and (ii) a four-armed mobile Holliday junction that results in a strongly-coupled H-like tetramer of Cy5 molecules at 0 bp separation (**Figure 3.2**, bottom). In both constructs, each dye molecule is covalently attached at either end to the DNA backbone via a pair of linkers. Cy5 was chosen because in addition to being readily attached to DNA, its high molar extinction coefficient (> 200,000 M^{-1} cm^{-1}) lends itself to strong excitonic coupling, and its high fluorescence quantum yield indicates few intrinsic nonradiative decay pathways. Constructs were prepared in aqueous buffer solution according to Cannon *et al.*[25] To ensure the removal of malformed structures and excess monomer strands, the aggregate solutions were purified

by polyacrylamide gel electrophoresis (PAGE, see **Section S1**). For steady-state absorption and fluorescence measurements, samples were prepared with an optical density of 0.1 or less at the highest absorption peak; for time-resolved fluorescence and transient absorption measurements, the optical densities at the highest absorption peak were less than 0.1 and 0.3, respectively. Additional details regarding optical spectroscopy measurements and associated sample preparation can be found in **Section S2**.

The constructs were characterized via steady-state absorption spectroscopy, which provides information regarding the type and extent of electronic coupling induced by aggregation. The absorption spectrum of a single-stranded Cy5-labeled oligonucleotide, which forms the basis for both aggregate constructs, is displayed in **Figure 3.2** (top). This Cy5 monomer spectrum exhibits a single electronic absorption band, with the vibronic origin (i.e., 0-0) band peaking at ca. 647 nm. The J-dimer (**Figure 3.2**, middle) exhibits both a blue-shifted peak at ca. 597 nm and a more intense red-shifted peak at ca. 666 nm, while the H-tetramer (**Figure 3.2**, bottom) exhibits a very intense blue-shifted peak (ca. 563 nm) and suppressed absorption intensity at longer wavelengths, both signatures of strong electronic coupling in the aggregate samples (**Figure 3.1**). With the exception of the J-dimer solution's absorption spectrum, which exhibits signatures of a small amount of structural heterogeneity due to slight variations in sample preparation (see **Section S3**), these results are consistent with Cannon *et al.*,[25] who also provide the dye packing geometries associated with each of these constructs as determined via a detailed theoretical analysis of the absorption spectra.
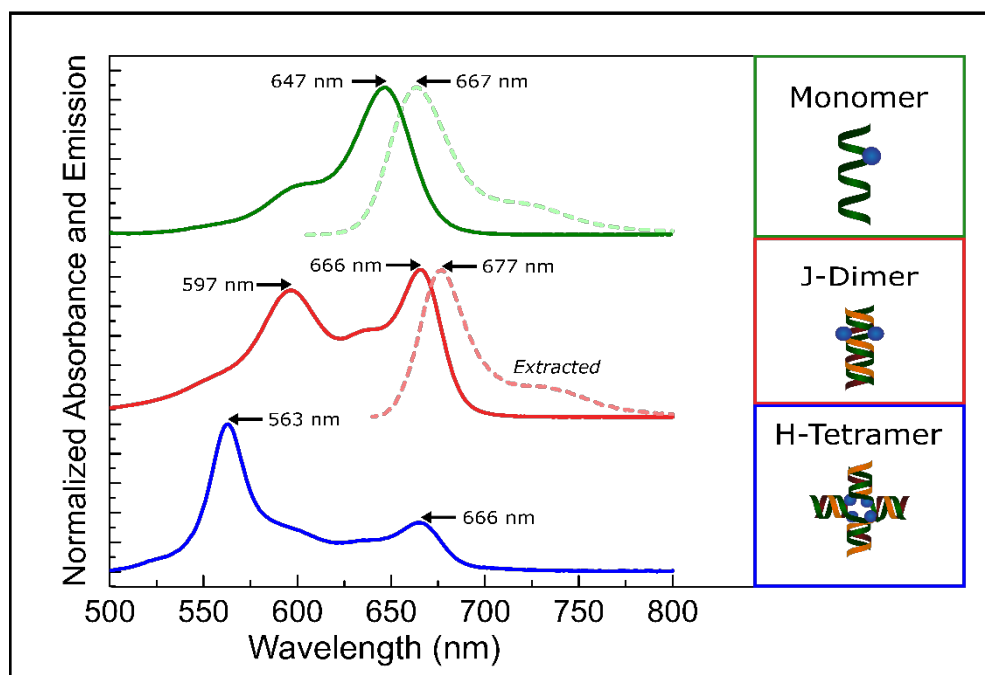
Figure 3.2. **Steady-state absorption and fluorescence emission spectra with corresponding schematic illustrations for the DNA-templated Cy5 monomer (top), J-dimer (middle), and H-tetramer (bottom). The absorption spectra for the monomer, J-dimer, and H-tetramer are plotted in dark green, red, and blue, respectively, and the emission spectra for the monomer and J-dimer are plotted as dashed lines in light green and light red, respectively. The emission spectra for both the monomer and J-dimer were obtained using an excitation wavelength of 595 nm, with the fluorescence emission of the J-dimer extracted via the method described in Section 3.6.6. As described in the main text, it was not possible to extract the H-tetramer emission spectrum.**

Steady-state fluorescence spectroscopy provides additional, complementary information about the electronic structure of the samples. The Cy5 monomer fluorescence emission is readily measured given its appreciable fluorescence quantum yield ($\Phi_F = 0.29$, see **Section S4**), and the resultant emission spectrum is essentially a mirror image of the absorption spectrum (**Figure 3.2**, top). Based on the difference in energy between the absorption and fluorescence origin bands (with the latter peaking at 667 nm), the Stokes shift for the monomer was found to be ca. 440 cm^{-1}. These values are generally consistent

with prior literature reports.[29] Initial attempts to measure the fluorescence emission of the J- and H-aggregate samples were thwarted by their highly suppressed emission intensity as compared to the monomer (fluorescence quantum yields for the J- and H-aggregate solutions were ca. 1×10^{-2} and 3×10^{-4}, respectively). Upon further inspection, fluorescence excitation measurements indicated that an additional, extremely low concentration monomer component (i.e., a subpopulation of structures that exhibited optical signatures of monomers) contributed non-negligibly to the observed fluorescence emission of both PAGE-purified aggregate solutions (**Section S5**). Accordingly, a procedure was developed to extract the 'pure' emission spectrum of each aggregate component from the corresponding as-measured fluorescence data (**Section S6**). The resultant extracted J-dimer emission spectrum is displayed in **Figure 3.2,** middle. The origin band of the J-dimer emission peaks at ca. 677 nm, which is slightly red-shifted with respect to the origin band of the J-dimer absorption (ca. 666 nm). The corresponding Stokes shift of ca. 240 cm^{-1} for the J-dimer is much smaller than the 440 cm^{-1} Stokes shift measured for the monomer, consistent with J-aggregation.[39] Due to the even more highly suppressed fluorescence emission of the H-tetramer construct, it was not possible to extract the H-tetramer's 'pure' emission spectrum in the same manner as the J-dimer, although a broad, featureless, red-shifted emission band was observed at ca. 800 nm (**Section S7**). Similar broad, featureless fluorescence emission, reminiscent of that seen from molecular 'excimers',[40] has been observed previously for H-aggregates of other cyanine-based dyes.[41,42] Critically, the fluorescence quenching observed in the aggregate solutions suggests the presence of a significant nonradiative decay pathway in the aggregates that is not present in the monomer.

With the steady-state behavior of the aggregate constructs characterized, the exciton dynamics were investigated using a time-resolved fluorescence method, time-correlated single photon counting (TCSPC). Based on each construct's respective absorption spectrum (**Figure 3.2**) and available excitation wavelengths, an excitation wavelength of 653 nm was selected for the monomer and J-dimer samples, while 507 nm was chosen to excite the H-tetramer sample. The fluorescence was then monitored near the maximum emission wavelength for each sample, corresponding to detection wavelengths of 667, 680, and 800 nm for the monomer, J-dimer, and H-tetramer samples, respectively. The detection wavelengths of 680 and 800 nm for the J-dimer and H-tetramer, respectively, were chosen to maximize the aggregate contribution and minimize the monomer contribution to the overall fluorescence decay. The resultant fluorescence decays are shown as open circles in **Figure 3.3**, with corresponding exponential decay fits shown as lines. The fluorescence decay of the monomer (**Figure 3.3**, green) was well described by a single exponential with a time constant of $\tau = 1.3$ ns, in excellent agreement with previously reported excited-state lifetimes for Cy5.[4,43,44] Interestingly, the J-dimer and H-tetramer both exhibited much faster decays than the monomer. Because of the additional subpopulation of monomers present in these samples, a biexponential function was necessary to properly fit the data (**Section S8**). The TCSPC data for the J-dimer and H-tetramer samples fit in this manner yielded a long time component of ca. 1.3 ns, consistent with a monomer contribution to the fluorescence, and a second short, instrument response limited decay component with a time constant less than ca. 250 ps. The fit parameters obtained are displayed in **Table 3.1**. The larger monomer subpopulation component contribution (A_2 in **Table 3.1**) in the J-dimer experiment is due to the fact that the monomer

and J-dimer exhibit similar optical properties (i.e., absorption and emission spectra, **Figure 3.2**) and so there is poor contrast between these components at the excitation and emission wavelengths, whereas the H-tetramer absorption and emission are well separated from that of the monomer.
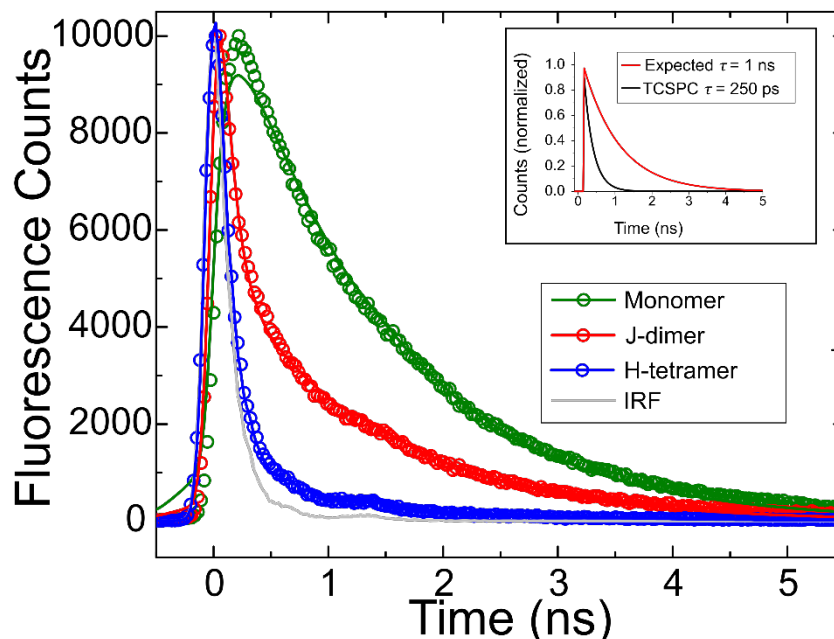
Figure 3.3. **Time-resolved fluorescence decays of solutions of the monomer (green), J-dimer (red), and H-tetramer (blue). The instrument response function (IRF) is shown in solid gray. Open circles correspond to the experimental data, while the solid lines represent exponential decay fits convolved with the IRF. Inset: The observed (black trace) versus expected (red trace) fluorescence decays for the J-dimer. The expected decay assumes classical (Kasha-type) J-aggregate behavior and that aggregation only affects the radiative decay rate (i.e., it assumes that $k_{nr,J} = k_{nr,m}$). For the purpose of illustrating the limiting case of full superradiance, it also assumes the maximum radiative rate possible, which for a dimer is $k_{r,J} = 2 \times k_{r,m}$. Full details of the derivation are reported in Section S.9.**

Table 3.1. **Excitation Wavelengths and Biexponential Fitting Parameters for TCSPC Decays**[a]

Construct	λ_{exc} (nm)	A_1 (%)	τ_1 (ns)	A_2 (%)	τ_2 (ns)
Monomer	653	N/A	1.3	N/A	N/A
J-dimer	653	87	≤ 0.25	13	1.3
H-tetramer	507	99.8	≤ 0.25	0.2	1.3

[a]The decays corresponding to the aggregate constructs were fit with the following biexponential function: $I(t) = A_1 e^{-t/\tau_1} + A_2 e^{-t/\tau_2}$. See **Section S8** for additional details regarding the mathematical and physical justification of these biexponential fits.

Insight into the nature of the accelerated fluorescence decay of the aggregates, i.e., whether radiative or nonradiative relaxation play a dominant role, can be gleaned by considering the TCSPC results in the context of molecular exciton theory. First, it is instructive to consider that the observed decay rate, k_{obs}, is equal to the sum of the radiative, k_r, and nonradiative, k_{nr}, decay rates (i.e., $k_{obs} = k_r + k_{nr}$).[45] The first of these terms, k_r, can be evaluated according to molecular exciton theory.[17,46] For example, k_r is enhanced in a J-aggregate, an effect known colloquially as superradiance.[47] In an ideal J-aggregate (**Figure 3.1**, middle left), $k_{r,J}$ is equivalent to the product of the number of molecules comprising the aggregate, N, and the radiative rate of a single molecule (i.e. $k_{r,J} = N \times k_{r,m}$).[47,48] Conversely, for an H-aggregate, $k_{r,H}$ is suppressed and, for an ideal H-aggregate (**Figure 3.1**, middle right) where the optical transition between the lowest excited state (S_1S_0') and the ground state (S_0S_0) is forbidden, $k_{r,H} = 0$. Because molecules typically pack in an oblique manner (**Figure 3.1**, right) or in a manner that is neither pure J nor H, these ideal limits generally are not realized. More typically, mixed J- or H-like behavior is observed, as in the present case (**Figure 3.2**). For these real systems, insights into the radiative decay rate can be gleaned from the experimentally-measured extinction spectrum. For example, Strickler and Berg showed that the radiative rate is directly related to the

intensity of absorption into the lowest-energy singlet excited state.[49] While a quantitative analysis of the radiative decay rate of the J- and H-like constructs is complicated by several factors, including structural heterogeneity and overlapping transitions to (S_1S_0)' and (S_1S_0)'' states, we know from prior work[25] that the extinction of their lowest-energy singlet absorption band is increased and decreased, respectively. Relative to the monomer ($k_{r,m}$), we can therefore expect the radiative rate to be enhanced for the J-dimer ($k_{r,J}$) and suppressed for the H-tetramer ($k_{r,H}$), where m, J, and H, indicate the monomer, J-dimer, and H-tetramer, respectively.

Considering that exciton theory predicts an enhanced and suppressed k_r for the J-dimer and H-tetramer, respectively, and employing the previous assumption that k_{nr} is uninfluenced by aggregation (i.e., $k_{nr,aggregate} = k_{nr,m}$), we expect k_{obs} for the J-dimer and H-tetramer to be enhanced and suppressed, respectively. **Figure 3.3** shows that the fluorescence decay of the H-tetramer is significantly accelerated with respect to the monomer. Since an aggregation-induced decrease in k_r should serve to *increase* the fluorescence lifetime of the H-tetramer, this unexpected observed decrease in the fluorescence lifetime can only be accounted for by a significant increase in the nonradiative rate for the H-tetramer, $k_{nr,H}$. **Figure 3.3** shows that the fluorescence decay of the J-dimer is also significantly accelerated with respect to the monomer. Here, we can place bounds on the extent to which superradiance contributes to the overall enhanced decay. By covalently tethering two Cy5 dyes to the DNA template, we can guarantee that two, and only two, dye molecules interact. This means that we can expect a $k_{r,J}$ rate enhancement of at most $2 \times k_{r,m}$. The inset of **Figure 3.3** shows the fluorescence decay expected for the J-dimer according to these assumptions, which yields a time constant of 1.0 ns (red curve;

see **Section 3.6.9**). Also shown in the **Figure 3.3** inset is a single exponential decay generated for the J-dimer based on the measured, instrument response-limited fluorescence lifetime (black curve), which decays considerably faster than the decay expected for solely radiative enhancement (red trace). This discrepancy between the expected and actual fluorescence decay rates shows that new and significant nonradiative decay channels emerge in the J-dimer. Hence, for both types of aggregates, the TCSPC measurements confirm that significantly enhanced nonradiative relaxation is introduced upon aggregation.

In order to better understand the nonradiative relaxation in the aggregate constructs, we turned to ultrafast transient absorption spectroscopy (TAS). Significantly, TAS provides information on both bright and dark states, such as triplets and photoisomers, and can additionally elucidate whether the initial photoexcitation returns directly to the ground state and, if so, on what timescale. Furthermore, since the response time of the TAS system is nearly 3 orders of magnitude faster than the TCSPC system (Supporting Information S.10), we can potentially directly time resolve the excited state decay and quantify the extent of the nonradiative relaxation contribution. For the TAS measurements, each sample was excited and probed near its respective absorption maximum for maximal signal to noise, with wavelengths of 650, 675, and 565 nm used for the monomer, J-dimer, and H-tetramer, respectively (Supporting Information S.11). Note that to improve contrast with the underlying subpopulation of monomers, the J-dimer sample was excited and probed at 675 nm, which is slightly red-shifted relative to its absorption maximum (see **Figure 3.2**).

The transient absorption (TA) decays for the monomer and aggregate samples are displayed in **Figure 3.4**. All samples show a positive ground state bleach signal that decays

with time. A single exponential fit described the monomer TA decay well and returned a time constant of 1.5 ns, in good agreement with the lifetime measured by TCSPC. Furthermore, the recovery of the ground-state bleach signal to baseline indicates that the monomer relaxes directly to the ground state with very low probability of photoisomerization or intersystem crossing.[50] For the aggregate solutions, a significantly more rapid initial recovery of the ground state bleach is observed. As with the TCSPC data, an additional long-time component consistent with a subpopulation of monomers was observed, and hence a biexponential fit was necessary to accurately model these data. Significantly, the short time constants corresponding to ground state recovery of the aggregate species were found to be 11 and 35 ps for the J-dimer and H-tetramer, respectively. Wavelength- and fluence-dependence measurements (**Section S12** and **Section S13**) indicate that the measured lifetimes are representative of the intrinsic exciton lifetimes; that is, the measurements are not complicated by additional decay pathways, such as internal conversion from high-lying excited states or exciton-exciton annihilation, nor the structural heterogeneity identified in **Section S3**. Quantitative analysis of the TA data (**Section S14**) reveals the excited-state dynamics of the aggregate constructs are nearly exclusively governed by nonradiative processes, with 99.6% of ground state recovery being nonradiative in nature for the J-dimer and 99.96% nonradiative for the H-tetramer.
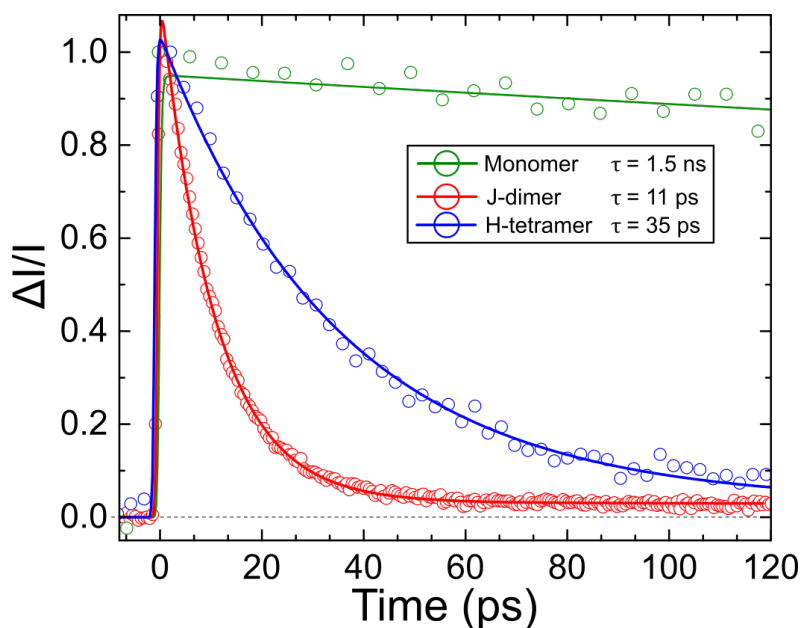
Figure 3.4. **Transient absorption measurements on solutions of the monomer (green), J-dimer (red), and H-tetramer (blue). The open circles correspond to the experimental data, while the solid lines represent single or biexponential fits to the data (see main text for additional details). The data are scaled to unity with a positive scalar to preserve the sign of the signal.**

Having quantified the nonradiative contribution to the overall decay, the underlying microscopic decay mechanism can be examined. In view of the rapid nature of the nonradiative relaxation of the aggregate constructs (i.e., tens of ps), both intersystem crossing and photoisomerization can be ruled out as contributing significantly to the nonradiative decay. While intersystem crossing and photoisomerization can be rapid in certain systems, these processes occur on a microsecond timescale for Cy5 attached to DNA,[50] and it is difficult to envision how aggregation would accelerate their kinetics by nearly six orders of magnitude. For example, there are no 'heavy atoms' in this Cy5 derivative (**Section S1**) to facilitate intersystem crossing in the aggregate constructs, and steric hindrance due to the presence of adjacent molecules would tend to decrease rather than increase the rate of photoisomerization. Additionally, charge transfer is ruled out for

reasons discussed in **Section S15**. A seminal contribution by Sundström and Gillbro studying dithiadicarbocyanine, a compound structurally very similar to Cy5, also observed drastically accelerated nonradiative decay in aggregated sytems.[51] In that work, the authors concluded the nonradiative decay was facilitated by an electric dipole-dipole coupling mechanism; this, however, was later disputed[52] on the basis that the trend the authors observed for the exciton lifetime with respect to the dielectric constant of the medium was inconsistent with a decay mechanism based on electric dipole-dipole coupling. These previous studies (refs. 50 and 52) indicate that, in addition to nonradiative decay via photoisomerization and intersystem crossing, nonradiative decay via electric dipole-dipole coupling can be ruled out. This indicates direct relaxation to the ground state via strong nonadiabatic coupling, i.e., internal conversion, must be the dominant mechanism governing the short exciton lifetimes of the Cy5 aggregates. Given that such rapid nonradiative relaxation is observed in both H- and J-aggregates of even more structurally rigid compounds (e.g., cresyl violet,[53,54] methylene blue[51,52] and structurally very similar thionine,[51,55] Nile blue,[56] porphyrins,[57,58,59] and phthalocyanines[60,61]) where photoinduced isomerization is not possible, we further conclude that radiationless, nonadiabatic transitions from S_1S_0 directly to S_0S_0 (and, in the present case, the thermally-stable *trans* isomer[62] form of S_0S_0) may represent a general decay pathway that emerges in systems comprising excitonically-coupled dye aggregates.

3.4 Conclusion

In conclusion, we have investigated the excited-state dynamics of strongly-coupled J-aggregate (dimer) and H-aggregate (tetramer) constructs formed through covalent attachment of cyanine-based (Cy5) dyes to DNA. Steady-state absorption and fluorescence

spectroscopy indicated that fluorescence emission was strongly quenched in the aggregate solutions, and the majority of this emission arises from a small subpopulation of highly-emissive monomers. Quenched fluorescence emission suggests a new nonradiative decay pathway is introduced upon aggregation, which was confirmed via an analysis of TCSPC measurements in the context of molecular exciton theory. Finally, the extent to which nonradiative decay contributes to the relaxation dynamics was quantified with TAS. The exciton lifetimes of the J-dimer and H-tetramer were measured to be ca. 11 and 35 ps, respectively, indicating that nonradiative decay is largely (>99%) responsible for the relaxation dynamics of both types of aggregates studied here, which we attribute to a rapid nonadiabatic transition between S_1S_0 and S_0S_0. Identifying the dominant relaxation mechanism in DNA-templated dye aggregates as direct internal conversion to the ground state presents the tantalizing possibility of optimally tuning exciton lifetimes for optoelectronic and nanoscale computing applications by rationally modifying either the DNA backbone or dye structure.

3.5 Acknowledgments

3.6 References

(1)   Mirkovic, T.; Ostroumov, E. E.; Anna, J. M.; Grondelle, R. Van; Govindjee; Scholes, G. D. Light Absorption and Energy Transfer in the Antenna Complexes of Photosynthetic Organisms. *Chem. Rev.* **2017**, *117* (2), 249–293.

(2)   Ostroverkhova, O. Organic Optoelectronic Materials: Mechanisms and Applications. *Chem. Rev.* **2016**, *116* (22), 13279–13412.

(3)   Brixner, T.; Hildner, R.; Köhler, J.; Lambert, C.; Würthner, F. Exciton Transport in Molecular Aggregates – From Natural Antennas to Synthetic Chromophore Systems. *Adv. Energy Mater.* **2017**, *7* (16), 1–33.

(4)   Cunningham, P. D.; Khachatrian, A.; Buckhout-White, S.; Deschamps, J. R.; Goldman, E. R.; Medintz, I. L.; Melinger, J. S. Resonance Energy Transfer in DNA Duplexes Labeled with Localized Dyes. *J. Phys. Chem. B* **2014**, *118* (50), 14555–14565.

(5)   Melinger, J. S.; Khachatrian, A.; Ancona, M. G.; Buckhout-White, S.; Goldman, E. R.; Spillmann, C. M.; Medintz, I. L.; Cunningham, P. D. FRET from Multiple Pathways in Fluorophore-Labeled DNA. *ACS Photonics* **2016**, *3* (4), 659–669.

(6)   Cunningham, P. D.; Kim, Y. C.; Díaz, S. A.; Buckhout-White, S.; Mathur, D.; Medintz, I. L.; Melinger, J. S. Optical Properties of Vibronically Coupled Cy3 Dimers on DNA Scaffolds. *J. Phys. Chem. B* **2018**, *122* (19), 5020–5029.

(7)   Graugnard, E.; Kellis, D. L.; Bui, H.; Barnes, S.; Kuang, W.; Lee, J.; Hughes, W. L.; Knowlton, W. B.; Yurke, B. DNA-Controlled Excitonic Switches. *Nano Lett.* **2012**, *12* (4), 2117–2122.

(8)   Cannon, B. L.; Kellis, D. L.; Davis, P. H.; Lee, J.; Kuang, W.; Hughes, W. L.; Graugnard, E.; Yurke, B.; Knowlton, W. B. Excitonic AND Logic Gates on DNA Brick Nanobreadboards. *ACS Photonics* **2015**, *2* (3), 398–404.

(9)   Kellis, D. L.; Rehn, S. M.; Cannon, B. L.; Davis, P. H.; Graugnard, E.; Lee, J.; Yurke, B.; Knowlton, W. B. DNA-Mediated Excitonic Upconversion FRET Switching. *New J. Phys.* **2015**, *17* (11), 115007.

(10)   Wang, S.; Lebeck, A. R.; Dwyer, C. Nanoscale Resonance Energy Transfer-Based Devices for Probabilistic Computing. *IEEE Micro* **2015**, *35* (5), 72–84.

(11)   Sawaya, N. P. D.; Rappoport, D.; Tabor, D. P.; Aspuru-Guzik, A. Excitonics: A Set of Gates for Molecular Exciton Processing and Signaling. *ACS Nano* **2018**, *12* (7), 6410–6420.

(12)   Jelley, E. E. Spectral Absorption and Fluorescence of Dyes in the Molecular State. *Nature* **1936**, *138* (3502), 1009–1010.

(13)   Jelley, E. E. Molecular, Nematic and Crystal States of I: I-Diethyl--Cyanine Chloride. *Nature* **1937**, *139* (3519), 631–631.

(14)   Scheibe, G. Über Die Veränderlichkeit Der Absorptionsspektren in Lösungen Und Die Nebenvalenzen Als Ihre Ursache. *Angew. Chemie* **1937**, *50* (11), 212–219.

(15)   Davydov, A. S. Theory of Absorption Spectra of Molecular Crystals. *Transl. Repr. from Zh. Eksp. Teor. Fiz.* **1948**, *18* (2), 210–218.

(16)   Kasha, M. Energy Transfer Mechanisms and the Molecular Exciton Model for Molecular Aggregates. *Radiat. Res.* **1963**, *20* (1), 55–70.

(17)   Kasha, M.; Rawls, H. R.; Ashraf El-Bayoumi, M. The Exciton Model in Molecular Spectroscopy. *Pure Appl. Chem.* **1965**, *11* (3–4), 371–392.

(18)   Scholes, G. D.; Fleming, G. R.; Olaya-Castro, A.; Van Grondelle, R. Lessons from Nature about Solar Light Harvesting. *Nat. Chem.* **2011**, *3* (10), 763–774.

(19)   Snow, C. D.; Nguyen, H.; Pande, V. S.; Gruebele, M. Absolute Comparison of Simulated and Experimental Protein-Folding Dynamics. *Nature* **2002**, *420* (6911), 102–106.

(20)   Baker, D.; Sali, A. Protein Structure Prediction and Structural Genomics. *Science.* **2001**, *294* (5540), 93–96.

(21)   Dill, K. A.; MacCallum, J. L. The Protein-Folding Problem, 50 Years On. *Science.* **2012**, *338* (6110), 1042–1046.

(22)   Yeates, T. O. Geometric Principles for Designing Highly Symmetric Self-Assembling Protein Nanomaterials. *Annu. Rev. Biophys.* **2017**, *46* (1), 23–42.

(23)   Huang, P. S.; Boyken, S. E.; Baker, D. The Coming of Age of de Novo Protein Design. *Nature* **2016**, *537* (7620), 320–327.

(24)   Bale, J. B.; Gonen, S.; Liu, Y.; Sheffler, W.; Ellis, D.; Thomas, C.; Cascio, D.; Yeates, T. O.; Gonen, T.; King, N. P.; et al. Accurate Design of Megadalton-Scale Two-Component Icosahedral Protein Complexes. *Science.* **2016**, *353* (6297), 389–395.

(25)   Cannon, B. L.; Kellis, D. L.; Patten, L. K.; Davis, P. H.; Lee, J.; Graugnard, E.; Yurke, B.; Knowlton, W. B. Coherent Exciton Delocalization in a Two-State DNA-Templated Dye Aggregate System. *J. Phys. Chem. A* **2017**, *121* (37), 6905–6916.

(26)   Cannon, B. L.; Patten, L. K.; Kellis, D. L.; Davis, P. H.; Lee, J.; Graugnard, E.; Yurke, B.; Knowlton, W. B. Large Davydov Splitting and Strong Fluorescence Suppression: An Investigation of Exciton Delocalization in DNA-Templated Holliday Junction Dye Aggregates. *J. Phys. Chem. A* **2018**, *122* (8), 2086–2095.

(27)   Teo, Y. N.; Kool, E. T. DNA-Multichromophore Systems. *Chem. Rev.* **2012**, *112* (7), 4221–4245.

(28)   Nicoli, F.; Roos, M. K.; Hemmig, E. A.; Di Antonio, M.; De Vivie-Riedle, R.; Liedl, T. Proximity-Induced H-Aggregation of Cyanine Dyes on DNA-Duplexes. *J. Phys. Chem. A* **2016**, *120* (50), 9941–9947.

(29)   Markova, L. I.; Malinovskii, V. L.; Patsenker, L. D.; Häner, R. J- vs. H-Type Assembly: Pentamethine Cyanine (Cy5) as a near-IR Chiroptical Reporter. *Chem. Commun.* **2013**, *49* (46), 5298–5300.

(30)   Melinger, J. S.; Khachatrian, A.; Ancona, M. G.; Buckhout-White, S.; Goldman, E. R.; Spillmann, C. M.; Medintz, I. L.; Cunningham, P. D. FRET from Multiple Pathways in Fluorophore-Labeled DNA. *ACS Photonics* **2016**, *3* (4), 659–669.

(31)   Klein, W. P.; Díaz, S. A.; Buckhout-White, S.; Melinger, J. S.; Cunningham, P. D.; Goldman, E. R.; Ancona, M. G.; Kuang, W.; Medintz, I. L. Utilizing HomoFRET to Extend DNA-Scaffolded Photonic Networks and Increase Light-Harvesting Capability. *Adv. Opt. Mater.* **2018**, *6* (1), 1–12.

(32)   Heilemann, M.; Tinnefeld, P.; Mosteiro, G. S.; Parajo, M. G.; Van Hulst, N. F.; Sauer, M. Multistep Energy Transfer in Single Molecular Photonic Wires. *J. Am. Chem. Soc.* **2004**, *126* (21), 6514–6515.

(33)   Massey, M.; Medintz, I. L.; Ancona, M. G.; Algar, W. R. Time-Gated FRET and DNA-Based Photonic Molecular Logic Gates: AND, OR, NAND, and NOR. *ACS Sensors* **2017**, *2* (8), 1205–1214.

(34) Asanuma, H.; Fujii, T.; Kato, T.; Kashida, H. Coherent Interactions of Dyes Assembled on DNA. *J. Photochem. Photobiol. C Photochem. Rev.* **2012**, *13* (2), 124–135.

(35) Kringle, L.; Sawaya, N. P. D.; Widom, J.; Adams, C.; Raymer, M. G.; Aspuru-Guzik, A.; Marcus, A. H. Temperature-Dependent Conformations of Exciton-Coupled Cy3 Dimers in Double-Stranded DNA. *J. Chem. Phys.* **2018**, *148* (8), 85101.

(36) Heussman, D.; Kittell, J.; Kringle, L.; Tamimi, A.; von Hippel, P. H.; Marcus, A. H. Measuring Local Conformations and Conformational Disorder of (Cy3)2 Dimer Labeled DNA Fork Junctions Using Absorbance, Circular Dichroism and Two-Dimensional Fluorescence Spectroscopy. *Faraday Discuss.* **2019**, No. DOI: 10.1039/C8FD00245B.

(37) Banal, J. L.; Kondo, T.; Veneziano, R.; Bathe, M.; Schlau-Cohen, G. S. Photophysics of J-Aggregate-Mediated Energy Transfer on DNA. *J. Phys. Chem. Lett.* **2017**, *8* (23), 5827–5833.

(38) Boulais, E.; Sawaya, N. P. D.; Veneziano, R.; Andreoni, A.; Banal, J. L.; Kondo, T.; Mandal, S.; Lin, S.; Schlau-Cohen, G. S.; Woodbury, N. W.; et al. Programmed Coherent Coupling in a Synthetic DNA-Based Excitonic Circuit. *Nat. Mater.* **2018**, *17* (2), 159–166.

(39) Würthner, F.; Kaiser, T. E.; Saha-Möller, C. R. J-Aggregates: From Serendipitous Discovery to Supramolecular Engineering of Functional Dye Materials. *Angew. Chemie - Int. Ed.* **2011**, *50* (15), 3376–3410.

(40) Pensack, R. D.; Ashmore, R. J.; Paoletta, A. L.; Scholes, G. D. The Nature of Excimer Formation in Crystalline Pyrene Nanoparticles. *J. Phys. Chem. C* **2018**, *122* (36), 21004–21017.

(41) Rösch, U.; Yao, S.; Wortmann, R.; Würthner, F. Fluorescent H-Aggregates of Merocyanine Dyes. *Angew. Chemie - Int. Ed.* **2006**, *45* (42), 7026–7030.

(42) Ryu, N.; Okazaki, Y.; Pouget, E.; Takafuji, M.; Nagaoka, S.; Ihara, H.; Oda, R. Fluorescence Emission Originated from H-Aggregated Cyanine Dye with Chiral Gemini Surfactant Assemblies Having Narrow Absorption Band and Remarkably Large Stokes Shift. *Chem. Commun.* **2017**, *53* (63), 8870–8873.

(43) Huang, Z.; Ji, D.; Wang, S.; Xia, A.; Koberling, F.; Patting, M.; Erdmann, R. Spectral Identification of Specific Photophysics of Cy5 by Means of Ensemble and Single Molecule Measurements. *J. Phys. Chem. A* **2006**, *110* (1), 45–50.

(44) Singh, M. K. Time-Resolved Single Molecule Fluorescence Spectroscopy of Cy5-dCTP: Influence of the Immobilization Strategy. *Phys. Chem. Chem. Phys.* **2009**, *11* (33), 7225–7230.

(45) Turro, N. J.; Scaiano, J. C.; Ramamurthy, V. *Modern Molecular Photochemistry of Organic Molecules*; University Science Books: Sausalito, Calif, 2010.

(46) Hestand, N. J.; Spano, F. C. Molecular Aggregate Photophysics beyond the Kasha Model: Novel Design Principles for Organic Materials. *Acc. Chem. Res.* **2017**, *50* (2), 341–350.

(47) Dicke, R. H. Coherence in Spontaneous Radiation Process. *Phys. Rev.* **1954**, *93* (1), 99–110.

(48) Spano, F. C.; Kuklinski, J. R.; Mukamel, S. Cooperative Radiative Dynamics in Molecular Aggregates. *J. Chem. Phys.* **1991**, *94* (11), 7534–7544.

(49) Strickler, S. J.; Berg, R. A. Relationship between Absorption Intensity and Fluorescence Lifetime of Molecules. *J. Chem. Phys.* **1962**, *37* (4), 814–822.

(50) Widengren, J.; Schwille, P. Characterization of Photoinduced Isomerization and Back-Isomerization of the Cyanine Dye Cy5 by Fluorescence Correlation Spectroscopy. *J. Phys. Chem. A* **2000**, *104* (27), 6416–6428.

(51) Sundström, V.; Gillbro, T. Excited State Dynamics and Photophysics of Aggregated Dye Chromophores in Solution. *J. Chem. Phys.* **1985**, *83* (6), 2733–2743.

(52) Dean, J. C.; Oblinsky, D. G.; Rafiq, S.; Scholes, G. D. Methylene Blue Exciton States Steer Nonradiative Relaxation: Ultrafast Spectroscopy of Methylene Blue Dimer. *J. Phys. Chem. B* **2016**, *120* (3), 440–454.

(53) Kreller, D. I.; Kamat, P. V. Photochemistry of Sensitizing Dyes. Spectroscopic and Redox Properties of Cresyl Violet. *J. Phys. Chem* **1991**, *95* (11), 4406–4410.

(54) Martini, I.; Hartland, G. V; Kamat, P. V. Ultrafast Photophysical Investigation of Cresyl Violet Aggregates Adsorbed onto Nanometer-Sized Particles of SnO2 and SiO2. *J. Phys. Chem. B* **1997**, *101* (24), 4826–4830.

(55) Das, S.; Kamat, P. V. Can H-Aggregates Serve as Light-Harvesting Antennae? Triplet−Triplet Energy Transfer between Excited Aggregates and Monomer Thionine in Aersol-OT Solutions. *J. Phys. Chem. B* **1999**, *103* (1), 209–215.

(56) Nasr, C.; Hotchandani, S. Excited-State Behavior of Nile Blue H-Aggregates Bound to SiO2 and SnO2 Colloids. *Chem. Mater.* **2000**, *12* (6), 1529–1535.

(57) Kelbauskas, L.; Bagdonas, S.; Dietel, W.; Rotomskis, R. Excitation Relaxation and Structure of TPPS4 J-Aggregates. *J. Lumin.* **2003**, *101* (4), 253–262.

(58) Collini, E.; Ferrante, C.; Bozio, R. Influence of Excitonic Interactions on the Transient Absorption and Two-Photon Absorption Spectra of Porphyrin J-Aggregates in the NIR Region. *J. Phys. Chem. C* **2007**, *111* (50), 18636–18645.

(59) Verma, S.; Ghosh, A.; Das, A.; Ghosh, H. N. Ultrafast Exciton Dynamics of J- and H-Aggregates of the Porphyrin-Catechol in Aqueous Solution. *J. Phys. Chem. B* **2010**, *114* (25), 8327–8334.

(60) Kakade, S.; Ghosh, R.; Palit, D. K. Excited State Dynamics of Zinc-Phthalocyanine Nanoaggregates in Strong Hydrogen Bonding Solvents. *J. Phys. Chem. C* **2012**, *116* (28), 15155–15166.

(61) Caplins, B. W.; Mullenbach, T. K.; Holmes, R. J.; Blank, D. A. Intermolecular Interactions Determine Exciton Lifetimes in Neat Films and Solid State Solutions of Metal-Free Phthalocyanine. *J. Phys. Chem. C* **2015**, *119* (49), 27340–27347.

(62) Sanchez-Galvez, A.; Hunt, P.; Robb, M. A.; Olivucci, M.; Vreven, T.; Schlegel, H. B. Ultrafast Radiationless Deactivation of Organic Dyes: Evidence for a Two-State Two-Mode Pathway in Polymethine Cyanines. *J. Am. Chem. Soc.* **2000**, *122* (12), 2911–2924.

CHAPTER FOUR: EXCITED-STATE LIFETIMES OF DNA-TEMPLATED

CYANINE DIMER, TRIMER, AND TETRAMER AGGREGATES: THE ROLE OF

EXCITON DELOCALIZATION, DYE SEPARATION, AND DNA HETEROGENEITY

This chapter is published by the American Chemical Society in *The Journal of Physical Chemistry B* and should be referenced appropriately

Reference:

Huff, J. S.; Turner, D. B.; Mass, O. A.; Patten, L. K.; Wilson, C. K.; Roy, S. K.; Barclay, M. S.; Yurke, B.; Knowlton, W. B.; Davis, P. H.; Pensack, R. D. Excited-State Lifetimes of DNA-Templated Cyanine Dimer, Trimer, and Tetramer Aggregates: The Role of Exciton Delocalization, Dye Separation, and DNA Heterogeneity. *J. Phys. Chem. B* **2021**, *125*, 10240–10259

*This chapter includes modifications from the originally published version.

4.1 Abstract

DNA-templated molecular (dye) aggregates are a novel class of materials that have garnered attention in a broad range of areas including light harvesting, sensing, and computing. Using DNA to template dye aggregation is attractive due to the relative ease with which DNA nanostructures can be assembled in solution, the diverse array of nanostructures that can be assembled, and the ability to precisely position dyes to within a few Angstroms of one another. These factors, combined with the programmability of DNA, raise the prospect of designer materials custom tailored for specific applications. While considerable progress has been made in characterizing the optical properties and associated electronic structure of these materials, less is known about their excited-state dynamics. For example, little is known about how the excited-state lifetime, a parameter essential to many applications, is influenced by structural factors, such as the number of dyes within the aggregate and their spatial arrangement. In this work, we use a combination of transient absorption spectroscopy and global target analysis to measure excited-state lifetimes in a series of DNA-templated cyanine dye aggregates. Specifically, we investigate six distinct dimer, trimer, and tetramer aggregates—based on the ubiquitous cyanine dye Cy5— templated using both duplex and Holliday junction DNA nanostructures. We find that these DNA-templated Cy5 aggregates all exhibit significantly reduced excited-state lifetimes, some by more than two orders-of-magnitude, and observe considerable variation among the lifetimes. We attribute the reduced excited-state lifetimes to enhanced nonradiative decay and proceed to discuss various structural factors, including exciton delocalization, dye separation, and DNA heterogeneity, that may contribute to the observed reduction and variability of excited-state lifetimes. Guided by insights from structural modeling, we find

that the reduced lifetimes and enhanced nonradiative decay are most strongly correlated with the distance between the dyes. These results inform potential tradeoffs between dye separation, excitonic coupling strength, and excited-state lifetime that motivate deeper mechanistic understanding, potentially via further dye and dye template design.

4.2 Introduction

Molecular (dye) aggregates, which can form delocalized collective excitations called excitons, are central to a number of applications including natural and artificial light harvesting,[1,2] organic optoelectronics,[3] sensing,[4–6] and nanoscale computing.[7–12] The role of dye aggregates in some of these applications is to efficiently absorb light and transfer it to a reaction center, charge-transfer interface, or across an excitonic wire.[1–4,10] Any losses along the way reduce the overall efficiency of the energy transfer process. Conversely, dye aggregates have found a role in other applications such as sensing[5,6] or photothermal therapy[13,14] for their ability to quench emitted light, i.e., quickly convert light energy into heat. Here, the contrast between the highly emissive monomer dyes and weakly emissive dye aggregates is essential. Thus, developing an understanding of the nonradiative processes that lead to quenching in dye aggregates can both improve the overall efficiency of energy conversion and computing applications as well as potentially enhance overall contrast in sensing applications.

Since the discovery of dye aggregates in the 1930s by Scheibe and Jelley,[15,16] a considerable amount of research has been dedicated to better understanding their unique electronic structure. Kasha, following Davydov's work on molecular crystals,[17,18] highlighted that many dye aggregate optical properties, such as new and shifted absorption bands, can be explained by a relatively simple model based on the mutual orientation of the transition dipole moments (TDMs) of constituent dyes. Kasha's description of dye aggregation can, in many cases, accurately predict the energy-level splitting and redistribution of oscillator strength concomitant with dye aggregation. Kasha's model, for example, predicts that when dyes pack with their TDMs in an end-to-end (J-aggregate) or

stacked (H-aggregate) configuration, the absorption spectrum is redshifted or blueshifted, respectively, compared to the individual dye. The energy shift is largely related to whether transitions from the ground state to the lowest- or highest-energy excitonic states are allowed. In a J-aggregate, transitions to the lowest- and highest-energy excitonic states are optically allowed and forbidden, respectively, while the opposite is true for H-aggregates. It is worthwhile to note that more recently the theoretical treatment of the electronic structure of dye aggregates has been further refined to include vibronic[19] and charge-transfer[20,21] coupling, the latter of which becomes important at small intermolecular distances.

While great progress has been made in understanding the electronic structure of dye aggregates, challenges remain in understanding their dynamical properties. Excited-state lifetimes, which are essential to any application utilizing dye aggregates, are a dynamical property controlled by both radiative and nonradiative decay processes.[22] As noted above, optical transitions between the ground and lowest-energy excited states of J- and H-aggregates are allowed and forbidden, respectively. Given that emission is the inverse of absorption and involves the same electronic states, insight into the radiative decay rate can be gained from the static electronic structure. For example, the TDMs of dyes in a perfect J-aggregate sum together constructively, which enhances the radiative rate compared with the monomer. For a perfect H-aggregate, in contrast, the TDMs of the dyes destructively interfere, causing the radiative rate to become zero. This is the reason why, assuming nonradiative decay rates have not changed, it is generally suggested that J- and H-aggregates are emissive and dark, respectively. Although the effect of aggregation on the radiative rate is fairly well understood, in practice, several works have shown that

nonradiative decay processes can play a more predominant role in dye aggregate photophysics, ultimately governing their excited-state lifetimes.[14,23–25] Clearly, developing a deeper understanding of excited-state lifetimes in dye aggregates, particularly the role of nonradiative decay processes, is of utmost importance.

There are a variety of ways to form dye aggregates. Dye aggregates can be formed spontaneously in concentrated solutions, well above the solubility limit, as was originally demonstrated by Scheibe and Jelley.[15,16] Some control of the aggregate character in solutions of spontaneously aggregating dyes can be achieved through alterations of the solvent conditions such as the ionic strength and composition,[26] solvent polarity, and temperature. Dye substituents can be modified to affect aggregate packing as well.[27] However, strict control of the number of dyes in an aggregate is not possible for spontaneously formed aggregates larger than a dimer. Natural systems use proteins to overcome this limitation, which has resulted in sophisticated supramolecular assemblies for light harvesting.[1,28] The examples from nature demonstrate that high specificity with regard to the number of interacting dyes, dye placement, and orientation is possible. Although considerable progress has been made in predicting how proteins fold,[29–34] to date artificial protein-templated dye aggregates have yet to be demonstrated, likely due to complexities arising from adding a dye to the protein structure. Using DNA to template dye aggregates represents an alternative, promising approach. In contrast to amino acids, nucleic acids have relatively simple pairing rules, i.e., Watson-Crick base pairing, yet can form a diverse array of structures including duplexes, Holliday junctions, and higher-order structures.[35–39] Many early, pioneering works used duplex DNA to template dye aggregates via physisorption.[40–42] More recently, an even higher level of precision and versatility has

been achieved by covalently-tethering dyes to DNA.[24,43–48] Such precision and versatility enables the controlled assembly of dye aggregates with distinct packing geometries[24,47,49] and dye aggregate networks with a specific number of constituent dyes,[47,49,50] facilitating the study of structure-function relationships and design of aggregates with properties custom tailored and optimized for specific applications.

Cyanines are ubiquitous dyes, by far the most commonly employed family of dyes in covalently-tethered DNA templating.[46,49,51–54] Of these dyes, the pentamethine dye Cy5 (**Scheme 4.1**) is particularly attractive due to its strong absorption (i.e., TDM of ~16 D [ref. 55] and associated peak extinction coefficient of ~250,000 M^{-1} cm^{-1}) in the visible spectral range ($\lambda_{max} \sim 650$ nm). According to Kasha's molecular exciton model,[56,57] the excitonic hopping parameter, J, sometimes referred to as the excitonic coupling strength, is directly proportional to the square of the TDM. Thus, a large TDM may lead to a large J. Indeed, our recent work has shown that J can be as large as 800 cm^{-1} (100 meV) in certain DNA-templated Cy5 aggregates.[49,58] Additionally, Cy5 is quite photostable. Cy5 has a relatively high fluorescence quantum yield of ~0.3,[25,59] indicating that radiative decay is able to effectively compete with nonradiative decay processes. This results in a fairly long ~1.5 ns lifetime for a Cy5 monomer, which we showed previously was dramatically reduced in dimer and tetramer aggregates due to accelerated nonradiative decay.[25] The physical origin of this accelerated nonradiative decay, however, remains elusive. Furthermore, the generality of this effect and whether it depends on packing configuration, such as the number of dyes and the distance and orientation between them, has yet to be explored.
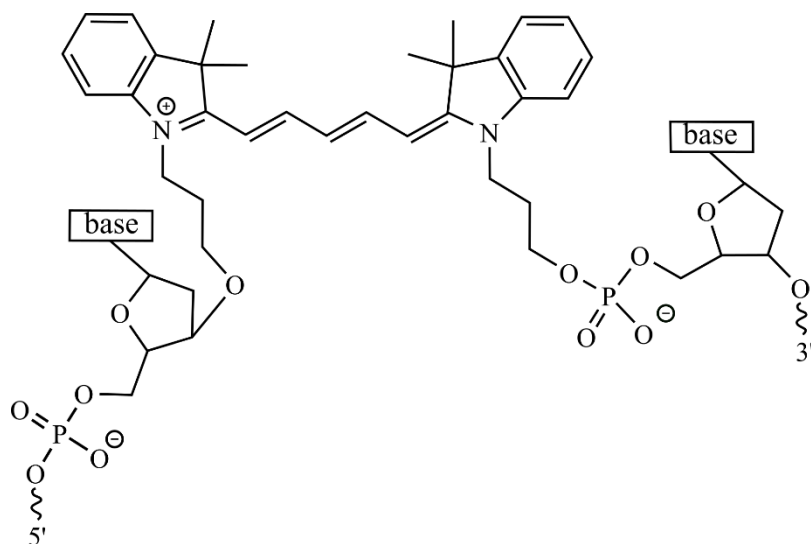
Scheme 4.1. Cy5, a common fluorescence labeling dye composed of a pentamethine bridge flanked by two dimethyl indolenine rings, shown tethered to an oligonucleotide backbone via two propyl linkers covalently bonded to the deoxyribose and phosphate groups of the 5' and 3' ends of the sequence, respectively.

In this work, we use a combination of femtosecond transient absorption (TA) spectroscopy and global target analysis (GTA) to examine the excited-state dynamics of a series of DNA-templated Cy5 aggregates. First, we examine the excited-state dynamics of duplex dimer and Holliday-junction tetramer structures formed using two distinct oligonucleotide strands. Next, we examine the excited-state dynamics of two different dimers, a trimer, and a tetramer using DNA Holliday junctions formed from four distinct oligonucleotide strands. In all cases, considerable reduction of the excited-state lifetime in the aggregates compared with the monomer is observed and, in addition, considerable variability is observed in the lifetimes of the aggregate structures. Pump-wavelength dependent femtosecond TA measurements indicate that certain solutions exhibit an appreciable extent of heterogeneity, particularly with respect to aggregate structures. We proceed to discuss the structural factors influencing nonradiative decay in the DNA-templated aggregates, such as exciton delocalization and dye separation. Finally, we

discuss factors contributing to the variability of the excited-state lifetimes, including potential sources of heterogeneity.

4.3 Methods

DNA-Dye Construct Preparation. Oligonucleotides labeled with Cy5 via dual phosphoramidite linkers and purified by dual high-performance liquid chromatography were obtained as lyophilized powders from Integrated DNA Technologies (IDT; Coralville, IA). Unlabeled oligonucleotides purified by desalting were also obtained from IDT. Stock solutions of labeled and unlabeled oligonucleotides were prepared at a concentration of 100 µM by hydrating with water obtained from a Barnstead Nanopure water purification system (ThermoFisher Scientific, Waltham, MA). Stock oligonucleotide solution concentrations were determined according to Beer's law using the extinction coefficient provided by the vendor (at 260 nm) and the absorbance measured at 260 nm via a NanoDrop One UV-Vis spectrophotometer (ThermoFisher Scientific, Waltham, MA), which reports absorbance scaled to a path length of 1 cm. Solutions of DNA and DNA-dye constructs (i.e., labeled and unlabeled DNA duplexes and HJs) were prepared by combining equimolar amounts of stock oligonucleotide solutions with an aqueous TAE buffer solution prepared at ten times its typical concentration, i.e., 10×. $MgCl_2$ was added for selected DNA and DNA-dye constructs. The volumes of the stock oligonucleotide solutions, TAE buffer solution, and water were chosen so that the final concentration of the DNA or DNA-dye construct was in the range of 1-5 µM. The volumes were also chosen to achieve a final buffer concentration of 1× TAE and the final desired concentration of $MgCl_2$, which ranged from 0 – 100 mM. The resulting solutions were vortex mixed for 30 seconds, then allowed to sit overnight in a dark container at room temperature.

Steady-State Absorption Spectroscopy.

Steady-state spectra were collected using either a Cary 60 or 5000 UV-Vis spectrophotometer (Agilent Technologies, Santa Clara, CA). Spectra were typically collected from 200 to 800 nm in 1 nm steps. Solutions were contained in a 2 mm quartz cuvette (Starna Cells, Atascadero, CA) and had a maximum absorbance of ca. 0.3 in the range of 500 – 700 nm.

Femtosecond Transient Absorption Spectroscopy.

All TA spectra were collected using a custom-built TA spectrometer. At the head of the system, a Ti:sapphire-based laser oscillator (Coherent, Santa Clara, CA) produces a train of femtosecond pulses at a rate of 80 MHz, centered at ~800 nm and with an energy of ~4 nJ/pulse. The output of the laser oscillator seeds a Ti:sapphire-based regenerative amplifier (Coherent, Santa Clara, CA), which produces an amplified train of ~40 fs pulses at a rate of 1 kHz, centered at ~800 nm and with an energy of ~3 mJ/pulse. The output of the laser amplifier was used to drive an optical parametric amplifier (Coherent, Santa Clara, CA) to generate the pump beam, which was varied from ~560 to ~700 nm. The probe beam was generated by focusing a small fraction of the laser amplifier output onto a 2 mm thick sapphire window (Newlight Photonics, Toronto, ON, Canada), which produced a white-light continuum spanning ~420 to 750 nm (**Section S1**). The pump and probe beams were spatially overlapped at the sample position and their relative time delay was controlled by varying the pump beam path distance via a mechanical delay stage (Aerotech, Pittsburgh, PA). TA spectra were collected by routing the probe beam to a spectrograph, which included a monochromator and an sCMOS array detector (Andor, Belfast, Northern Ireland). For all measurements, the relative orientation of the linearly polarized pump and

probe beams was set to 55°, i.e., the so-called "magic" angle. Pump and probe beam diameters were estimated to be ca. 215 and 140 µm, respectively, by measuring the beam power in the presence and absence of a 50 µm diameter high-energy pinhole (Newport, Santa Clara, CA) situated in the focal plane of the probe beam. Pump fluences ranged from 13 – 40 µJ/cm^2 and are reported where appropriate. Solutions were contained in a 2 mm quartz cuvette (Starna Cells, Atascadero, CA) and stirred with magnetic stirrer bars (Starna Cells, Atascadero, CA) rotated over the course of the measurement with a magnetic stirring apparatus (Ultrafast Systems, Sarasota, FL). The pump pulse duration was determined to be ~180 fs by performing an autocorrelation on a 2 mm quartz cuvette filled with distilled water situated at the sample position (**Section S2**).

Global and Target Analysis of Transient Absorption.

Prior to GTA, the femtosecond TA data were corrected for chirp in the probe continuum. The chirp in the probe continuum was modeled with a polynomial function and the respective wavelength-dependent time offset correction factors were subtracted from the data. GTA of the corrected data was facilitated with the Java-based graphical user interface Glotaran[60] and was performed using the TIMP statistical package, which is part of the R computational platform.

<u>Steady-State Optical Modeling.</u>

The optical properties of selected DNA-dye constructs were modeled using in-house software based on the Kühn-Renger-May method (version 13.7).[47,49,58] The software simultaneously fits absorbance and circular dichroism data by constructing and diagonalizing a Holstein Hamiltonian[19] that includes a single dominant vibronic mode. The fitting procedure begins with a user input dye configuration and performs a stochastic search by randomly perturbing the dye configuration and checking the fit quality. The output of the optical modeling is a set of vectors representing the spatial orientation and separation of the TDMs of the dyes in the aggregate. In the case of Cy5, the TDM is taken to be along the long axis of the pentamethine bridge (**Scheme 4.1**).

4.4 Results

<u>Construct Preparation and Steady-State Optical Characterization.</u>

To examine the impact of DNA-dye configuration on the excited-state dynamics of Cy5 aggregates, we chose to study the two types of DNA-Cy5 constructs presented in **Figure 4.1**.
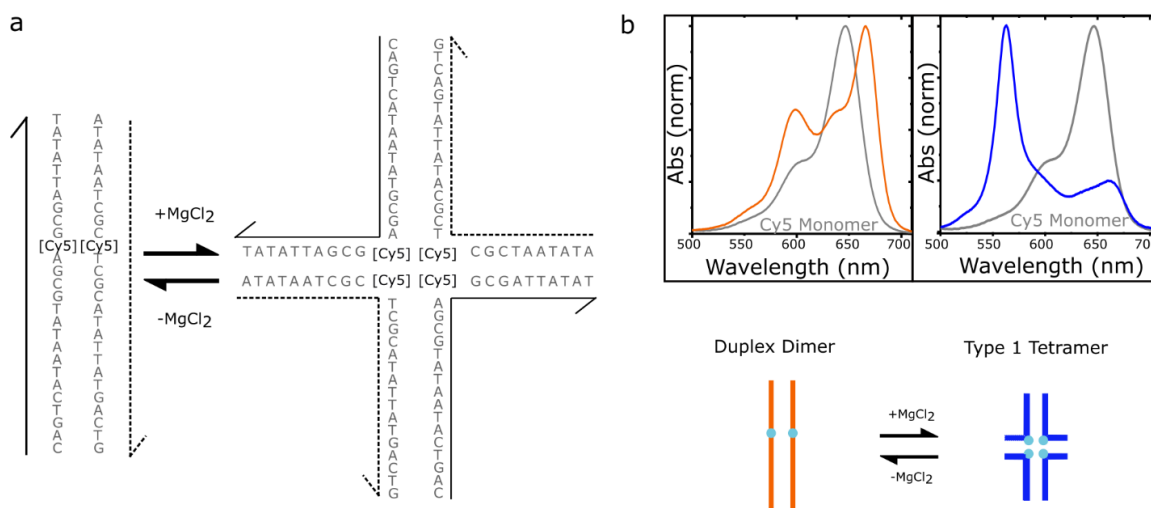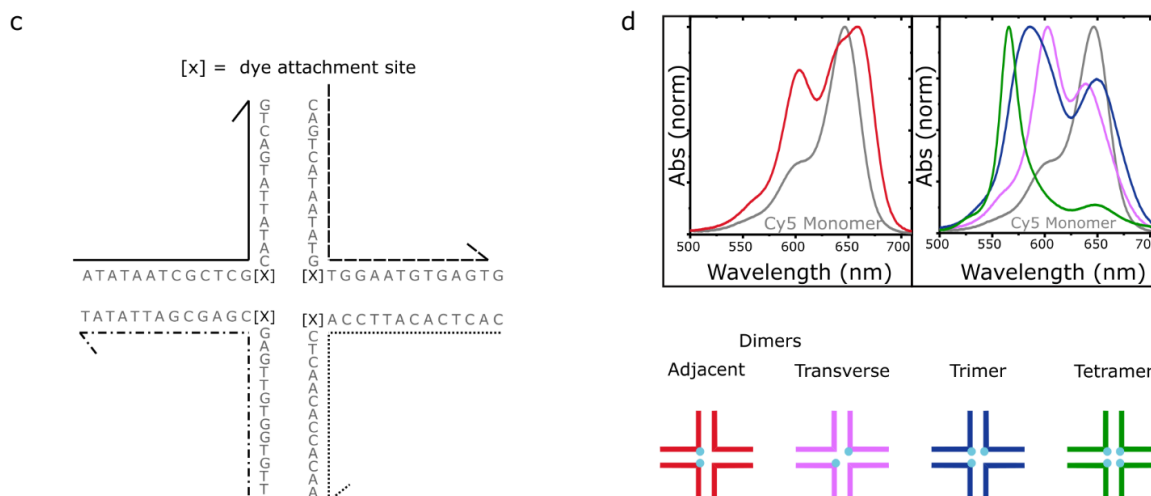
Figure 4.1. **(a) Type 1 DNA-dye constructs formed by mixing two complementary Cy5-labeled oligonucleotide strands in an aqueous buffer solution in the absence (left) and presence (right) of added MgCl$_2$. Duplex DNA is the primary nanostructure in the absence of added MgCl$_2$, whereas DNA Holliday junctions are formed when MgCl$_2$ is added. There is one Cy5 dye per strand, and so the duplex and Holliday junction template the aggregation of a Cy5 dimer and tetramer, respectively. (b) Normalized absorption spectra of the duplex dimer and "mobile" Holliday junction tetramer. The lower part of panel b depicts schematic illustrations of the duplex dimer and Holliday junction tetramer, where cyan circles indicate the approximate location of Cy5 dyes. (c) Type 2 DNA-dye constructs that form by mixing four mutually complementary oligonucleotide strands in an aqueous buffer solution with MgCl$_2$ added. The solutions primarily consist of "immobile" Holliday junctions. Cy5**

84

dyes are covalently tethered to two, three, or four positions within the Holliday junction. (d) Normalized absorption spectra of the two dimer species (adjacent and transverse), trimer, and tetramer formed via "immobile" Holliday junctions. The lower part of panel d depicts schematic illustrations of the dimer, trimer, and tetramer structures, where cyan circles indicate the approximate location of Cy5 dyes. The schematic depictions of the dye labeled duplex and Holliday junction structures are not meant to imply specific geometric configurations of the dye or DNA backbone.

Cannon *et al.* showed that a range of DNA-Cy5 dye aggregate nanostructures are possible from a basis set of either two or four oligonucleotide strands.[47,49] **Figure 4.1a** shows the two DNA-dye aggregate nanostructures resulting from a basis set of two oligonucleotide strands. In this case, which we label the "type 1" set of DNA-dye constructs, it is possible to form a Cy5 dimer via duplex DNA along with a Cy5 tetramer via a DNA Holliday junction. Specifically, Cannon *et al.* showed that, in the absence of added $MgCl_2$, duplex DNA was the primary DNA nanostructure in the solution. However, through gel electrophoresis studies, Cannon et al. showed that adding $MgCl_2$ to the solution promoted the association of four strands to form a "mobile" DNA Holliday junction tetramer. Furthermore, the Holliday junction is only observed when the two basis strands are labeled with Cy5, indicating that the DNA-dye construct may be additionally stabilized by the mutual attraction of the four dyes. Since two and four dyes are aggregated via DNA duplexes and Holliday junctions, we label these the duplex dimer and type 1 tetramer structures, respectively. In the case of the duplex dimer and type 1 tetramer structures, the excitonically coupled absorption spectra exhibit redshifted and blueshifted spectral features consistent with J- and H-aggregation, respectively (**Figure 4.1b**). For the remainder of the paper, we refer to the solutions where primarily duplex dimers and Holliday junction tetramers are present as the no-salt type 1 and high-salt type 1 solutions, respectively.

Expanding the basis set to four oligonucleotides provides access to an even larger number of DNA-dye aggregate configurations (**Figure 4.1c**). Here, a single "immobile" DNA Holliday junction is targeted. In this case, the Holliday junction is targeted to minimize the possibility that lower-order DNA nanostructures, such as duplexes, might form and contribute to heterogeneity in the solution. We label these aggregates as the "type 2" set of DNA-dye constructs. In the type 2 set of DNA-dye constructs, the number of dyes in the aggregate can be varied between two, three, and four. Thus, the effect of the extent of exciton delocalization on excited-state lifetimes can be examined. Furthermore, two different dimer configurations are possible—an adjacent and transverse dimer. Cannon *et al.* showed that the adjacent dimer exhibited optical signatures of a J-aggregate packing arrangement, while the transverse dimer, trimer, and tetramer all exhibited signatures of H-aggregate packing.[49] These signatures are evident in the absorption spectra shown in **Figure 4.1d**. Thus, the so-called type 2 set of DNA nanostructures provide access to a range of configurations, including different possible extents of exciton delocalization, proximal positions of the dyes, and packing arrangements.

Excited-State Dynamics of Type 1 DNA-Cy5 Constructs.

We begin by examining the excited-state dynamics of the no-salt type 1 solution, which is composed largely of duplex dimer structures. We performed spectrally-resolved femtosecond TA measurements exciting the solutions at specific wavelengths using a narrowband pump and tracking the ensuing excited-state dynamics across the visible spectrum using a continuum probe (see e.g. **Section S.1**). Here, we excite the solution at 675 nm (**Figure 4.2a**) which was selected to coincide with the main absorption band at ~666 nm. The resulting TA surface for the no-salt type 1 solution shown in **Figure 4.2a**

plots the evolution of the TA spectrum. Several positive and negative TA signals (plotted in units of $\Delta T/T$) are evident, all of which decay on a rapid ca. 10 ps timescale. **Figure 4.2b** displays spectral slices that more clearly highlight the rapidly decaying positive and negative signals. At the earliest time delay shown of ~1 ps, two prominent positive TA signals are apparent at 603 and 672 nm that generally align with the peaks appearing at ca. 600 and 666 nm in the steady-state absorption spectrum. As such, we assign these positive TA signals to ground-state bleach (GSB) features of the duplex dimer structure. In addition, several negative TA signals are observed at ca. 445, 493, and 638 nm, which we assign to excited-state absorption (ESA) features. At the longest time delay shown of ~150 ps, all the signals have decayed except for a weak positive signal at ca. 655 nm, which we assign to the GSB feature associated with a small subpopulation of monomers.
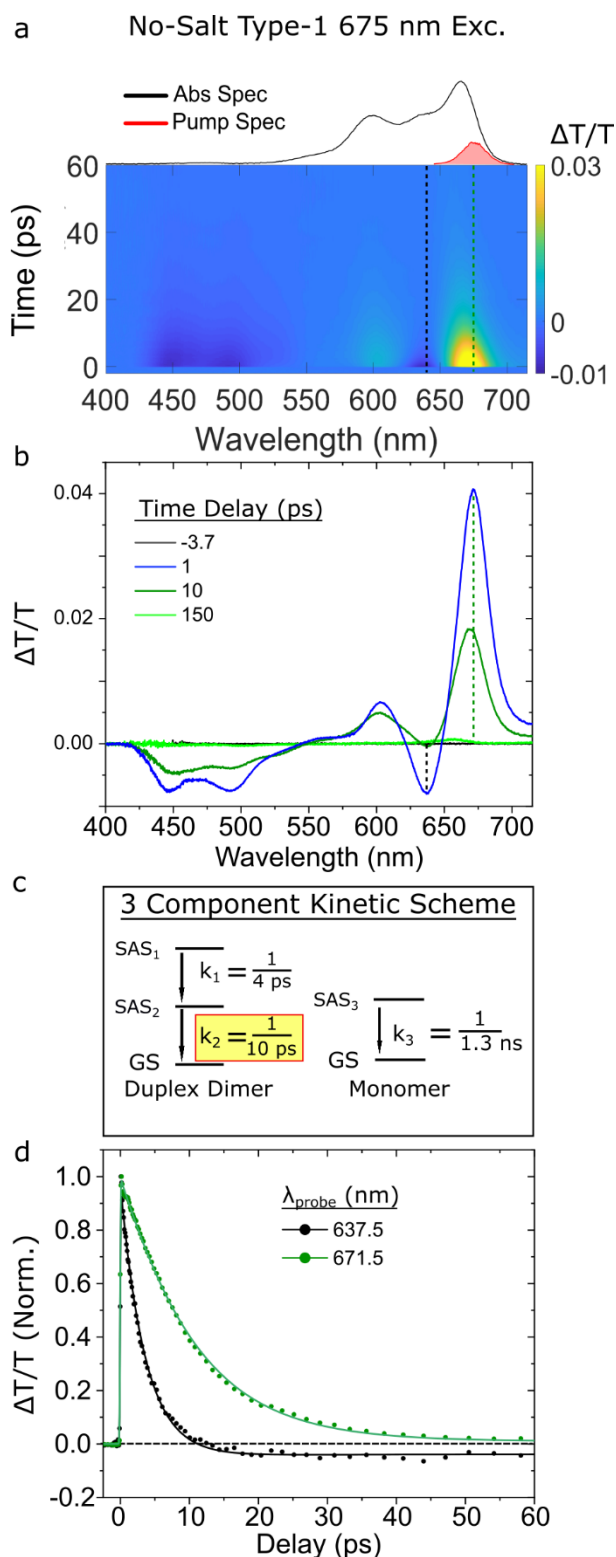
Figure 4.2. Femtosecond TA spectrum of the no-salt type 1 solution, predominantly composed of duplex J-dimer structures, collected with a pump wavelength of 675 nm at a fluence of 18 μJ/cm². (a) Surface plot. The black and green vertical dashed lines correspond to individual kinetics traces plotted in panel d. The

absorption and pump spectra are plotted above the TA surface plot. The scale bar is indicated beside the plot. (b) Selected TA spectra. Time delays are indicated in the legend. (c) Kinetic scheme used to model the TA spectrum via GTA. Rate constants (expressed as inverse time constants) associated with conversion between different components exhibiting distinct species-associated spectra (SAS) are shown. The rate constant associated with the excited-state lifetime of the duplex dimer structure is highlighted in yellow. (d) Selected TA kinetics at probe wavelengths of 638 and 672 nm are shown, with the kinetics normalized to their maximum amplitude near the time origin of the measurement. Data are shown as circles, while fits are shown as solid lines.

To further investigate the excited-state dynamics of the duplex dimer structure, we performed a GTA of the TA of the no-salt type 1 solution. The kinetic scheme used to model the data is shown in **Figure 4.2c**. A more detailed mathematical and physical justification of the three-component kinetic scheme, including the species-associated spectra (SAS) for each component, can be found in **Section S3** of the Supporting Information. The kinetic scheme includes two components associated with the duplex dimer structure and a third component to account for a small subpopulation of monomers. With the exception of the small subpopulation of monomers, the no-salt type 1 solution is not expected to exhibit significant heterogeneity, particularly at the 675 nm excitation wavelength chosen for the TA measurement.[25] Thus, we conclude that the two components in the kinetic scheme assigned to the duplex dimer structure decay in sequence. **Figure 4.2d** displays normalized kinetics traces and associated fits at probe wavelengths of 672 and 638 nm, which correspond to the decay of the most prominent GSB and ESA features, respectively, of the duplex dimer (see e.g. **Figure 4.2a**). The GTA returned k_1 and k_2 rate constants, associated with the sequential decay of the duplex dimer, of ca. $1/3.6$ ps^{-1} and $1/10$ ps^{-1}, respectively, while the third rate constant, k_3, associated with monomers, was fixed to the excited-state decay rate of the monomer, i.e., $1/1.3$ ns^{-1} (**Section S4**). **Figure 4.2d** shows that the ESA feature exhibits a decay component on a timescale much faster

than the GSB feature, which the GTA derives to be 4 ps. In contrast, the GTA derives a time constant of 10 ps for the more slowly decaying GSB feature. The latter result is in excellent agreement with the 11 ps lifetime previously measured using a degenerate, narrowband pump-probe configuration.[25]

Next, we examined the excited-state dynamics of the high-salt type 1 solution, primarily composed of type 1 tetramer structures. In order to preferentially excite the type 1 tetramer structures, i.e., to optically bias a population of excited states specifically associated with these structures, the solution was pumped at 555 nm, near where the type 1 tetramer structures absorb the strongest. The resulting TA surface plot is shown below the steady-state absorption spectrum in **Figure 4.3a**. A single positive TA signal is apparent in the surface plot at ca. 561 nm, which is situated between two negative TA signals, one at shorter wavelengths that is weak and broad, and another at longer wavelength that is more intense and narrow. Notably, compared with the duplex dimer structure, the signal persists on a longer several 10s of ps timescale. **Figure 4.3b** shows selected TA spectra taken from the TA surface plot. At early time delay (1 ps), an intense and narrow positive TA band peaking at ca. 561 nm is observed, which aligns with the main absorption band of the high-salt type 1 solution. Given that the high-salt type 1 solution is composed largely of type 1 tetramer structures, we assign the positive TA band to the GSB of the type 1 tetramer structures. As noted above, the GSB of the type 1 tetramer structure is situated between two negative TA signals. **Figure 4.3b** shows that these signals, which we assign to ESA features, peak at ca. 467 and 608 nm. Notably, the 1 ps TA spectrum is essentially featureless between ca. 650 - 715 nm. This observation indicates that duplex dimer structures, which exhibit a pronounced GSB feature at ca. 671 nm (**Figure 4.2b**), contribute

negligibly, if at all, to the observed TA. At intermediate time delays (10-30 ps), the TA spectrum appears to decay uniformly. This result is consistent with the interpretation that only a single aggregate structure, the type 1 tetramer, contributes to the TA signal. At long time delays (150 ps), the TA signal has completely recovered to baseline and no monomer signal is evident. Thus, the selected TA spectra indicate that the 555 nm pump preferentially excites type 1 tetramer structures in the high-salt type 1 solution.

a   High-salt Type-1 555 nm Exc.

b

c   2 Component Kinetic Scheme

$$SAS_1$$
$$k_1 = \frac{1}{2.3} \text{ ps}$$
$$SAS_2$$
$$k_2 = \frac{1}{30} \text{ ps}$$
$$GS$$

Type 1 Tetramer

d

e   High-salt Type-1 660 nm Exc.

f

g   5 Component Kinetic Scheme
Major Populations

$$SAS_1$$
$$k_1 = \frac{1}{4 \text{ ps}}$$
$$SAS_2$$
$$k_2 = \frac{1}{10 \text{ ps}}$$ $$SAS_3$$ $$k_3 = \frac{1}{32 \text{ ps}}$$
$$GS$$ $$GS$$
Duplex Dimer   Type 1 Tetramer

Minor Populations

$$SAS_4$$ $$SAS_5$$
$$k_4 \sim \frac{1}{160 \text{ ps}}$$ $$k_5 = \frac{1}{1.3 \text{ ns}}$$
$$GS$$ $$GS$$
Adj Dimer   Monomer

h
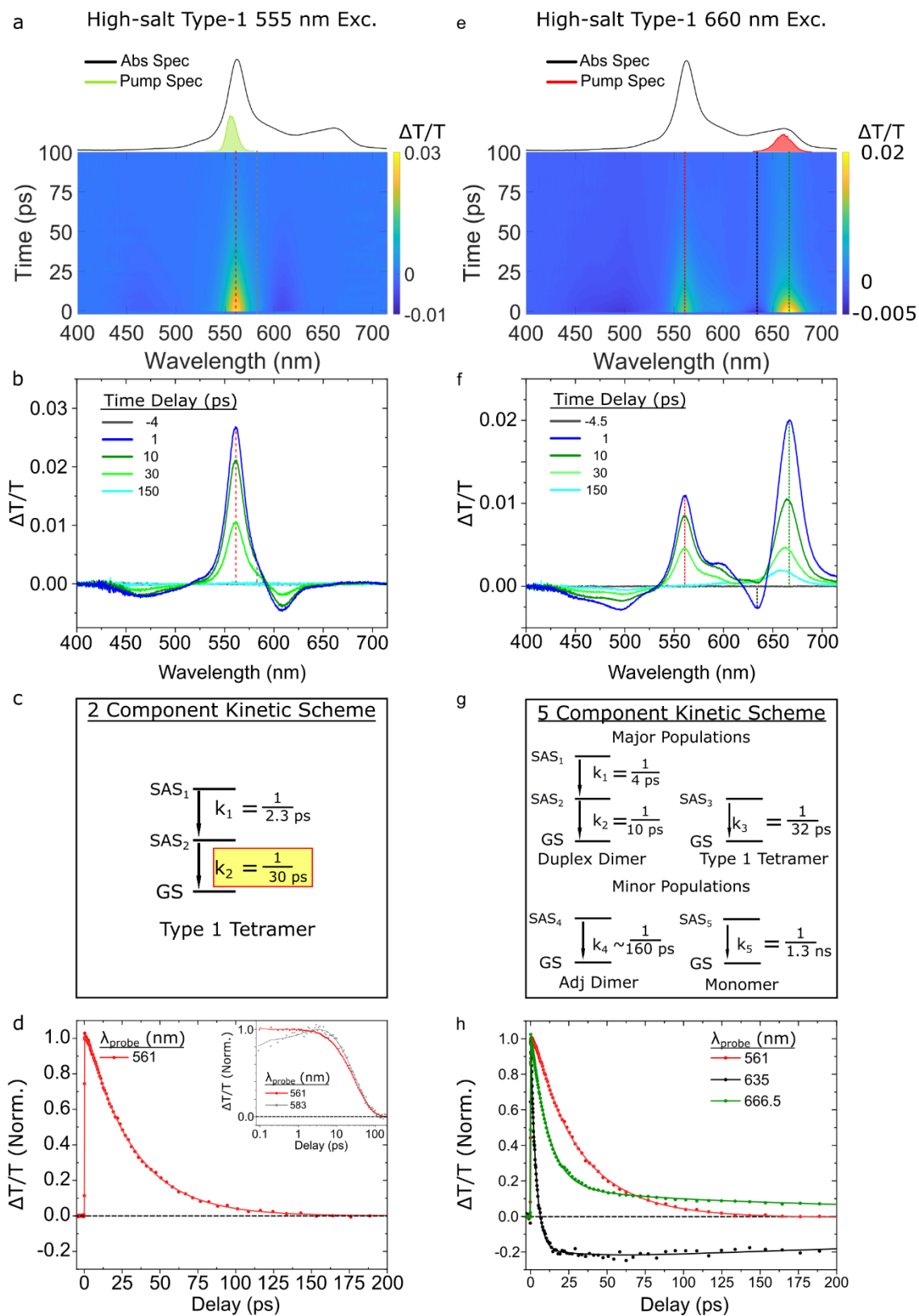
Figure 4.3. **Femtosecond TA spectra of the high-salt type 1 solution, primarily composed of type 1 tetramer structures, collected with pump wavelengths of 555 and 660 nm at pump fluences of 26 and 18 μJ/cm², respectively. (a, e) Surface plots. Vertical dashed lines indicate kinetics traces that are plotted in panels d and h, respectively. (b, f) Selected TA spectra for each pump wavelength. Time delays are indicated in the legend. (c, g) Kinetic schemes used for GTA. The rate constants associated with specific components are reported as inverse time constants. In the case of panel g, all rate constants were fixed except for the rate constant associated with the fourth component (or SAS₄). (d, h) Selected TA kinetics, normalized to their maximum amplitude near the time origin of the measurement. Data are shown as circles, while fits are shown as solid lines. Panel d displays TA kinetics at a probe wavelength of 561 nm, which corresponds to the GSB of the type 1 tetramer structure; the inset of panel d displays TA kinetics taken at probe wavelengths of 561 and 583 nm corresponding to the GSB and ESA, respectively, of the type 1 tetramer structure. Panel h displays TA kinetics at a probe wavelength of 561 nm, which corresponds primarily to the GSB of the type 1 tetramer structure, and at probe wavelengths of 635 and 667 nm, which correspond primarily to the ESA and GSB, respectively, of the duplex dimer structure.**

To further investigate the excited-state dynamics of the type 1 tetramer structures, we performed a GTA of the TA of the high-salt type 1 solution excited at 555 nm. The two-component kinetic scheme used to model the data is shown in **Figure 4.3c**. A more detailed mathematical and physical justification of the two-component kinetic scheme, including the SAS for each component, can be found in **Section S5**. **Figure 4.3d** displays a normalized kinetics trace at 561 nm and an overlay of normalized kinetics traces at 561 and 583 nm are shown in the inset. The kinetics traces are largely similar, with slight deviations evident on the sub-10-ps timescale. Two rate constants k_1 and k_2 with values of $1/2.3$ ps^{-1} and $1/30$ ps^{-1}, respectively, are derived from the GTA. While k_1 could have several physical origins, including solvent dynamics and vibrational cooling, the value of ca. $1/30$ ps^{-1} is clearly associated with the full recovery of the GSB and decay of the ESA features. As such, we assign k_2 to the excited-state decay rate of the type 1 tetramer structures. The value of ca. 30 ps derived by the GTA is in good agreement with the lifetime of ca. 35 ps previously measured via degenerate, narrowband pump-probe.[25]

Having measured the 'pure' spectrotemporal signals—that is, the spectra and rate constants—associated with the duplex dimer and type 1 tetramer structures, we next proceeded to simultaneously excite both populations in order to produce a heterogeneous TA dataset. This was accomplished by exciting the high-salt type 1 solution at 660 nm, where both the duplex dimer and type 1 tetramer exhibit appreciable absorption (**Figure 4.1b**). As expected, both the TA surface plot and selected TA spectra appear to be a sum of the signals associated with the duplex dimer and type 1 tetramer structures (**Figure 4.3e,f**). This is perhaps most visible in the 1 ps TA spectrum, which exhibits positive and negative TA signals at ca. 667 and 635 nm, respectively, clearly reminiscent of the GSB and ESA features associated with the duplex dimer structure. As was observed in the low-salt type 1 solution excited at 675 nm, the ESA feature peaking at ca. 635 nm decays considerably by ca. 10 ps. In addition, a prominent positive TA feature is observed at ca. 561 nm, which is reminiscent of the GSB feature of the type 1 tetramer structure. Consistent with our expectations based on the ca. 10 and 30 ps lifetimes measured for the duplex dimer and type 1 tetramer structures, respectively, the positive TA signal at 667 nm decays faster than the positive TA signal at 561 nm. Clearly, the positive TA signals at 667 and 561 nm are attributable to the GSB features of the duplex dimer and type 1 tetramer structures, respectively. Thus, we have successfully achieved a heterogeneous TA dataset where two aggregate structures are simultaneously excited.

To test the ability of GTA to decompose a TA dataset into 'pure' spectra and rate constants of the constituent components, we then performed a GTA on the heterogeneous TA dataset including signatures of both duplex dimers and type 1 tetramers. A five-component kinetic scheme with both sequential and parallel pathways, shown in **Figure**

4.3g, was used to model the data. A more detailed mathematical and physical justification of the five-component kinetic scheme, including the SAS for each component, can be found in **Section S.6**. An essential aspect of the model is that it includes multiple parallel decay pathways to account for the heterogeneous nature of the solution and corresponding TA dataset. Guided by the rate constants measured for the duplex dimer and type 1 tetramer detailed above, k_1-k_3 and k_5 attributable to the duplex dimer, type 1 tetramer, and monomer were fixed to the values of $k_1=1/4$ ps^{-1}, $k_2=1/10$ ps^{-1}, $k_3=1/32$ ps^{-1}, and $k_5=1/1.3$ ns^{-1}, respectively. Only one component was used for the type 1 tetramer due to the small change in amplitude between its two components (see e.g. **Figure 4.3c** and **Section 4.8.5**). An additional component, not associated with any of the structures discussed thus far, was revealed by the GTA. The rate constant associated with this component, k_4, was derived to be $1/160$ ps^{-1}. Additional details about this component, including a tentative physical assignment, can be found below. **Figure 4.3h** displays normalized kinetics traces at probe wavelengths of 561, 635, and 667 nm, which correspond primarily to the GSB of the type 1 tetramer, the ESA of the duplex dimer, and the GSB of the duplex dimer, respectively. Remarkably, the kinetics traces displayed in **Figure 4.3h** appear largely to represent a linear combination of the kinetics traces displayed in **Figures 4.2d** and **4.3d**, i.e., associated with the duplex dimer and type 1 tetramer structures, respectively, with the exception of a more pronounced long-lived signal readily attributable to a larger fraction of monomers photoexcited in the high-salt type 2 solution. Fits of the kinetics traces, derived from the five-component GTA, are also shown in **Figure 4.3h**.

We next proceed to compare the 'pure' SAS derived for the duplex dimer and type 1 tetramer with the corresponding SAS derived from the heterogeneous TA dataset. **Figure**

4.4 displays the 'pure' SAS derived for the duplex dimer and type 1 tetramer along with the corresponding SAS derived from the heterogeneous TA dataset. The five-component kinetic scheme used to model the heterogeneous TA dataset is shown in **Figure 4.4a** above the SAS plots, with arrows pointing from each component to its corresponding SAS. To facilitate comparison, the SAS are normalized to the strongest GSB feature in each plot.
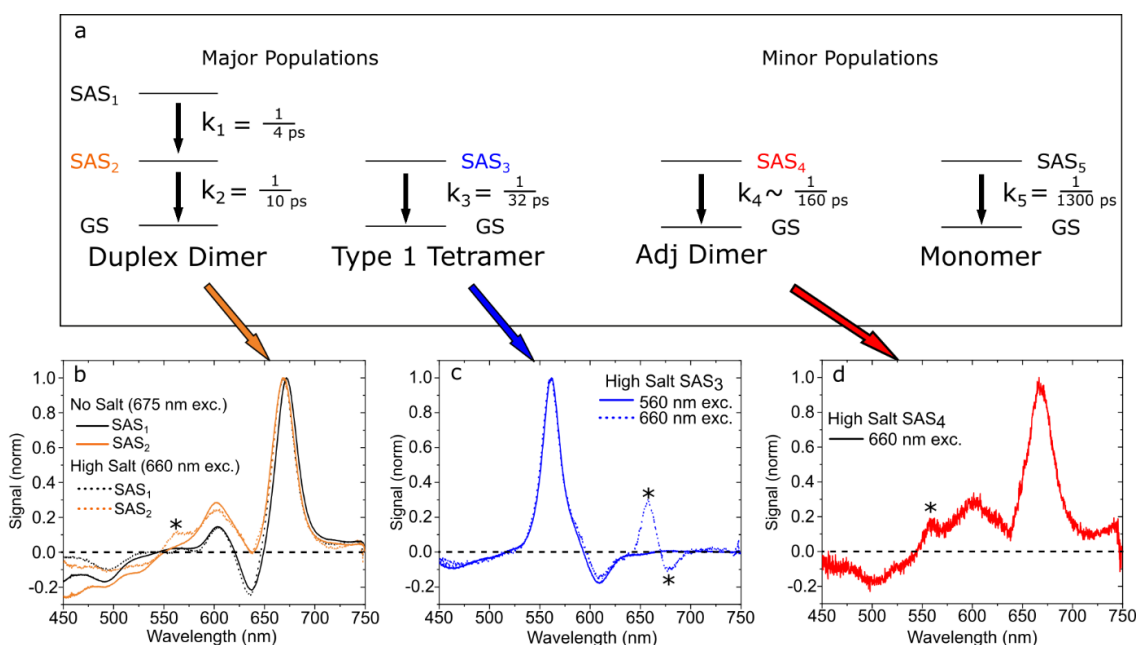
Figure 4.4. **(a) The five-component kinetic scheme used to model the high-salt type 1 solution pumped at 660 nm via a GTA (reproduced from Figure 4.3g). Four subpopulations—duplex dimers, type 1 tetramers, adjacent dimers, and monomers—decay in parallel in the model. The duplex dimers additionally exhibit a sequential decay in the model. (b) The 'pure' species associated spectra (SAS) derived for the duplex dimer from the no-salt type-1 solution pumped at 675 nm (solid lines) and SAS from the heterogeneous dataset, i.e., the high-salt type-1 solution pumped at 660 nm, attributed to the duplex dimer (dotted lines). SAS₁ are plotted in black and SAS₂ are plotted in orange. (c) The 'pure' SAS derived for the type 1 tetramer from the high-salt type-1 solution pumped at 555 nm (solid line) and the SAS from the heterogeneous dataset pumped at 660 nm, attributed to the type 1 tetramer (dotted line). (d) The SAS from the heterogeneous dataset attributed to the fourth component, which we assign to a small subpopulation of adjacent dimer-like structures present in the high-salt type-1 solution.**

The 'pure' SAS derived for the duplex dimer and type 1 tetramer are in overall good agreement with the corresponding SAS derived from the heterogeneous TA dataset. **Figure 4.4b** shows that the 'pure' SAS_1 for the duplex dimer and the corresponding SAS derived from the heterogeneous TA dataset are nearly indistinguishable. The most notable difference appears in the comparison of the 'pure' SAS_2 for the duplex dimer compared with the corresponding SAS derived from the heterogeneous TA dataset. Compared with the 'pure' SAS_2 for the duplex dimer, the SAS from the heterogeneous dataset exhibits additional positive amplitude at ca. 560 nm, marked with an asterisk. Given that the additional intensity is located in the vicinity of the main GSB for the type 1 tetramer that appears at ca. 560 nm, we attribute the additional intensity to component mixing between SAS_2 and SAS_3 due to their similar lifetimes (10 and 32 ps, respectively) and spectral overlap. **Figure 4.4c** shows that the 'pure' SAS of the type 1 tetramer and the corresponding SAS derived from the heterogeneous TA dataset are also largely indistinguishable. Here, we see overall good agreement between the SAS except for the spectral region between 650 and 700 nm, marked with two asterisks. Specifically, while the 'pure' SAS has essentially zero amplitude in this spectral region, the SAS derived from the heterogeneous dataset exhibits positive and negative TA features. We attribute these features to a combination of component mixing between SAS_3 and shorter timescale components along with dynamic pump scatter present at intermediate time delays. Lastly, **Figure 4.4d** shows the SAS associated with the fourth component in the model, which, given the similarity of its SAS and rate constant with the type 2 adjacent dimer discussed in the following section, we tentatively attribute to an additional adjacent dimer-like structure present in the high-salt type 1 solution.

Overall, the results indicate that GTA is largely able to disentangle the SAS and rate constants associated with different aggregate structures in a heterogeneous solution, and even uncover a previously unidentified aggregate structure. However, when lifetimes of species are similar and their spectra overlap, certain limitations such as component mixing can arise. These are important points of relevance to the next section.

Excited-State Dynamics of Type 2 DNA-Cy5 Constructs.

With the excited-state dynamics of the type 1 DNA-dye constructs characterized, we next proceeded to characterize the excited-state dynamics of the type 2 DNA-dye constructs.

Dimers. We begin by examining the excited-state dynamics of the transverse dimer solution pumped at 600 nm near where the Holliday junction transverse dimer structures absorb most strongly. **Figure 4.5a** displays the associated TA surface plot, which is characterized by a broad GSB band with its most intense feature peaking at ca. 600 nm and a weaker ESA band at shorter wavelength peaking at ca. 495 nm. Relatively uniform decay of these spectral bands is observed in the TA surface. **Figure 4.5b** displays selected TA spectra, which show how these features evolve over time. Comparing the TA spectrum at 1 ps in **Figure 4.5b** to the absorption spectrum of the transverse dimer, the shoulder, intense bleach, and secondary bleach at 560, 600, and 635 nm, respectively, all align well with features in the steady-state absorption spectrum. The TA spectrum at early delay times (1 ps) largely resembles the TA spectra at intermediate (100 ps) and longer delay (400 ps). However, the ratio of the intensities of primary and secondary GSB features at 600 and 635 nm, respectively, decreases at longer delay times, which we attribute to long-lived monomer contribution to the TA. The close resemblance between steady-state and transient

spectra, the relatively uniform TA decay, and the results of pump wavelength dependent TA (described below) are all consistent with the interpretation that the transverse dimer solution exhibits little aggregate structural heterogeneity and that the TA data shown in **Figure 4.5a,b** primarily represent the excited-state dynamics of transverse dimer structures.
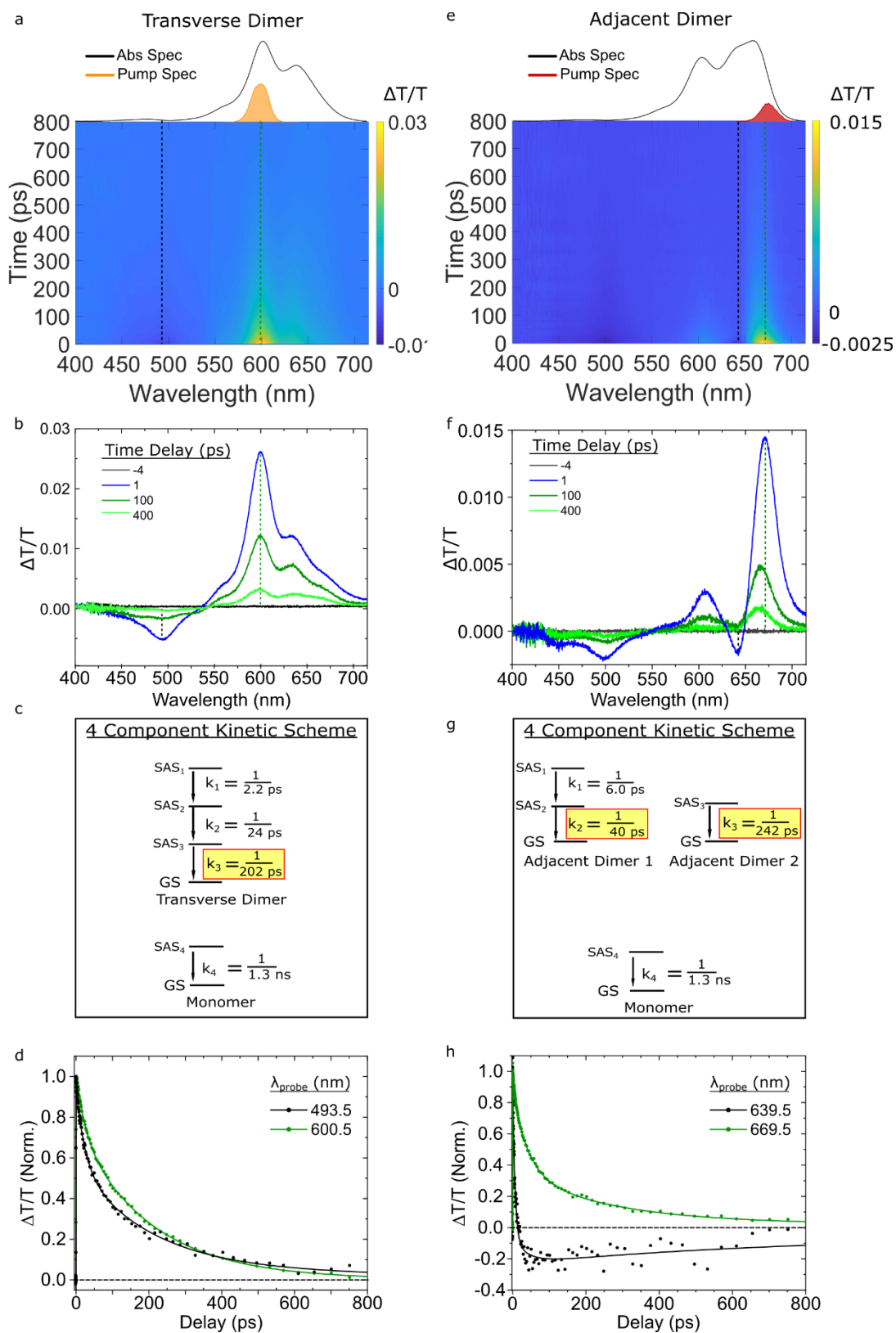
Figure 4.5. **Femtosecond TA spectra of the type 2 transverse and adjacent dimer solutions pumped at 600 and 675 nm, respectively, with pump fluences of 13 and 15**

µJ/cm², respectively. (a, e) TA surface plots of the transverse and adjacent dimer solutions. Vertical dashed lines indicate selected kinetics traces plotted in panels d and h. (b, f) Selected TA spectra. (c, g) Kinetic schemes used for GTA. The rate constants associated with specific components and SAS are reported as inverse time constants. In both analyses, the rate constant associated with the monomer was fixed to 1/1.3 ns⁻¹. (d, h) Normalized kinetics traces taken at different probe wavelengths. Data are shown as circles, while fits are shown as solid lines. In panel d, kinetics traces are displayed for probe wavelengths of 494 and 601 nm, which correspond to ESA and GSB bands, respectively. In panel h, kinetics traces are displayed for probe wavelengths of 640 and 670 nm, which correspond to ESA and overlapping ESA and GSB bands, respectively.

To extract the lifetime of the transverse dimer structure, we performed GTA on the TA data. The four-component kinetic scheme used to model the data is shown in **Figure 4.5c**. A more detailed mathematical and physical justification of the four-component kinetic scheme, including the SAS for each component, can be found in **Section S7** of the Supporting Information. The kinetic scheme includes sequential kinetics associated with the transverse dimer structures and the parallel decay of a small subpopulation of monomers. With the fourth rate constant, k_4, associated with monomer decay fixed to a value of 1/1.3 ns⁻¹ (a value used in all subsequent analyses), we derived k_1, k_2, and k_3 values of 1/2.2, 1/24, and 1/202 ps⁻¹ respectively. We attribute k_1 and k_2 to excited-state dynamics that do not result in decay to the ground state, as the primary difference between SAS are small spectral shifts and changes to ESA bands (**Section S7**). We attribute the third and final rate constant associated with the transverse dimer structures, i.e., k_3, to excited-state decay to the ground state. **Figure 4.5d** plots normalized kinetics traces at 601 and 494 nm along with fits derived from the GTA. The trace at 494 nm initially decreases in amplitude more rapidly than the trace at 601 nm, which reflects changes in excited-state electronic structure associated with the short-wavelength ESA band that take place at a rate of 1/24 ps⁻¹ (i.e., k_2). In contrast, the 601 nm trace, which follows the decay of the main GSB

feature, largely reflects the $1/202$ ps^{-1} excited-state decay rate of the transverse dimer structures.

We next characterize the excited-state dynamics of the adjacent dimer solution. Specifically, we performed TA with a 675 nm pump wavelength, which corresponds to the strongest absorption band of the adjacent dimer solution. **Figure 4.5e** displays the TA surface. Two GSB features are visible, with the strongest and weakest features at 671 and 608 nm, respectively. An ESA feature at ca. 641 nm also appears to overlap the two GSB features. A second ESA feature is observed at shorter wavelengths at 499 nm. While the 608 and 671 nm GSB features align reasonably well with the maxima observed in the steady-state absorption spectrum, overall the TA spectra do not strongly resemble the steady-state absorption spectrum, possibly indicating that the adjacent dimer solution is heterogeneous. Excitation wavelength dependent TA measurements (described below) confirm that the adjacent dimer solution may exhibit appreciable heterogeneity. Despite the heterogeneity, the redshifted absorption maximum of the adjacent dimer solution (**Figure 4.1d**) suggests that J-aggregates are the predominant species. By exciting at 675 nm, J-aggregates are thus selectively excited over H-aggregates or monomers. Selected TA spectra are plotted in **Figure 4.5f**. Similar to what we saw with the duplex dimer (**Figure 4.3a-d**), the two GSB features and the ESA at short wavelengths of the adjacent dimer appear to decay together while the ESA at ca. 641 nm exhibits a more rapid decay. For example, at 1 ps delay the amplitudes of both ESA features are similar, but after 100 ps the ESA at 635 nm has decayed appreciably such that the overall TA signal has become positive in that region while the ESA at ca. 500 nm is still negative.

To extract the lifetimes of the adjacent dimer structures, we performed a GTA according to a four-component kinetic scheme (**Figure 4.5g,h**). Additional details regarding the mathematical and physical justification of the four-component kinetic scheme are shown in **Section S8** of the Supporting Information. We attribute k_1 and k_2 with values of 1/6.0 and 1/40 ps^{-1}, respectively, to two rate constants associated with a single population of short-lived adjacent dimer structures. As we saw above for the duplex and transverse dimer structures, we assign k_1 (1/6.0 ps^{-1}) to an excited-state process that results in a change of electronic structure, as primarily a reduction in amplitude of the ESA band at 641 nm is observed between SAS$_1$ and SAS$_2$ (**Section S8**). We attribute k_2 (1/40 ps^{-1}) to the excited-state decay rate of the short-lived adjacent dimer structures. Based on the distinct spectral features of SAS$_3$ as compared with SAS$_1$ and SAS$_2$ (**Section S8**), we attribute k_3 (1/242 ps^{-1}) to the excited-state decay rate of a subpopulation of long-lived adjacent dimer structures. Thus, two different dimer structures with excited-state lifetimes of ca. 40 and 240 ps are observed in the adjacent dimer solution.

To further characterize the heterogeneity of the transverse and adjacent dimer solutions, we examined the pump-wavelength dependence of their TA. While **Figure 4.5** displays the TA of the transverse dimer solution pumped at 600 nm, **Figure 4.6** shows the TA of the transverse dimer solution pumped at 660 nm, which was chosen to selectively excite monomer and J-aggregate subpopulations. Compared with the TA surface shown in **Figure 4.5a**, the TA surface shown in **Figure 4.6a** exhibits more pronounced GSB and ESA features at ca. 660 and 500 nm, respectively. Compared with **Figure 4.5b**, less uniform decay of the TA spectra is observed in **Figure 4.6b**. For example, the GSB at 605 nm decays more rapidly than the GSB at 660 nm, and the 400 ps TA spectrum largely

resembles that of the monomer. We then pumped the adjacent dimer solution at 600 nm to potentially selectively excite H-aggregate subpopulations. Compared with **Figure 4.5e** where the solution was pumped at 675 nm, the TA surface shown in **Figure 4.6d** exhibits additional GSB and ESA features at ca. 605 and 500 nm, respectively. Selected TA spectra shown in **Figure 4.6e** indicate that the GSB features at ca. 605 and 660 nm decay nearly synchronously for approximately 100 ps, but at later times the TA spectra resemble the monomer. Thus, it is clear from the pump-wavelength dependent TA results shown in **Figures 4.5** and **4.6** that both the transverse and adjacent dimer solutions exhibit some level of heterogeneity.
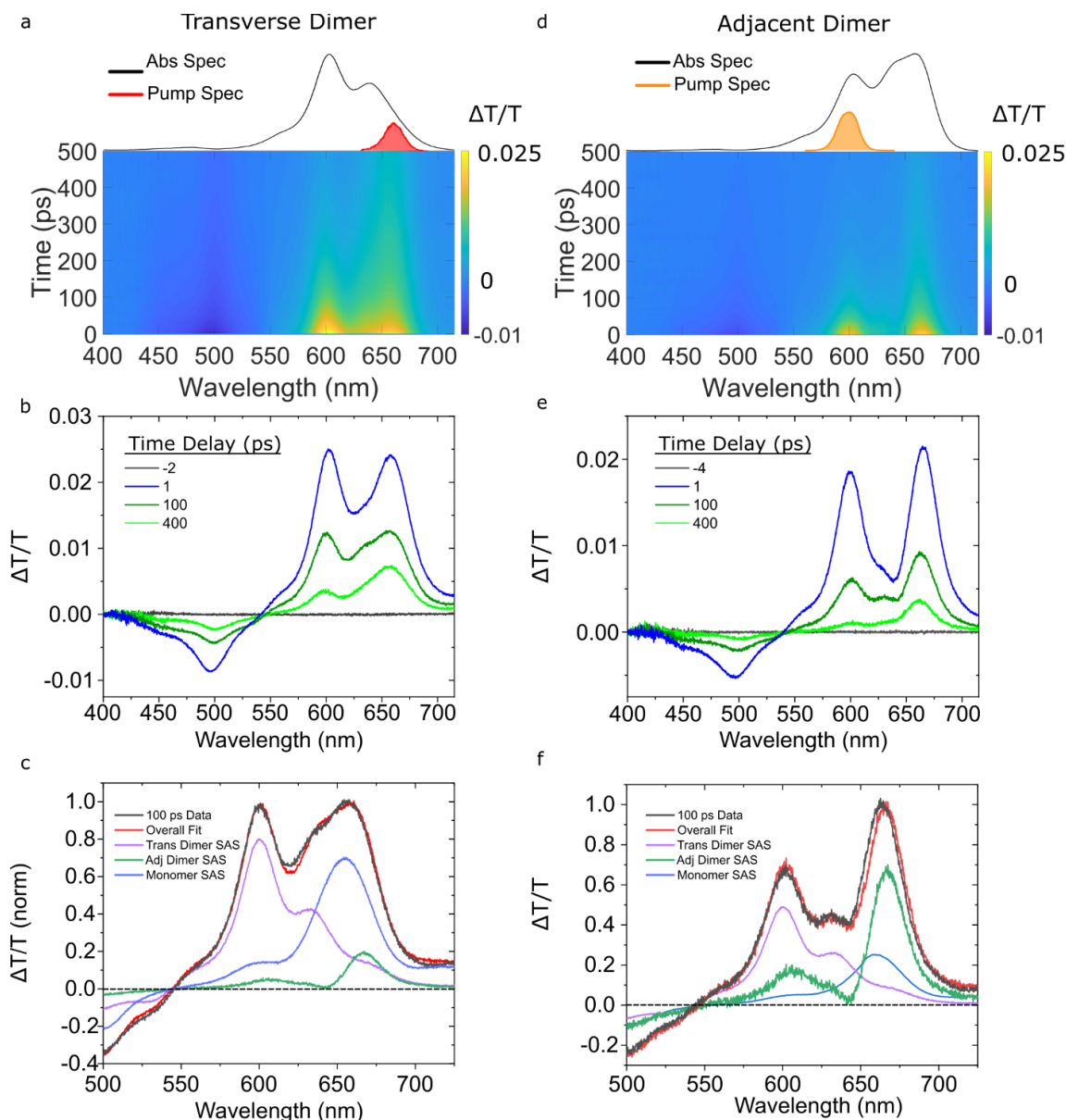
Figure 4.6. Femtosecond TA spectra of the type 2 transverse and adjacent dimer solutions pumped at 660 and 600 nm, respectively, with pump fluences of 40 and 15 $\mu J/cm^2$, respectively. (a, d) TA surface plots of the transverse and adjacent dimer solutions. (b, e) Selected TA spectra. (c, f) The 100 ps time delay TA spectra along with the scaled basis spectra used to model the data and the resultant fit. Data are shown in black; transverse dimer, adjacent dimer, and monomer basis spectra are shown in purple, green, and blue, respectively; and the fit is shown in red.

To further characterize the heterogeneity in the transverse and adjacent dimer solutions, we modeled their TA spectra using the SAS (or 'pure' spectra) of the monomers and transverse and long-lived adjacent dimer structures derived from the GTA. The

rationale for using these basis spectra is the following: (i) a small subpopulation of monomers is known to be present in the solutions[25] and (ii) the presence of long-lived adjacent dimer structures in the no-salt type 1 solution composed primarily of duplex dimer solution suggests such aggregates may be present in other solutions. **Figure 4.6c** displays the results of modeling the 100 ps timescale TA spectrum of the transverse dimer solution excited at 660 nm as a linear combination of these basis spectra. The model matches the data quite well and indicates that mostly monomers and transverse dimer structures are present in the solution, possibly also with a small amount of long-lived adjacent dimer structures. Due to the presence of a strong GSB feature at 600 nm in the TA spectrum of the adjacent dimer solution, which closely matches the primary GSB feature of the transverse dimer structures, it is sensible to conclude that transverse dimer structures may be contributing to the TA signal as well. Thus, the transverse dimer structure was included as a basis spectrum in the analysis of the TA spectrum of the adjacent dimer solution. **Figure 4.6f** displays the results of modeling the 100 ps timescale TA spectrum as a linear combination of monomer, adjacent dimer, and transverse dimer basis spectra. Again, the model matches the data well and indicates that an appreciable population of transverse dimer structures is present in the adjacent dimer solution. Based on these results, we thus conclude that with respect to aggregate structures, the transverse and adjacent dimer solutions exhibit limited and appreciable heterogeneity, respectively.

Trimer. Having characterized the excited-state dynamics of the transverse and adjacent dimer solutions, we next turn our attention to the excited-state dynamics of the trimer solution. **Figure 4.7** displays the TA of the trimer solution pumped near its most intense absorption band at 560 nm. The TA surface and selected TA spectra shown in

Figure 4.7a,b exhibit two GSB features peaking at ca. 574 and 680 nm. Two ESA features are also observed at ca. 469 and 655 nm. Between early (1 ps) and intermediate (30 ps) time delays, the maximum of the primary GSB feature shifts toward longer wavelengths and broadens slightly. At the same time, the ESA maximum at 469 nm shifts to shorter wavelengths. At longer time delays (150 ps), the primary GSB feature has redshifted further, peaking at 582 nm, while the weak ESA observed at ca. 655 nm has decayed considerably. The significant spectral shifts observed in the TA data suggest that the trimer solution may be heterogeneous and that pumping the solution at 560 nm excites multiple aggregate structures.

Figure 4.7. Femtosecond TA spectra of the type 2 trimer solution pumped at 560 nm with a pump fluence of 29 µJ/cm². **(a) TA surface plot. Vertical dashed lines**

indicate selected kinetics traces plotted in panel d. (b) Selected TA spectra. (c) Kinetic scheme used for GTA. (d) Normalized kinetics traces and their fits based on the kinetic model from panel c taken at probe wavelengths of 480 and 574 nm (black and red, respectively). Data are shown as circles, while fits are shown as solid lines. To better visualize the initial kinetics, the inset of panel d is plotted on a logarithmic time axis for kinetics traces taken at probe wavelengths of 574 and 600 nm (red and green, respectively).

To extract the lifetime of the trimer structure(s) and investigate the possibility of multiple aggregate subpopulations, we subsequently performed GTA. The four-component kinetic scheme used to model the data is shown in **Figure 4.7c**. Additional mathematical and physical justification is provided in **Section S9** of the Supporting Information. We assign the k_1 and k_2 rate constants with values of 1/2.0 and 1/26 ps^{-1}, respectively, to a single population of short-lived trimer structures. As we observed above for the dimer structures, k_1 is assigned to changes of electronic structure taking place in the excited state and k_2 is assigned to excited-state decay to the ground state. We assign the k_3 rate constant, which had a value of 1/82 ps^{-1}, to the parallel excited-state decay of a second long-lived trimer structure. As can be seen in the selected TA spectra displayed in **Figure 4.7b**, the GSB of the long-lived trimer structure is redshifted compared with that of the short-lived trimer structure. **Figure 4.7d** displays selected kinetics traces and associated fits taken at probe wavelengths of 574 and 600 nm. As can be seen more clearly in the inset, the traces at 574 and 600 nm have greater contributions from the short- and long-lived trimer structures, respectively. Thus, **Figure 4.7d** provides evidence for different relaxation rates of two trimer subpopulations, which decay with lifetimes of 26 and 82 ps.

To further characterize heterogeneity in the trimer solution, we performed pump-wavelength dependent TA. Two TA surfaces for the trimer solution excited at 560 and 660 nm are shown in **Section S10**. The two TA surfaces show very little resemblance as is

evident by the presence of drastically different GSB features. These results suggest that the trimer solution exhibits a considerable degree of heterogeneity. A Gaussian fitting analysis of the steady-state absorption spectrum of the trimer solution further supports this interpretation (**Section S11**). The analysis indicates that the absorption band at 589 nm is well described by two Gaussian lineshapes centered at 578 and 603 nm. The largest amplitude Gaussian lineshape centered at 578 nm can be explained by a predominant population of trimer structures—the most prominent GSB feature of the trimer structures appears in the vicinity of ca. 575 nm (**Figure S9.5**), which fits the expectation that the most prominent blueshifted steady-state absorption band of the trimer structure appear intermediate between that of the analogous dimer and tetramer structures with bands at ca. 603 and 563 nm, respectively (see e.g. **Figure 4.1d**). The Gaussian lineshape centered at 603 nm could arise from a subpopulation of transverse dimer structures, which, as was just noted, absorb most strongly in this spectral region. Additionally, the absorption band of the trimer solution that peaks at 650 nm is well described by two Gaussian lineshapes centered at 647 and 671 nm. The Gaussian lineshape centered at 647 nm coincides well with the monomer absorption band at ca. 650 nm. The Gaussian lineshape centered at 671 nm, on the other hand, coincides well with the most prominent GSB feature of the adjacent dimer solution that peaks at 669 nm (**Figure 4.5e,f**), which we take to be approximately representative of the most intense steady-state absorption band of the adjacent dimer structures. To further explore the heterogeneity of the trimer solution, we modeled the 100 ps TA spectra of the solution excited at 660 nm, which appears to excite most subpopulations, with similar basis spectra as used above for the transverse and adjacent dimer solutions (**Section S12**). The model fits the data well and indicates that, in addition

to two trimer structures evidenced by GTA, the trimer solution likely contains additional subpopulations of monomers, adjacent dimers, and transverse dimer-like structures, which is further consistent with the Gaussian fitting analysis.

Tetramer. Lastly, we performed TA measurements on the tetramer solution. We first determined that the solution is mostly homogeneous except for a small subpopulation of monomers (see **Section S13**). As such, exciting the solution at 560 nm, which corresponds to the most intense absorption feature in the steady-state absorption spectrum, selectively excites the tetramer structure.
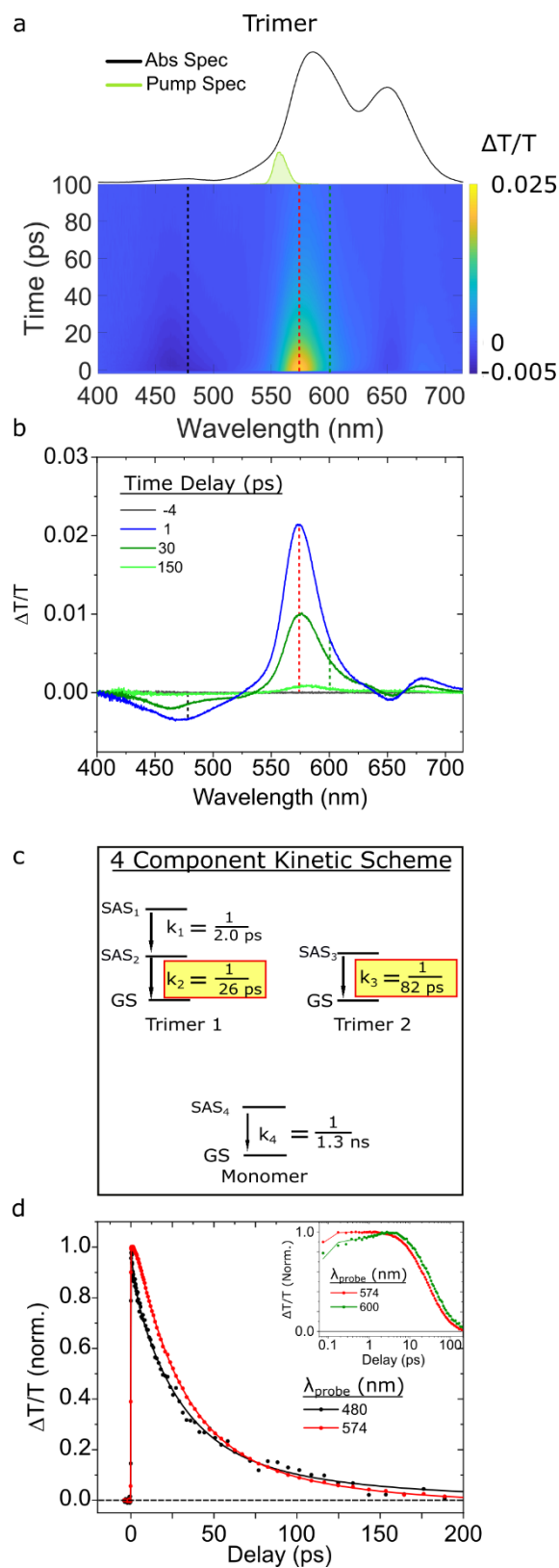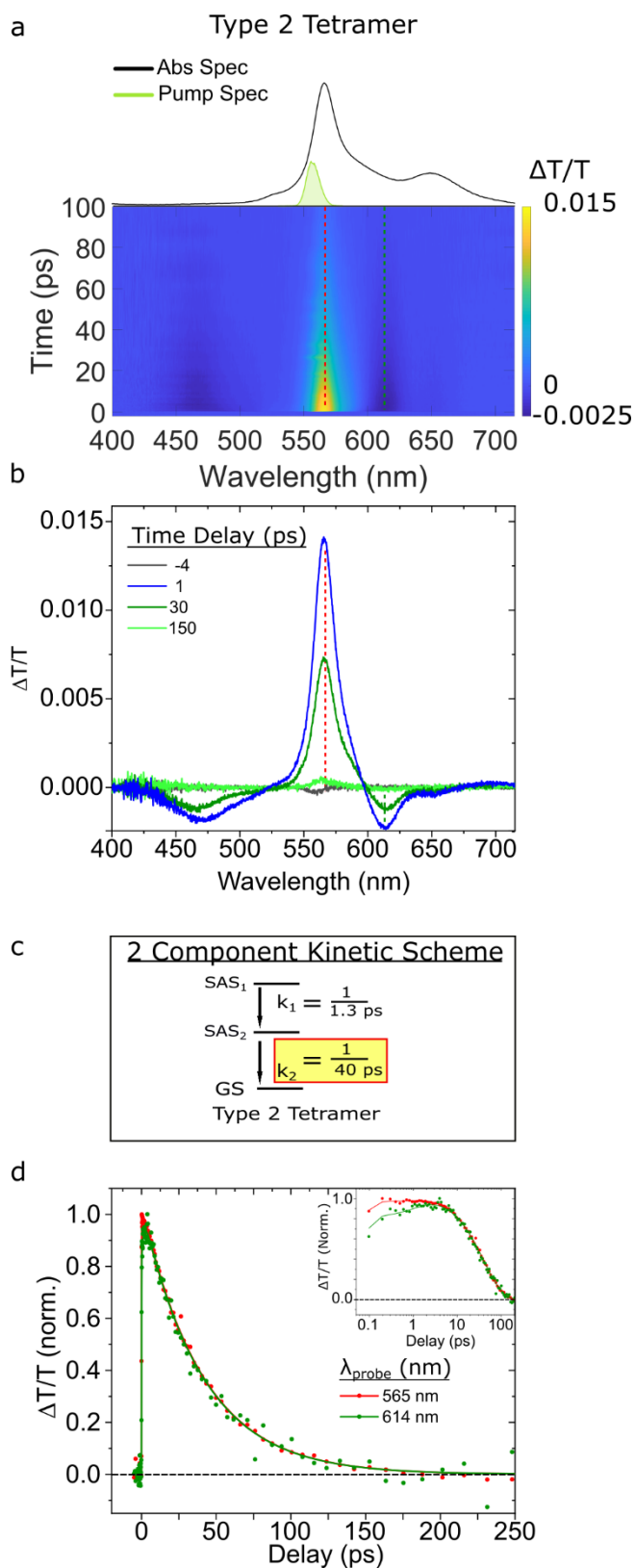
Figure 4.8. **Femtosecond TA spectra of the type 2 tetramer solution pumped at 560 nm with a pump fluence of 14 µJ/cm². (a) TA surface plots. Vertical dashed lines**

indicate selected kinetics traces plotted in panel d. (b) Selected TA spectra. (c) Kinetic scheme used for GTA. (d) Normalized selected kinetics traces and their fits based on the kinetic models from panel c taken at probe wavelengths of 565 and 614 nm (red and green, respectively). Data are shown as circles, while fits are shown as solid lines. To better visualize the initial TA response of the solution, the inset of panel d is plotted on a logarithmic time axis for the kinetics traces taken at probe wavelengths of 565 and 614 nm.

The TA surfaces and spectra for the type 2 tetramer structure (**Figure 4.8a,b**) are very similar to those collected for the type 1 tetramer structure selectively excited in the high-salt type 1 solution (**Figure 4.3a,b**). Specifically, both TA spectra exhibit an intense, narrow GSB feature peaking at ca. 565 nm, which coincides with the most intense band in the steady-state absorption spectrum. The GSB feature also straddles two less intense ESA features peaking at ca. 572 and 614 nm. To quantify the lifetime of the type 2 tetramer structure, we performed GTA according to a kinetic two-component scheme (see e.g. **Figure 4.8c** and **Section S14**). As we saw for the other structures, we assign k_1 to a change of electronic structure taking place on the excited state and k_2 to the excited-state decay of the type 2 tetramer structure. **Figure 4.8d** displays kinetics traces and fits at probe wavelengths of 565 and 614 nm. The synchronous decay of these traces to baseline is consistent with the decay of a single population. The semilogarithmic plot in the inset of **Figure 4.8d** highlights the early-time component associated with changes in electronic structure (i.e., k_1). Based on the analysis, we derived k_1 and k_2 rate constants with values of 1/1.3 and 1/40 ps^{-1}, respectively.

Overview.

In summary, we find that the excited-state lifetimes of all Cy5 aggregate configurations are significantly shortened compared with the monomer (**Table 4.1**).

Table 4.1. **Excited-State Lifetimes of type 1 and type 2 DNA-Cy5 Constructs**

Type	Construct	Lifetime (ps)
N/A	Monomer	1300
1	Duplex Dimer	10
1	Tetramer	30
2	Transverse Dimer	202
2	Short-lived Adjacent Dimer	40
2	Long-lived Adjacent Dimer	242
2	Short-lived Trimer	26
2	Long-lived Trimer	82
2	Tetramer	40

The type 1 aggregate lifetimes are some of the shortest, as the duplex dimer and type 1 tetramer exhibit lifetimes of ca. 10 and 30 ps, respectively. Conversely, the lifetimes of the type 2 aggregates exhibit a wider range of variability. Consistent with the type 1 aggregates, we found the primary adjacent dimer population, the two trimers, and the type 2 tetramer to exhibit lifetimes ranging from ca. 30 – 80 ps. In contrast, we found the transverse dimer and second adjacent dimer to exhibit considerably longer lifetimes of ca. 200 and 240 ps, respectively. In addition to measuring the lifetimes, we discovered evidence of heterogeneity in all of the aggregate solutions with the duplex dimer, transverse dimer, and type 2 tetramer solutions exhibiting relatively little heterogeneity, and the adjacent dimer and trimer and solutions exhibiting more considerable heterogeneity. In the Discussion section, we consider various mechanisms that may explain the origin of the enhanced nonradiative decay in the aggregates and the appreciable variability in their lifetimes.

4.5 Discussion

A primary goal of this study, and the focus of the first subsection, is to evaluate the relative impact of several structural factors—such as packing type, coupling strength, exciton delocalization, and dye separation—on excited-state lifetimes in DNA-templated Cy5 aggregates. In the second subsection, we proceed to discuss another factor contributing to the variability of excited-state lifetimes—heterogeneity—and the potential role of the DNA template.

Structural Factors Impacting Excited-State Lifetime.

We first consider the possible relationship between packing type and excited-state lifetime. According to Kasha's molecular exciton theory, dyes that pack as H-aggregates (J-aggregates) are expected to exhibit decreased (increased) radiative rates due to the out-of-phase (in-phase) interactions of their TDMs.[57] As a result, assuming no change in nonradiative decay rate, the H-aggregates (J-aggregates) should exhibit longer (shorter) lifetimes compared with the dye monomer. Instead, for the broad set of H- and J-aggregates examined in the present work (**Figure 4.1**), we find no such correlation between packing type and lifetime (**Table 4.1**). Specifically, for the transverse dimer, trimer, and tetramer structures, which adopted an H-aggregate packing type, we observe drastically reduced, rather than increased, lifetimes compared with the monomer. In the case of the duplex J-dimer and adjacent dimer structures, we also observe drastically reduced lifetimes compared with the monomer; lifetimes reduced to an extent inconsistent with enhanced radiative decay (i.e., superradiance) expected for a dimer aggregate.[25] These results indicate that enhanced nonradiative decay is operative in both H- and J-aggregates. Thus,

we conclude that there is no correlation between packing type and lifetime and that nonradiative decay is the primary decay pathway in the DNA-templated dye aggregates.

We next discuss the impact of coupling strength on excited-state lifetime. In a classic study, Sundström and Gillbro observed dramatically reduced lifetimes in aggregates of diethylthiadicarbocyanine iodide (DTDCI), a Cy5-like pentamethine dye.[23] These authors attributed the reduced lifetimes observed in the aggregates, including a covalently bound dimer, to accelerated nonradiative decay. They proposed that accelerated nonradiative decay may be due to more strongly coupled dyes, based on predictions using a Fermi's golden rule expression that related nonradiative decay rate to coupling strength. In the case of our aggregates, specifically the duplex dimer, transverse dimer, and type 2 tetramer, we can determine the coupling strength, which we refer to as the excitonic hopping parameter (J). By modeling the optical properties of the different aggregate structures, which is described in greater detail below and in **Section S15**, we derived J to be 48 and 73 meV for the duplex and transverse dimer, respectively. For the type 2 tetramer, we derived a maximum value of 136 meV (i.e., J_{max}), which represents J for the most strongly coupled dye pair, and an average value of 68 meV (i.e., J_{avg}), which was taken as the average of J over all dye pairs. **Table 4.2** lists these values along with their respective lifetimes.

Table 4.2.   Excitonic Hopping Parameter and Excited-State Lifetimes of Selected type 1 and type 2 DNA-Dye Constructs.

DNA-Dye Construct	J_{max} (meV)	J_{avg} (meV)	Lifetime (ps)
Duplex Dimer	48	--	11
Transverse Dimer	73	--	200
Type 2 Tetramer	136	68	40

In contrast to the expectation that stronger electronic coupling leads to accelerated nonradiative decay and reduced lifetimes, we find that the measured lifetimes are larger for those Cy5 aggregates with larger J. For example, the duplex dimer with the smallest J value exhibits the shortest lifetime. In contrast, the transverse dimer and type 2 tetramer with larger J values exhibit larger lifetimes. From this comparison, we conclude that increasing values of the excitonic hopping parameter do not result in enhanced nonradiative decay and shorter lifetimes.

The extent of exciton delocalization (i.e., the number of dyes over which an excitation is collectively shared) is another factor that may impact aggregate lifetime. Theoretical work has indicated, for example, that nonradiative decay rates can decrease considerably with increasing extent of exciton delocalization.[61,62] A central element of such a model is that larger aggregates are expected to exhibit smaller nuclear displacements upon photoexcitation, which results in reduced nonradiative decay rates. There is experimental precedent for this theoretical prediction. As noted above, Sundström and Gillbro observed drastically reduced lifetimes for aggregates of DTDCI, whose monomer lifetime is 1.5 ns. Specifically, these authors measured dimer and trimer aggregate lifetimes of 19 and 50 ps, respectively, which is consistent with the interpretation that an increasing extent of exciton delocalization may suppress nonradiative decay rates. This correlation is not just specific to DTDCI. Das and Kamat, for example, found that dimer and trimer aggregates of the dye thionine exhibited lifetimes of 40 and 60 ps, respectively, as compared with a lifetime of 420 ps for the monomer.[63] Consistent with these observations, we find that the 40 ps lifetime of the tetramer is nearly four times as large as the lifetime of the shortest-lived dimer, the duplex dimer, which had a lifetime of 10 ps (**Table 4.1**).

Additionally, we find that the shortest-lived trimer, with a lifetime of 26 ps, is intermediate between that of the duplex dimer and the tetramer. We chose to focus on the shortest-lived aggregates for this comparison because, as we propose below, we believe that an additional factor, dye separation, plays a primary role in influencing aggregate excited-state lifetime.

Finally, we consider the impact of dye separation on excited-state lifetime. This potential relationship is motivated by Liang *et al.*'s pioneering work examining lifetimes and fluorescence emission in dimers of squaraine dyes, a family of dyes structurally very similar to cyanines,[64] bridged by a varying number of methylene groups. These authors observed the shortest lifetimes and least fluorescence emission for the most closely spaced dimers and found that lifetime and fluorescence emission increased progressively as the distance between the dyes became greater. In the case of our DNA-templated Cy5 aggregates, insights into dye separation can be gleaned by simulating the optical properties of the materials, namely the absorbance and circular dichroism spectra, via an approach based on Kühn–Renger–May (KRM) theory.[47,49,58] **Figure 4.9** displays the orientation of the TDMs that result from modeling the optical properties of the duplex dimer, the transverse dimer, and type 2 tetramer, highlighting the separation between TDMs in these aggregates.
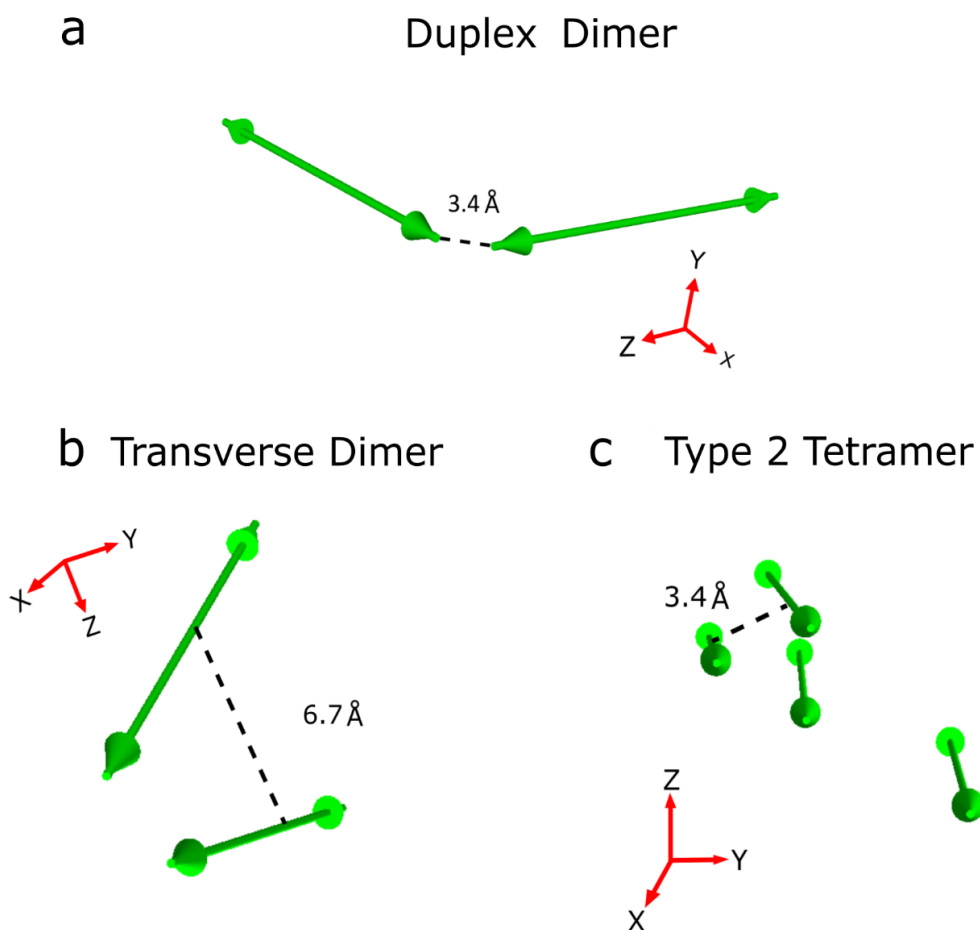
Figure 4.9. **Orientation of TDM vectors for (a) duplex dimer, (b) transverse dimer, and (c) type 2 tetramer derived by modeling the optical properties of the materials via an approach based on KRM theory. The TDM vector orientations were derived in Section 4.8.15. Green double-headed arrows correspond to TDM vectors, which are taken to lie along the long axis of the Cy5 dye. Dashed lines indicate the critical approach distance derived by the modeling; see main text for further details. The critical approach distance for the duplex dimer (i.e., J-aggregate) was taken to be the end-to-end distance, while the critical approach distance for the transverse dimer and type 2 tetramer (i.e., H-aggregates) was taken to be the center-to-center distance.**

Because of their fundamentally different packing configurations (see e.g. **Figures 4.1** and **4.9**), a direct comparison of the inter-dye separations of the J-like duplex dimer structure and the H-like transverse dimer and type 2 tetramer structures is not possible. To facilitate comparison, we thus define the end-to-end and face-to-face dye separation

observed in the J-like and H-like aggregate structures as critical approach distances (**Figure 4.9**). Viewed in this manner, the modeling derives a dye separation distance of 3.4 Å for the duplex dimer, while for the transverse dimer and type 2 tetramer, dye separation distances of 6.7 and 3.4 Å, respectively, are derived. For the structures with the shortest dye separation, i.e., the duplex dimer and type 2 tetramer, we measure the shortest lifetimes of 10 and 40 ps, respectively. For the transverse dimer, in contrast, where the distance is appreciably larger, we observe a much longer lifetime of 202 ps. Thus, consistent with the work of Liang *et al.*,[64] we observe a correlation between lifetime and dye separation. The reason for this correlation may be that at small separation distances the dyes exhibit appreciable wavefunction overlap. Furthermore, time-dependent changes in this wavefunction overlap may promote strong nonadiabatic coupling between the ground and excited states and thus facilitate nonradiative decay.[14,25] We posit such wavefunction overlap may occur between the indolenine end groups and the bridging pentamethine chains for the duplex dimer and tetramer, respectively.

<u>Heterogeneity and Variability of Lifetimes.</u>

Another factor contributing to the observed variability of excited-state lifetimes in the DNA-Cy5 aggregates may be heterogeneity. Heterogeneity can manifest itself as multiple DNA structures present in the solution, even though the number and type of basis DNA strands are identical. This can manifest in the form of static heterogeneity, where the DNA strands assemble and relax into multiple distinct DNA structures (or conformers). Additionally, dynamic heterogeneity may exist, wherein each structure fluctuates locally at the base pair level on a 100s of μs timescale. This latter process is known colloquially as DNA 'breathing';[65] it enables DNA replication and repair, and hence life on earth.

In a prototypical example of static heterogeneity, Cannon *et al.* reported "type 1" solutions of DNA-templated Cy5 aggregates (**Figure 4.1a,b**) that consist of a mixture of duplex DNA and DNA Holliday junctions.[47] Specifically, they showed that DNA-templated Cy5 aggregates constructed of DNA strands capable of forming both duplex DNA and DNA Holliday junctions (see e.g. Construct Preparation in Results), can indeed consist of a mixture of duplex DNA and DNA Holliday junctions by varying the amount of $MgCl_2$ present in the solution (**Figure 4.10**). The authors also showed that the interconversion between these structures is a slow process taking place on the order of minutes, which is consistent with the macroscopic structural changes necessary for this interconversion. The static heterogeneity present in the solution is evidenced in the TA results presented in **Figures 4.3 and 4.4**—the TA of the high-salt type 1 solution is well described by a model consisting of a mixture of duplex dimer and Holliday junction tetramer subpopulations. In addition, **Figures 4.3 and 4.4** show that two more components are required to model the data—a component associated with a small subpopulation of monomers, plus another component with optical properties and dynamics consistent with the long-lived adjacent dimer subpopulation (see e.g. **Figure 4.5e-h** and **Section S6**). We propose here that dynamic heterogeneity, or DNA 'breathing', may be the origin of these small subpopulations. Thus, leveraging the model originally developed by Cannon *et al.* that describes the solution as a mixture of duplex DNA and DNA Holliday junctions,[47] we propose to expand the model to include two additional structures to explain the presence of these two additional subpopulations (see e.g. **Figure 4.10**). Specifically, we propose that restricted and extended DNA "bubbles", or local pockets in the secondary structure that arise from DNA breathing, give rise to a small subpopulation of long-lived adjacent dimers

and monomers, respectively. The notion that DNA breathing might mediate interconversion between the short-lived duplex dimer and more longer-lived adjacent dimer and monomer configurations is wholly consistent with the correlation between dye separation and aggregate lifetime identified above. Additionally, in recent work by Marcus, von Hippel and co-workers in which they performed single molecule studies of Cy3-Cy5 pairs attached to single strand-duplex DNA junctions, they demonstrated the tendency for single stranded DNA segments to adopt configurations that could be grouped into three sets, or macrostates, which they described as compact, partially-extended, and fully-extended.[66] The restricted and extended bubble configurations we propose to explain the additional aggregate and monomer subpopulations observed here may be consistent with this interpretation of discrete, thermally accessible, transient dye-dye configurations.
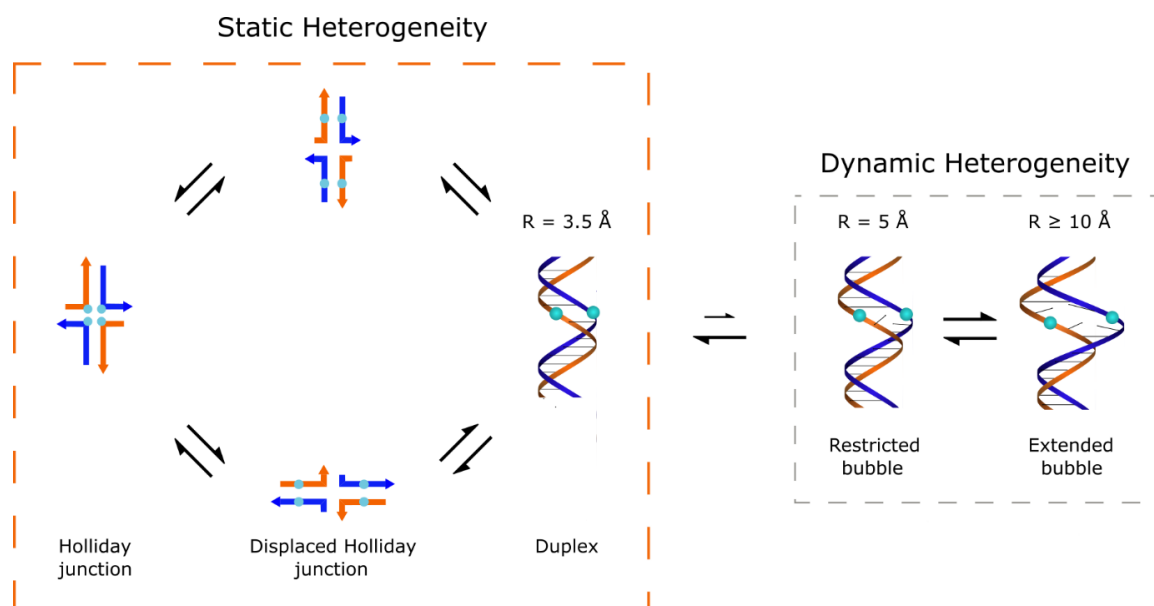
Figure 4.10.   Proposed model of the high-salt type 1 solution, which consists of a mixture of duplex DNA and DNA Holliday junction structures. The part of the model shown in the orange box is a classic example of static heterogeneity. The interconversion between duplex DNA and DNA Holliday junctions is a macroscopic structural change that takes place on the timescale of minutes, thus establishing a

steady-state mixture of components. We propose to expand this depiction of the high-salt type 1 solution with the addition of the structures shown in the gray box, which account for dynamic heterogeneity. Dynamic heterogeneity is present in these solutions via DNA 'breathing', a local structural change that takes place on a 100s of μs timescale. These structural changes are proposed to explain the presence of small subpopulations of long-lived adjacent dimers and monomers in the solution, as exemplified by the structures labeled "restricted bubble" and "extended bubble", respectively.

As another example of static heterogeneity, Mass *et al.* proposed a model for the "type 2" solutions of DNA-templated dye aggregates (**Figure 4.1c,d**) whereby the Holliday junction nanostructures can relax into multiple distinct configurations.[58,67,68] Such configurations include an open configuration and two distinct isomers of a stacked configuration. Critically, these distinct DNA configurations impact the dye aggregate configurations that are accessed. For example, **Figure 4.11** shows a range of possible DNA and dye aggregation configurations possible for the adjacent dimer, transverse dimer, trimer, and tetramer solutions.
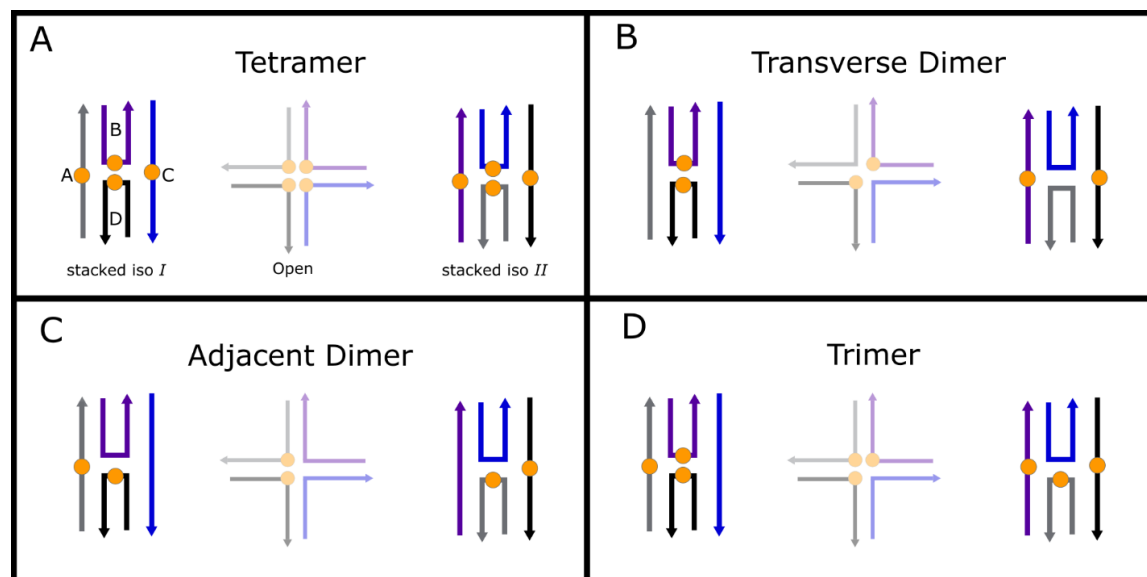
Figure 4.11.   Proposed model for the composition of the type 2 solutions, which includes the (a) tetramer, (b) transverse dimer, (c) adjacent dimer, and (d) trimer solutions. The schematic shows three possible configurations of the DNA template, which impact the different dye aggregate configurations that are possible. Due to the particular solution conditions, the predominant DNA configurations are the two stacked iso *I* and *II* configurations. A third, open configuration, which is present in a low amount in these solutions, is shown in reduced opacity.

To determine whether the open or stacked DNA configurations were predominant we first performed denaturation measurements. The results, shown in **Table 4.3** and **Section S16**, indicate that the stacked configurations are the predominant configurations in the adjacent dimer, transverse dimer, trimer, and tetramer solutions. All of these solutions, which were prepared with 15 mM MgCl$_2$ added, are found to exhibit a denaturation temperature on the order of ~60 °C, which is similar to that measured for a solution of unlabeled Holliday junctions with 15 mM MgCl$_2$ added. In contrast, a much smaller denaturation temperature of ~48 °C is measured for the unlabeled Holliday junctions prepared in a solution with 100 mM NaCl added. Given that the unlabeled Holliday junctions with 15 mM MgCl$_2$ and 100 mM NaCl added are known to primarily adopt stacked and open configurations, respectively, we therefore conclude that the two stacked configurations, iso *I* and *II*, are the predominant DNA configurations in the "type 2" DNA-templated Cy5 aggregate solutions.

Table 4.3. **Denaturation Temperatures of type 2 DNA-Dye Constructs**

DNA-Dye Construct	T_m (°C)
Unlabeled (100 mM NaCl added)	48.5
Unlabeled (15 mM MgCl$_2$ added)	60.5
Monomer	59.1
Adjacent Dimer	59.0
Transverse Dimer	60.9
Trimer	60.5
Tetramer	62.4

Next, we consider the plausibility of the model proposed in **Figure 4.11**, which indicates that two stacked DNA configurations are possible. Focusing on the tetramer and transverse dimer structures, the model predicts that these structures may adopt either one or two distinct dye aggregate configurations, respectively. In the case of the tetramer solution, for example, iso *I* and *II* are essentially equivalent in the model (**Figure 4.11a**); that is, the four dyes are positioned close to one another in a similar manner, such that we might expect the same aggregate configuration for the iso *I* and *II* DNA configurations. In the case of the transverse dimer solution, two distinct aggregate configurations appear in the model (**Figure 4.11b**). Namely, one configuration, iso *I*, where the dyes are closely spaced, and a second configuration, iso *II*, where the dyes are much farther apart. The dyes are spaced so far apart, in fact, that we might expect them to not interact and to behave independently (i.e., as uncoupled monomers). Indeed, this interpretation is consistent with the disproportionately large subpopulation of monomers observed in the transverse dimer solution (**Figure 4.6**). Critically, the model predicts little aggregate heterogeneity for both the tetramer and transverse dimer structures. Consistent with this expectation, pump-wavelength dependent TA measurements of the tetramer and transverse dimer solutions (see e.g. **Figures 4.5** and **4.6** and **Section S13**) indicated that these solutions exhibit little aggregate heterogeneity. Additional insights may be gleaned from **Table 4.3**. For example,

we find that the denaturation temperatures of the tetramer and transverse dimer solutions are greater than that of the unlabeled Holliday junctions, which indicates that dyes in these structures may act to stabilize the overall DNA-dye nanostructure, presumably via dye-dye interactions. Thus, we conclude that the tetramer and transverse dimer solutions exhibit little aggregate heterogeneity, a result consistent with the model, and that stabilizing dye-dye interactions may contribute to further suppression of aggregate heterogeneity.

Now we turn our attention to the adjacent dimer solution. For the adjacent dimer solution, the model predicts that, compared with the transverse dimer, the dyes are further separated and that, unlike for the tetramer, the dyes can be arranged in one of two ways to form an aggregate (**Figure 4.11c**). In the case of the adjacent dimer solution, we observed a denaturation temperature that was less than that of the unlabeled Holliday junction (**Table 4.3**). The lower denaturation temperature of the adjacent dimer solution may be explained by weaker dye-dye interactions, i.e., an overall destabilizing effect on the DNA-dye construct, which may, in part, be related to the larger separation of the dyes predicted by the model. The adjacent dimer solution also exhibited strong TA excitation wavelength dependence (**Figure 4.6**), suggesting appreciable heterogeneity. Although we found that the iso *I* and *II* configurations did not strongly impact aggregate heterogeneity for the tetramer and transverse dimers, apparently aggregate heterogeneity may occur in the case of the adjacent dimers due to the more distant spacing between dyes combined with differences in the flanking base pairs in the iso *I* and *II* configurations (**Section S17**). For example, Cunningham *et al.* showed that variations in the flanking base pairs can have a profound impact on aggregate packing type.[24] Specifically, these authors showed that Cy3 dimers templated using duplex DNA exhibited H- and J-aggregate packing types when

flanked with AT and GC base pairs, respectively. Consistent with this picture, a simple analysis of the TA of the DNA-templated Cy5 adjacent dimer aggregates indicated that the solution consisted not only of adjacent dimers, which tend to form J-aggregates with redshifted absorption spectra, but also a large proportion of transverse dimers, which tend to form H-aggregates with blueshifted absorption spectra (**Figure 4.6**). In further support of this interpretation, the absorption spectrum of the adjacent dimer solution (**Figure 4.1d**) exhibits obvious signatures of redshifted features attributable to adjacent dimers (i.e., J-aggregates) along with a strong absorption band at 600 nm that is consistent with the presence of an appreciable fraction of transverse dimers (i.e., H-aggregates). Lastly, it is critical to mention that the location of dyes both on the center and on the periphery or only on the center of the Holliday junction in the case of the adjacent and transverse dimer structures, respectively, may be another factor contributing to the differing degrees of heterogeneity observed in these solutions (**Section S17**). We conclude that the model may also explain the lower denaturation temperature and considerable heterogeneity observed for the adjacent dimer solution.

Regarding the trimer solution, the model suggests an even more complicated picture (**Figure 4.11d**). First, it is important to note that evidence indeed exists for the presence of "true" trimer configurations where the exciton is delocalized about all three dyes; for example, via the prominent H-aggregate absorption band that exhibits a blueshift intermediate between that of the transverse dimer and tetramer (**Figure 4.1d**). Furthermore, exciting the short-wavelength part of the blueshifted H-aggregate absorption band indeed appears to selectively excite "true" trimer configurations, which is evident by the mapping of the absorption spectrum onto the TA results in a similar manner to that observed for the

tetramer (see e.g. **Figures 4.7** and **4.8**). However, the model also predicts two trimer configurations that are not symmetric. On the one hand, the model predicts that the iso *I* configuration of the trimer could, in some sense, be considered a combination of iso *I* of the adjacent and transverse dimers. Viewed in this manner, we might expect to observe a subpopulation of these dimers in the trimer solution. Indeed, both the additional structure in the prominent H-aggregate absorption band at long wavelength (**Figure 4.1d** and **Section S11**) along with the prominent GSB feature appearing at 600 nm in the femtosecond TA spectra for the trimer solution excited at 660 nm (**Section S10**) are readily explained by invoking the presence of an additional subpopulation of transverse dimers. Similar to the iso *I* configuration, iso *II* of the trimer can be viewed as a combination of the iso *I* and *II* of the adjacent dimer. In the paragraph above, we argued that the distant spacing of the dyes in these configurations may explain the lower denaturation temperature and more extensive heterogeneity observed in that solution. In the case of the trimer solution, the addition of a third dye may further act to destabilize the DNA-dye nanostructure. However, **Table 4.3** indicates that the denaturation temperature of the trimer solution is very similar to that of the unlabeled Holliday junction. To explain this seeming anomaly, it is possible that transverse dimers present in the solution, via iso *I*, may act to stabilize the structure and thereby increase the denaturation temperature of the solution to approach that of the unlabeled Holliday junction. Coincidentally, this interpretation may also explain the prominence of spectral features attributable to transverse dimers in the trimer solution (**Sections S10** and **S12**); that is, the increased stabilization that the transverse dimer imparts may also increase the fraction of iso *I* configurations in the solution.

Finally, an additional source of heterogeneity may arise from the "semi-mobility" of the type 2 DNA templates. Whereas "mobile" Holliday junctions can undergo full branch migration (**Figure 4.10**, left panel) due to their fully symmetric nucleotide sequences (i.e., the two basis sequences are the reverse complement of one another), semi-mobile Holliday junctions are only able to undergo limited branch migration, the extent of which is determined by the length of the symmetric (i.e., reverse complementary) domains on the basis sequences at the center of the junction.[69] For the type 2 DNA template, the bases adjacent to the dye sites allow for branch migration of a single base which permits the Holliday junction to alternately shorten and lengthen the vertical and horizontal arms, respectively, by one base. This process is illustrated for the type 2 sequences in **Section S18**. For the transverse dimer, the horizontal displacement would increase the dye separation and possibly promote a subpopulation of monomers. The effect would be similar for the trimer and tetramer, but would instead promote smaller aggregates rather than monomers. Conversely, branch migration for the adjacent dimer would cause the dyes to move together as a unit and remain dimerized, but the changes in the DNA backbone may change the dye packing and lead to a distinct dimer subpopulation. Thus, both the stacked isomer and branch migration models may potentially contribute to the observed heterogeneity of the type 2 DNA templates.

In summary, the extensive heterogeneity observed in the trimer solution may well be explained by this model of static heterogeneity, which, as described above, suggests that many distinct dye aggregate configurations are possible. Clearly, the choice of the number of dyes and their relative position on the DNA template impacts the extent of heterogeneity,

which, in the absence of mitigation strategies, may impact studies and applications that require homogeneous assemblies of materials.

4.6 Conclusion

In conclusion, we observed drastically reduced excited-state lifetimes across a broad set of DNA-templated Cy5 aggregates. For the type 1 aggregates, we measured lifetimes of ~10 and ~30 ps for the duplex dimer and type 1 tetramer, respectively, consistent with prior work.[25] The type 2 aggregates also exhibited reduced lifetimes, but with a broader range of timescales. Specifically, we measured lifetimes of ~202 and ~40 ps for the transverse dimer and tetramer, respectively, and lifetimes ranging from ~40-242 and ~26-82 ps for the adjacent dimer and trimer, respectively. The reduced lifetimes result from significantly enhanced nonradiative decay rates concomitant with aggregation. By comparing the orientation of dyes of selected structures with their respective lifetimes, we observed a correlation between dye separation and lifetime whereby close spacing between dyes resulted in the shortest lifetimes. We also observed a weak correlation of lifetime with exciton delocalization. These results suggest that DNA-templated dye aggregates may indeed represent designer materials that can be custom tailored for a broad set of specific applications. For applications where short lifetimes are advantageous, such as in sensing and photodynamic therapy where either large emission contrast or extensive heat dissipation are desired, our results suggest that tuning materials for short dye separation is desirable. For applications where long lifetimes are important, on the other hand, large dye separation may be required. If both short dye separation and long lifetime are important, i.e., to achieve aggregates with large coupling strength and long-lived excited states, additional mechanistic insight may be needed to optimize these multiple parameters

simultaneously; otherwise, there may be a tradeoff among dye separation, coupling strength, and lifetime.

We also provided significant insight into potential sources of heterogeneity in DNA-templated dye aggregates that may explain the broad set of measured lifetimes. Varying extents of heterogeneity in the different solutions, ranging from limited to extensive, were highlighted by pump wavelength dependent transient absorption combined with global analyses via parallel decay models. For example, the duplex dimer and Holliday junction-based transverse dimer and tetramer solutions appeared to exhibit limited heterogeneity, whereas the Holliday junction-based adjacent dimer and trimer solutions appeared to exhibit more extensive heterogeneity. We consistently observed a subset of aggregates with longer lifetimes in most solutions, which we proposed to arise from transient local structural fluctuations of the DNA template via 'breathing'. The local structural fluctuations of the DNA may lead to large dye separation and correspondingly longer lifetimes, with a limiting case being two non-interacting dye monomers separated by a large distance. Another potential source of heterogeneity we identified was associated largely with the type 2 aggregates. Specifically, we found that the DNA Holliday junctions used to template the type 2 aggregates adopted a stacked configuration and that the stacked configuration could exist in one of two structural forms, iso *I* or *II*. The transverse dimer and tetramer aggregates had only one type of aggregate structure within this model, which was consistent with the general lack of heterogeneity observed in these solutions along with their higher denaturation temperatures. On the other hand, the adjacent dimer and trimer aggregates had two types of aggregate structures within this model, which was consistent with their more extensive heterogeneity and lower denaturation temperatures.

Moving forward, these materials may need to be further modified, e.g., by modifying the dye and/or DNA template to promote stronger dye and DNA interactions, respectively, to mitigate these potential sources of heterogeneity.

4.8 References

(1) Mirkovic, T.; Ostroumov, E. E.; Anna, J. M.; Grondelle, R. Van; Govindjee; Scholes, G. D. Light Absorption and Energy Transfer in the Antenna Complexes of Photosynthetic Organisms. *Chem. Rev.* **2017**, *117*, 249–293.

(2) Brixner, T.; Hildner, R.; Köhler, J.; Lambert, C.; Würthner, F. Exciton Transport in Molecular Aggregates – From Natural Antennas to Synthetic Chromophore Systems. *Adv. Energy Mater.* **2017**, *7*, 1700236.

(3) Ostroverkhova, O. Organic Optoelectronic Materials: Mechanisms and Applications. *Chem. Rev.* **2016**, *116*, 13279–13412.

(4) Zang, L.; Che, Y.; Moore, J. S. One-Dimensional Self-Assembly of Planar π-Conjugated Molecules: Adaptable Building Blocks for Organic Nanodevices. *Acc. Chem. Res.* **2008**, *41*, 1596–1608.

(5) Arunkumar, E.; Ajayaghosh, A.; Daub, J. Selective Calcium Ion Sensing with a Bichromophoric Squaraine Foldamer. *J. Am. Chem. Soc.* **2005**, *127*, 3156–3164.

(6) Okamoto, A. ECHO Probes: A Concept of Fluorescence Control for Practical Nucleic Acid Sensing. *Chem. Soc. Rev.* **2011**, *40*, 5815–5828.

(7) Yurke, B.; Kuang, W. Passive Linear Nanoscale Optical and Molecular Electronics Device Synthesis from Nanoparticles. *Phys. Rev. A* **2010**, *81*, 033814-1–9.

(8) Graugnard, E.; Kellis, D. L.; Bui, H.; Barnes, S.; Kuang, W.; Lee, J.; Hughes, W. L.; Knowlton, W. B.; Yurke, B. DNA-Controlled Excitonic Switches. *Nano Lett.* **2012**, *12*, 2117–2122.

(9) Laboda, C.; Duschl, H.; Dwyer, C. L. DNA-Enabled Integrated Molecular Systems for Computation and Sensing. *Acc. Chem. Res.* **2014**, *47*, 1816–1824.

(10) Cannon, B. L.; Kellis, D. L.; Davis, P. H.; Lee, J.; Kuang, W.; Hughes, W. L.; Graugnard, E.; Yurke, B.; Knowlton, W. B. Excitonic AND Logic Gates on DNA Brick Nanobreadboards. *ACS Photonics* **2015**, *2*, 398–404.

(11) Sawaya, N. P. D.; Rappoport, D.; Tabor, D. P.; Aspuru-Guzik, A. Excitonics: A Set of Gates for Molecular Exciton Processing and Signaling. *ACS Nano* **2018**, *12*, 6410–6420.

(12) Kellis, D. L.; Sarter, C.; Cannon, B. L.; Davis, P. H.; Graugnard, E.; Lee, J.; Pensack, R. D.; Kolmar, T.; Jäschke, A.; Yurke, B.; et al. An All-Optical Excitonic Switch Operated in the Liquid and Solid Phases. *ACS Nano* **2019**, *13*, 2986–2994.

(13) Hu, W.; Miao, X.; Tao, H.; Baev, A.; Ren, C.; Fan, Q.; He, T.; Huang, W.; Prasad, P. N. Manipulating Nonradiative Decay Channel by Intermolecular Charge Transfer for Exceptionally Improved Photothermal Conversion. *ACS Nano* **2019**, *13*, 12006–12014.

(14) Dean, J. C.; Oblinsky, D. G.; Rafiq, S.; Scholes, G. D. Methylene Blue Exciton States Steer Nonradiative Relaxation: Ultrafast Spectroscopy of Methylene Blue Dimer. *J. Phys. Chem. B* **2016**, *120*, 440–454.

(15) Scheibe, G. Über Die Veränderlichkeit Der Absorptionsspektren in Lösungen Und Die Nebenvalenzen Als Ihre Ursache. *Angew. Chemie* **1937**, *50*, 212–219.

(16) Jelley, E. E. Molecular, Nematic and Crystal States of I: I-Diethyl--Cyanine Chloride. *Nature* **1937**, *139*, 631–632.

(17) Davydov, A. S. Theory of Absorption Spectra of Molecular Crystals. *Translated and Reprinted from Zh. Eksp. Teor. Fiz.* **1948**, *18*, 210–218.

(18) Davydov, A. S. The Theory of Molecular Excions. *Sov. Phys. Uspekhi* **1964**, *82*, 145–178.

(19) Kühn, O.; Renger, T.; May, V. Theory of Exciton-Vibrational Dynamics in Molecular Dimers. *Chem. Phys.* **1996**, *204*, 99–114.

(20) Hestand, N. J.; Spano, F. C. Molecular Aggregate Photophysics beyond the Kasha Model: Novel Design Principles for Organic Materials. *Acc. Chem. Res.* **2017**, *50*, 341–350.

(21) Hestand, N. J.; Spano, F. C. Expanded Theory of H- and J-Molecular Aggregates: The Effects of Vibronic Coupling and Intermolecular Charge Transfer. *Chem. Rev.* **2018**, *118*, 7069-7163

(22) Turro, N. J.; Scaiano, J. C.; Ramamurthy, V. *Modern Molecular Photochemistry of Organic Molecules*; University Science Books: Sausalito, Calif, 2010.

(23) Sundström, V.; Gillbro, T. Excited State Dynamics and Photophysics of Aggregated Dye Chromophores in Solution. *J. Chem. Phys.* **1985**, *83*, 2733–2743.

(24) Cunningham, P. D.; Kim, Y. C.; Díaz, S. A.; Buckhout-White, S.; Mathur, D.; Medintz, I. L.; Melinger, J. S. Optical Properties of Vibronically Coupled Cy3 Dimers on DNA Scaffolds. *J. Phys. Chem. B* **2018**, *122*, 5020–5029.

(25) Huff, J. S.; Davis, P. H.; Christy, A.; Kellis, D. L.; Kandadai, N.; Toa, Z. S. D.; Scholes, G. D.; Yurke, B.; Knowlton, W. B.; Pensack, R. D. DNA-Templated Aggregates of Strongly Coupled Cyanine Dyes: Nonradiative Decay Governs Exciton Lifetimes. *J. Phys. Chem. Lett.* **2019**, *10*, 2386–2392.

(26) Heyne, B. Self-Assembly of Organic Dyes in Supramolecular Aggregates. *Photochem. Photobiol. Sci.* **2016**, *15*, 1103–1114.

(27) Haedler, A. T.; Kreger, K.; Issac, A.; Wittmann, B.; Kivala, M.; Hammer, N.; Köhler, J.; Schmidt, H. W.; Hildner, R. Long-Range Energy Transport in Single Supramolecular Nanofibres at Room Temperature. *Nature* **2015**, *523*, 196–199.

(28) Scholes, G. D.; Fleming, G. R.; Olaya-Castro, A.; van Grondelle, R. Lessons from Nature about Solar Light Harvesting. *Nat. Chem.* **2011**, *3*, 763–774.

(29) Snow, C. D.; Nguyen, H.; Pande, V. S.; Gruebele, M. Absolute Comparison of Simulated and Experimental Protein-Folding Dynamics. *Nature* **2002**, *420*, 102–106.

(30) Baker, D.; Sali, A. Protein Structure Prediction and Structural Genomics. *Science* **2001**, *294*, 93–96.

(31) Dill, K. A.; MacCallum, J. L. The Protein-Folding Problem, 50 Years On. *Science* **2012**, *338*, 1042–1046.

(32) Yeates, T. O. Geometric Principles for Designing Highly Symmetric Self-Assembling Protein Nanomaterials. *Annu. Rev. Biophys.* **2017**, *46*, 23–42.

(33) Huang, P. S.; Boyken, S. E.; Baker, D. The Coming of Age of de Novo Protein Design. *Nature* **2016**, *537*, 320–327.

(34) Bale, J. B.; Gonen, S.; Liu, Y.; Sheffler, W.; Ellis, D.; Thomas, C.; Cascio, D.; Yeates, T. O.; Gonen, T.; King, N. P.; et al. Accurate Design of Megadalton-Scale Two-Component Icosahedral Protein Complexes. *Science* **2016**, *353*, 389–394.

(35) Seeman, N. C.; Kallenbach, N. R. Design of Immobile Nucleic Acid Junctions. *Biophys. J.* **1983**, *44*, 201–209.

(36) Winfree E.; Liu F.; Wenzler L. A.; Seeman N. C. Design and Self-Assembly of Two-Dimensional DNA Crystals. *Nature* **1998**, *394*, 539–544.

(37) Douglas, S. M.; Marblestone, A. H.; Teerapittayanon, S.; Vazquez, A.; Church, G. M.; Shih, W. M. Rapid Prototyping of 3D DNA-Origami Shapes with caDNAno. *Nucleic Acids Res.* **2009**, *37*, 5001–5006.

(38) Rothemund, P. W. K. Folding DNA to Create Nanoscale Shapes and Patterns. *Nature* **2006**, *440*, 297–302.

(39) Wang, D.; Yu, L.; Huang, C.; Arya, G.; Chang, S.; Ke, Y. Programmable Transformations of DNA Origami Made of Small Modular Dynamic Units. *J. Am. Chem. Soc.* **2021**, *143*, 2256–2263.

(40) Seifert, J. L.; Connor, R. E.; Kushon, S. A.; Wang, M.; Armitage, B. A. Spontaneous Assembly of Helical Cyanine Dye Aggregates on DNA Nanotemplates. *J. Am. Chem. Soc.* **1999**, *121*, 2987-2995.

(41) Wang, M.; Silva, G. L.; Armitage, B. A. DNA-Templated Formation of a Helical Cyanine Dye J-Aggregate. *J. Am. Chem. Soc.* **2000**, *122*, 9977–9986.

(42) Garoff, R. A.; Litzinger, E. A.; Connor, R. E.; Fishman, I.; Armitage, B. A. Helical Aggregation of Cyanine Dyes on DNA Templates: Effect of Dye Structure on Formation of Homo- and Heteroaggregates. *Langmuir* **2002**, *18*, 6330–6337.

(43) Asanuma, H.; Fujii, T.; Kato, T.; Kashida, H. Coherent Interactions of Dyes Assembled on DNA. *J. Photochem. Photobiol. C Photochem. Rev.* **2012**, *13*, 124–135.

(44) Cunningham, P. D.; Khachatrian, A.; Buckhout-White, S.; Deschamps, J. R.; Goldman, E. R.; Medintz, I. L.; Melinger, J. S. Resonance Energy Transfer in DNA Duplexes Labeled with Localized Dyes. *J. Phys. Chem. B* **2014**, *118*, 14555–14565.

(45) Melinger, J. S.; Khachatrian, A.; Ancona, M. G.; Buckhout-White, S.; Goldman, E. R.; Spillmann, C. M.; Medintz, I. L.; Cunningham, P. D. FRET from Multiple Pathways in Fluorophore-Labeled DNA. *ACS Photonics* **2016**, *3*, 659–669.

(46) Markova, L. I.; Malinovskii, V. L.; Patsenker, L. D.; Häner, R. J- vs. H-Type Assembly: Pentamethine Cyanine (Cy5) as a near-IR Chiroptical Reporter. *Chem. Commun.* **2013**, *49*, 5298–5300.

(47) Cannon, B. L.; Kellis, D. L.; Patten, L. K.; Davis, P. H.; Lee, J.; Graugnard, E.; Yurke, B.; Knowlton, W. B. Coherent Exciton Delocalization in a Two-State DNA-Templated Dye Aggregate System. *J. Phys. Chem. A* **2017**, *121*, 6905–6916.

(48) Asanuma, H.; Murayama, K.; Kamiya, Y.; Kashida, H. The DNA Duplex as an Aqueous One-Dimensional Soft Crystal Scaffold for Photochemistry. *Bull. Chem. Soc. Jpn.* **2018**, *91*, 1739–1748.

(49) Cannon, B. L.; Patten, L. K.; Kellis, D. L.; Davis, P. H.; Lee, J.; Graugnard, E.; Yurke, B.; Knowlton, W. B. Large Davydov Splitting and Strong Fluorescence Suppression: An Investigation of Exciton Delocalization in DNA-Templated Holliday Junction Dye Aggregates. *J. Phys. Chem. A* **2018**, *122*, 2086–2095.

(50) Mazuski, R. J.; Díaz, S. A.; Wood, R. E.; Lloyd, L. T.; Klein, W. P.; Mathur, D.; Melinger, J. S.; Engel, G. S. Ultrafast Excitation Transfer in Cy5 DNA Photonic Wires Displays Dye Conjugation and Excitation Energy Dependency. *J. Phys. Chem. Lett.* **2020**, *11*, 4163–4172.

(51) Sohail, S. H.; Otto, J. P.; Cunningham, P. D.; Kim, Y. C.; Wood, R. E.; Allodi, M. A.; Higgins, J. S.; Melinger, J. S.; Engel, G. S. DNA Scaffold Supports Long-Lived Vibronic Coherence in an Indodicarbocyanine (Cy5) Dimer. *Chem. Sci.*

2020, *11*, 8546–8557.

(52) Kringle, L.; Sawaya, N. P. D.; Widom, J.; Adams, C.; Raymer, M. G.; Aspuru-Guzik, A.; Marcus, A. H. Temperature-Dependent Conformations of Exciton-Coupled Cy3 Dimers in Double-Stranded DNA. *J. Chem. Phys.* **2018**, *148*, 085101.

(53) Heussman, D.; Kittell, J.; Kringle, L.; Tamimi, A.; von Hippel, P. H.; Marcus, A. H. Measuring Local Conformations and Conformational Disorder of (Cy3)2 Dimer Labeled DNA Fork Junctions Using Absorbance, Circular Dichroism and Two-Dimensional Fluorescence Spectroscopy. *Faraday Discuss.* **2019**, *216*, 211–235.

(54) Hart, S. M.; Chen, W. J.; Banal, J. L.; Bricker, W. P.; Dodin, A.; Markova, L.; Vyborna, Y.; Willard, A. P.; Häner, R.; Bathe, M.; et al. Engineering Couplings for Exciton Transport Using Synthetic DNA Scaffolds. *Chem* **2021**, *7*, 752–773.

(55) Dominik Spiegel, J.; Fulle, S.; Kleinschmidt, M.; Gohlke, H.; Marian, C. M. Failure of the IDA in FRET Systems at Close Inter-Dye Distances Is Moderated by Frequent Low K2 Values. *J. Phys. Chem. B* **2016**, *120*, 8845–8862.

(56) Kasha, M. Energy Transfer Mechanisms and the Molecular Exciton Model for Molecular Aggregates. *Radiat. Res.* **1963**, *20*, 55–71.

(57) Kasha, M.; Rawls, H. R.; Ashraf El-Bayoumi, M. The Exciton Model in Molecular Spectroscopy. *Pure Appl. Chem.* **1965**, *11*, 371–392.

(58) Mass, O. A.; Wilson, C. K.; Roy, S. K.; Barclay, M. S.; Patten, L. K.; Terpetschnig, E. A.; Lee, J.; Pensack, R. D.; Yurke, B.; Knowlton, W. B. Exciton Delocalization in Indolenine Squaraine Aggregates Templated by DNA Holliday Junction Scaffolds. *J. Phys. Chem. B* **2020**, *124*, 9636–9647.

(59) Böhmer, M.; Enderlein, J. Fluorescence Spectroscopy of Single Molecules under Ambient Conditions: Methodology and Technology. *ChemPhysChem* **2003**, *4*, 792–808.

(60) Snellenburg, J. J.; Laptenok, S.; Seger, R.; Mullen, K. M.; van Stokkum, I. H. M. Glotaran: A Java-Based Graphical User Interface for the R Package TIMP. *J. Stat. Softw.* **2012**, *49*.

(61) Scharf, B.; Dinur, U. Striking Dependence of the Rate of Electronic Radiationless Transitions on the Size of the Molecular System. *Chem. Phys. Lett.* **1984**, *105*, 78–82.

(62) Humeniuk, A.; Mitrić, R.; Bonačić-Koutecký, V. Size Dependence of Non-Radiative Decay Rates in J - Aggregates. *J. Phys. Chem. A* **2020**, 124, 10143–10151.

(63) Das, S.; Kamat, P. V. Can H-Aggregates Serve as Light-Harvesting Antennae? Triplet−Triplet Energy Transfer between Excited Aggregates and Monomer Thionine in Aersol-OT Solutions. *J. Phys. Chem. B* **1999**, *103*, 209–215.

(64) Liang, K.; Farahat, M. S.; Perlstein, J.; Law, K. Y.; Whitten, D. G. Exciton Interactions in Nonconjugated Squaraine Dimers. Mechanisms for Coupling and Consequences for Photophysics and Photochemistry. *J. Am. Chem. Soc.* **1997**, *119*, 830–831.

(65) Von Hippel, P. H.; Johnson, N. P.; Marcus, A. H. Fifty Years of DNA "Breathing": Reflections on Old and New Approaches. *Biopolymers* **2013**, *99*, 923–954.

(66) Israels, B.; Albrecht, C. S.; Dang, A.; Barney, M.; von Hippel, P. H.; Marcus, A.H.

Sub-millisecond Conformational Transitions of Short Single-Stranded DNA Lattices by Photon Correlation Single-Molecule FRET. bioRxiv doi: 10.1101/2021.04.09.439239.

(67)   Lilley, D. M. J.; Norman, D. G. The Holliday Junction Is Finally Seen with Crystal Clarity. *Nat. Struct. Biol.* **1999**, *6*, 897–899.

(68)   Joo, C.; McKinney, S. A.; Lilley, D. M. J.; Ha, T. Exploring Rare Conformational Species and Ionic Effects in DNA Holliday Junctions Using Single-Molecule Spectroscopy. *J. Mol. Biol.* **2004**, *341*, 739–751.

(69)   Seeman, N. C. Nucleic Acid Junctions and Lattices. *J. theor. Biol.* **1982**, *99*, 237–247.

CHAPTER FIVE: CONCLUSIONS AND FUTURE WORK

In conclusion, dye aggregates are diverse materials that can exhibit drastically different optical and dynamical properties than the corresponding isolated dye, which makes them of interest for applications in sensing, nanophotonics, computing, and quantum information. DNA nanotechnology can facilitate controlled assembly of dye aggregates, allowing for basic research into their properties in addition to providing a platform for realizing advanced applications. The preceding three chapters of this dissertation presented studies of several DNA-templated aggregates of the dyes Cy5 and Cy5.5. Taken together, these studies represent a significant contribution to the knowledge base of DNA-templated dye aggregates with specific contributions to our understanding of 1) how to achieve control of the optical spectra of DNA-templated dye aggregates, 2) structural parameters that control the excited-state dynamics of DNA-templated dye aggregates, and 3) how to identify and classify sources of heterogeneity. The results of these studies and their significance are summarized below, followed by a discussion of potential future work.

The primary results from **Chapter 2** are summarized as follows:

1. Strongly-coupled heterotetramers of Cy5 and Cy5.5 are readily formed when templated onto the immobile DNA Holliday junction template first introduced by Cannon and coworkers.[1]

2. The S_0-S_1 electronic transition energies of the heterotetramers are adequately modeled using a purely-electronic exciton theory model that neglects vibronic coupling and implicitly assumes the dyes reside at the corners of a square. The transition energies

can be fit globally using the nearest-neighbor exitonic coupling strength, J_N, as the sole fitting parameter, with the best fit resulting from J_N of 108 meV. The individual best fits of each tetramer spectrum result in J_N values that cluster around the global fit average, ranging from 92 to 123 meV with increasing Cy5 content.

3. The excited-state lifetimes of the heterotetramers and homotetramers are all very similar, ranging between 30 and 50 ps. These lifetimes are significantly shorter than those of the Cy5 and Cy5.5 monomers, which were 1870 and 920 ps, respectively. These short excited-state lifetimes in conjunction with the very low fluorescence intensity indicate that the reduction in excited-state lifetimes relative to the monomers is due to enhanced nonradiative relaxation upon forming aggregates.

The study detailed in **Chapter 2** was the first, to the best of our knowledge, to examine heterotetramers that depart from a 1:1 composition ratio of dye species. Studying these intermediate compositions allowed us to demonstrate that heteroaggregation of Cy5 and Cy5.5 leads to discrete tunability of the electronic transition energies. The ability of the purely-electronic exciton theory model to capture the progression of transition energies suggests that Cy5 and Cy5.5 are largely interchangeable in aggregates, exhibiting behavior reminiscent of alloying. These results are significant because they provide a potentially-generalizable strategy for controlling the transition energies of dye aggregates, which is important for energy transfer applications as we highlighted with our proposed J-aggregate energy relay. The study also sheds further light on the phenomenon of nonradiative quenching of cyanines, showing that heteroaggregation has no appreciable effect on the nonradiative relaxation kinetics since the lifetimes of the homo- and heteroaggregates were all similarly decreased.

The primary results from **Chapter 3** are summarized as follows:

1. Fluorescence excitation measurements indicate that Cy5 monomers are present in the J-dimer and H-tetramer solutions and contribute the majority of the measured fluorescence emission. The Cy5 monomer fluorescence was observed despite performing gel electrophoresis to remove any free dye or SSDNA monomers from the solutions.

2. An in-depth photophysical characterization of the duplex J-dimer and Holliday junction H-tetramer Cy5 aggregates first reported by Cannon *et al.* corroborates that both structures exhibit drastically-reduced fluorescence compared to the Cy5 monomer. Relative fluorescence quantum yield measurements reveal that the fluorescence quantum yield of solutions of Cy5 monomer attached to SSDNA is ~0.3, while the J-dimer and H-tetramer solution fluorescence quantum yields can be estimated to be 0.01 and 0.001, respectively.

3. The excited state lifetimes of the Cy5 monomer, J-dimer, and H-tetramer are 1300 ps, 11 ps, and 40 ps, respectively, as measured by femtosecond transient absorption spectroscopy.

4. The TA kinetics traces of the J-dimer and H-tetramer solutions are multi-exponential, with a long-lived component consistent with a small subpopulation of the Cy5 monomer subpopulation known to exist in the solutions.

5. The fluorescence quantum yields and excited-state lifetimes can be used to calculate the radiative and nonradiative decay rates of the monomer, and make a bounded estimation of these quantities for the J-dimer and H-tetramer solutions. The nonradiative decay rates of the monomer, J-dimer, and H-tetramer solutions

were found to be 5.5×10^8, 9.1×10^8, and 2.9×10^8, respectively. Accordingly, nonradiative decay processes account for 99.9% and 99.96% of the relaxation observed in the J-dimer and H-tetramer, respectively.

While not the primary result of the work, discovering the monomer subpopulations is a significant result because it allowed us to account for their presence in subsequent measurements and thus properly interpret our experimental data. It was important to report these subpopulations so that other researchers interested in DNA-templated aggregates can take them into account when interpreting their own measurements. Because of the monomer subpopulations, we interpreted our measurements of the fluorescence quantum yields of the J-dimer and H-tetramer solutions as an upper boundary of the fluorescence quantum yield of those structures. The dramatic reduction in fluorescence quantum yield exhibited by the J-dimer and H-tetramer was important to establishing that aggregation led to an increase in the nonradiative decay rate relative to the radiative decay rate. Taken with the fluorescence quantum yields, the reduced excited-state lifetimes can be attributed virtually entirely to an increase in the nonradiative decay rate of the aggregates with respect to the monomer. This result was significant because, at the time it was published, few studies had reported time-resolved measurements of DNA-templated dye aggregates, and there was some confusion about how to interpret reduced excited-state lifetimes. With this study, we added to a growing body of evidence that DNA-templated cyanine aggregates exhibit reduced lifetimes largely due to enhanced nonradiative decay.

The primary results from **Chapter 4** are summarized as follows:

1. Spectrally-resolved femtosecond TA measurements of six DNA-templated Cy5 aggregates revealed drastically-accelerated relaxation kinetics relative to the Cy5 monomer, with lifetimes ranging from 10 to 240 ps. The reduced lifetimes were attributed to enhanced nonradiative decay upon aggregation.

2. Analysis of lifetimes with respect to structural parameters suggests that increasing the extent of exciton delocalization (e.g. the number of dyes comprising the aggregate) somewhat attenuates the nonradiative decay enhancement upon forming an aggregate. This interpretation is consistent with theory that suggests that reduced nuclear displacement upon excitation in larger aggregates may lead to reduced nonradiative decay.[2,3] Additionally, reducing inter-dye separation may lead to increased nonradiative quenching.

3. Conducting transient absorption measurements at multiple excitation wavelengths can reveal the presence of aggregate and monomer subpopulations.

4. Additional transient absorption measurements of the Type 1 aggregate solutions known to contain different ratios of the same 2 aggregate subpopulations were conducted at multiple excitation wavelengths and global target analyses of the resulting spectrotemporal datasets yielded species associated spectra that largely reproduce the known TA spectra of the subpopulations.

5. For heterogeneous aggregate solutions in which the subpopulations have similar lifetimes, global target analysis is of limited use.

The results of the excited-state lifetime measurements paired with the limited structural analysis provide some important insights. For example, the observed reduced excited-state lifetimes in all aggregate solutions relative to the Cy5 monomer is

significant because it further supports the interpretation that enhanced nonradiative relaxation is a general effect of aggregation in Cy5 aggregates. However, in this study we measured a much larger range of lifetimes than for the aggregates studied in **Chapters 2** and **3**. For example, the 200 ps excited-state lifetime of the transverse dimer is ~20 fold longer than the 10 ps lifetime of the J-dimer, while being only ~7× shorter than the Cy5 monomer. Furthermore, we observed examples of both J- and H-aggregates with excited state lifetimes greater than 200 ps. This observation is an important result because it shows that changing only the DNA template partially mitigated nonradiative decay enhancement. Finally, there appears to be no strong correlation between the excitonic coupling strength, J, and enhanced nonradiative decay, which is promising because proposed applications that require strong excitonic coupling such as quantum computing would suffer from greatly reduced excited-state lifetimes.

Our results related to heterogeneity are also of potential use to the DNA-templated dye aggregate research community. In **Chapter 4**, we demonstrated that a simple test for heterogeneity is to collect TA measurements at multiple excitation wavelengths. This approach is complementary to the steady-state fluorescence techniques used in **Chapter 3**, allowing for detection of non-fluorescent aggregate subpopulations. By extracting spectra that largely resemble the TA spectra expected for the J-dimer, H-tetramer, and monomer, we demonstrated the potential utility of GTA for analyzing TA datasets of heterogeneous solutions. We further demonstrated clear limits to the approach when the adjacent- and transverse-dimer TA spectra could not be extracted from a dataset containing contributions from both due to their similar lifetimes. These

spectroscopic and analytical approaches we first demonstrated in **Chapter 4** have since become standard practice within our own research group for identifying heterogeneity, and will likely prove useful in future efforts to manage heterogeneity in spectroscopic studies of DNA-templated dye aggregates.

The above results raise questions that motivate further investigation. Some of these questions and ideas for follow-up studies are presented below:

1. Can aggregates of three or more distinct dyes undergo strong excitonic interactions? The results of **Chapter 2** show that the immobile DNA Holliday junction can be used as a test bed for studying heteroaggregation. If DNA sequences modified with commercially-available dyes are used, it is no more complicated to prepare solutions of aggregates containing three or four distinct dyes than it is to use two. There are, however, considerably more permutations of heterotetramers afforded by using more distinct dyes, and it may be necessary to sample the permutations rather than prepare them all.

2. Will DNA Holliday junction-templated heterotetramers of chemically-distinct dyes other than Cy5 and Cy5.5 exhibit a similar discrete tunability of their absorption frequency? Studies that reproduce the work of **Chapter 2** using different pairs of chemically-distinct dyes to form heterotetramers could shed light on the generality of the alloy-like effect observed for Cy5 and Cy5.5.

3. Can optical monomers be fully suppressed in solutions of DNA-templated dye aggregates at room temperature? In **Chapter 3**, we showed that monomers account for the majority of the fluorescence measured in DNA-templated aggregates of Cy5, despite efforts to eliminate single-stranded monomers from the solutions via

gel electrophoresis. In **Chapter 4** we further showed, via global target analyses of spectrally-resolved transient absorption datasets of DNA-templated Cy5 aggregate solutions, that monomer subpopulations contribute to the TA spectra when the excitation wavelength overlaps with the optical absorption of the Cy5 monomer. We also identified DNA breathing as a probable source of "transient" monomers in solution. A future study could test this hypothesis by measuring how the fluorescence intensity of a DNA-templated aggregate solution changes as a function of temperature. Typically, one expects fluorescence intensity to increase with reduced temperature since nonradiative decay mechanisms such as photoisomerization are thermally activated.[2] However, if DNA breathing is mediating the formation of a highly-fluorescent monomer subpopulation, then reducing the solution temperature will reduce the rate of DNA breathing, thereby reducing the population of monomers and increasing the population of virtually non-fluorescent aggregates. Thus, one expects a reduction in fluorescence intensity of DNA-templated Cy5 aggregate solutions at reduced temperature.

4. What is the source of the longer-lived dimer subpopulation in the type-2 DNA-templated adjacent dimer solution? From the GTA of the TA data measured for the adjacent dimer solution, we concluded that there are potentially two J-aggregates in the adjacent dimer solution: one with a lifetime of 40 ps, and the other with a lifetime of 242 ps. This 242 ps lifetime is the longest measured for a Cy5 aggregate in the studies presented in the preceding chapters. The presence of adjacent dimer, monomer, and short-lived J-aggregates make it difficult to study what leads to the longer lifetimes in this structure. In **Chapter 2**, we showed that subtle differences

in the absorption spectra of Cy5-Cy5.5 heterotetramers of the same composition arise from changing the position of the dyes on the DNA Holliday junction template. There are three other Cy5 adjacent dimer configurations that have not been studied. By preparing and characterizing solutions of these other dimers with the methods described above, we may find that one of the adjacent dimer configurations contains a larger fraction of these longer-lived structures. Additionally, we also noted in **Chapter 4** that the DNA Holliday junction can undergo isomerization, and that the subpopulations may exist transiently as the DNA template undergoes structural reorganization. If the Holliday junction template could be modified to prohibit this isomerization, this hypothesis could be tested.

References

(1) Cannon, B. L.; Patten, L. K.; Kellis, D. L.; Davis, P. H.; Lee, J.; Graugnard, E.; Yurke, B.; Knowlton, W. B. Large Davydov Splitting and Strong Fluorescence Suppression: An Investigation of Exciton Delocalization in DNA-Templated Holliday Junction Dye Aggregates. *J. Phys. Chem. A* **2018**, *122* (8), 2086–2095.

(2) Scharf, B.; Dinur, U. Striking Dependence of the Rate of Electronic Radiationless Transitions on the Size of the Molecular System. *Chem. Phys. Lett.* **1984**, *105*, 78–82.

(3) Humeniuk, A.; Mitrić, R.; Bonačić-Koutecký, V. Size Dependence of Non-Radiative Decay Rates in J - Aggregates. *J. Phys. Chem. A* **2020**, 124, 10143–10151.

(4) Saltiel, J.; D'Agostino, J. T. Separation of Viscosity and Temperature Effects on the SingletPathway to Stilbene Photoisomerization. *J. Am. Chem. Soc.* **1972**, 94 (18), 6445-6456.